
University of
Strathclyde
Glasgow

Micro-LED direct writing and structured illumination in automated photolithography

PhD Thesis

Alex Blanchard

Structured Light Research Group
Department of Physics, Institute of Photonics
SUPA, University of Strathclyde, Glasgow

February 11, 2026

This thesis is the result of the author's original research. It has been composed by the author and has not been previously submitted for examination which has led to the award of a degree.

Signed: A.BLANCHARD

Date: 04-02-2026

Dedicated to the memory of Andrew John Blanchard

1956 - 2023

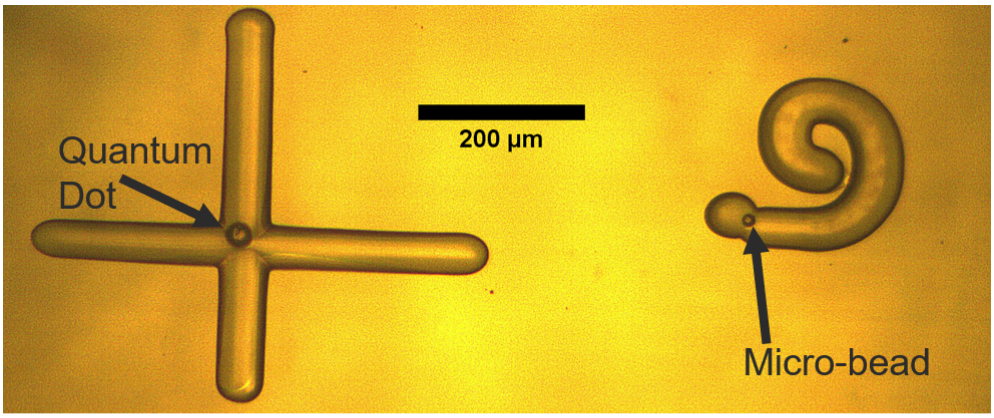

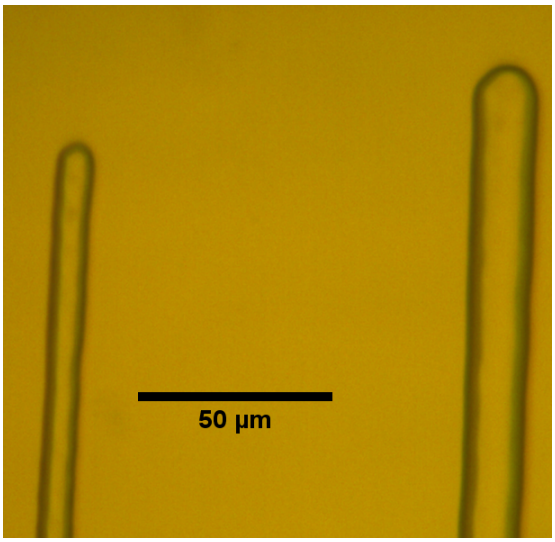

Top: Two photo-cured structures, where hyperspectral positioning was used with indicated markers as a starting point for photo-curing.

Bottom: The thinnest structures cured using a 40 μm deep ultraviolet LED.

Acknowledgements

This project and thesis wouldn't have happened without many, many people helping and supporting me. Thanks go first of all to my supervisors, Johannes and Martin, for their time, insight, and guidance in supporting me and my work over the course of this project. It couldn't have been done without you. Financially, thanks go to EPSRC, Fraunhofer UK, and the Platform Grant fund for supporting this project.

Thank you to the colleagues who I have become friends with, laughed with, and bored senseless about photolithography over the past six years: Olivia, Daniel, Graeme, Jonathan, Johnathan, Elise, Alistair, Charli, Charlotte, Bethan, Dillon, Isaac, Sean, Stephen, Utkarsh, and all the Emmas. Special thanks go to Mark Stonehouse for the laughs, knowledge, and time he spent working in this area before me.

My friends, thank you for being there for me and having a laugh with me throughout, especially those from Sambayabamba, Glasgow Frontrunners, and Glasgow Lions, who gave me the opportunity to switch off and remind me that there is more to life than physics. Special thanks go to my once-flatmate Kelly James, who during the COVID-19 lockdowns, put her body on the line helping me move a coffee table in and out of my bedroom to make a homemade optics lab.

Finally. Mum, Dad, Elizabeth, thank you for always having my back and supporting me, even when I told you that I'd be starting a PhD five years after saying that I didn't want to go into academia. Thank you for giving me the platform to leap off from and fly. I hope this does you all proud. Time to book the trip to Uzes!

Abstract

Monolithic micro-Light Emitting Diode (μ-LED) arrays comprising of pixels on the micro-scale is a rapidly developing technology of interest to researchers through their high efficiency and modulation rate. Coupling with complementary metal-oxide semiconductor (CMOS) electronics allows these devices to provide structured illumination via spatio-temporal control. The CMOS drivers control the optical emission pattern of the μ-LED arrays, resulting in a direct writing tool with photo-curing μ-LEDs. Direct writing is an alternative approach to the quartz masks that are commonly used in photolithography.

This thesis describes the use of these CMOS controlled μ-LED arrays for mask-less micro-photolithography, using hyperspectral imaging to look simultaneously at multiple markers. This can be done through numerous methods, but it was decided to focus on spectral analysis of the fluorescent markers during the photolithography process, with system instructions tied to the peak fluorescent wavelength. This thesis also reports deep ultraviolet photo-curing with μ-LEDs, with structures down to 7 μm in size, albeit without CMOS control.

These demonstrations were possible through the development of an experimental direct writing setup. The setup involved confocal combination of two μ-LED sources and one detection arm. Identification and positioning of fluorescent markers was enabled by active illumination with the μ-LEDs and bespoke post-processing of the time-sequence detected signal. These efforts culminated in the demonstration of writing structures individually aligned with different fluorescent markers on the same substrate, where the markers were all red-emitting and could only be distinguished by resolving their emission spectra. The system that was developed is shown to be capable of curing highly

uniform structures with controllable width via direct writing. This is possible thanks to a motorised XYZ stage, controllable alongside the μ-LED array. This technology offers prospects for a range of applications.

Contents

List of Figures

List of Figures

List of Acronyms

LED	Light Emitting Diode
μ-LED	Micro-Light Emitting Diode
UV	UltraViolet
DUV	Deep UltraViolet
SPAD	Single Photon Avalanche Diode
SPI	Single Pixel Imaging
HSPI	HyperSpectral Single Pixel Imaging
GaN	Gallium Nitride
Si	Silicon
Mg	Magnesium
QW	Quantum Well
MQW	Multiple Quantum Well
EBL	Electron Blocking Layer
QCSE	Quantum Confined Stark Effect
MOCVD	Metallo-Organic Chemical Vapour Deposition
EQE	External Quantum Efficiency
IQE	Internal Quantum Efficiency
CMOS	Complementary Metal-Oxide Semiconductor
QD	Quantum Dot
nm	nanometer
μm	micrometer
ms	millisecond

ZnS	Zinc Sulphide
CdSe	Cadmium Selenide
NA	Numerical Aperture
rpm	Revolutions Per Minute
DMD	Digital Multi-mirror Display
FoV	Field of View
PWM	Pulse Width Modulation
MSI	MultiSpectral Imaging
SNR	Signal to Noise Ratio
CCD	Charge-Coupled Device
FWHM	Full Width at Half Maximum
FLIM	Fluorescence Lifetime IMaging
SIM	Structured Illumination Microscopy
TCSPC	Time-Correlated Single Photon Counting
DI	DeIonised
IPA	IsoPropyl Alcohol
NMR	Nuclear Magnetic Resonance
fps	frames per second
TMF	Time Modulated Fluorescence
TMI	Time Modulated Illumination
ESEM	Environmental Scanning Electron Microscope
PPE	Personal Protective Equipment
KET	Knife Edge Test
TIA	TransImpedance Amplifier
PCA	Principal Component Analysis
PC	Principal Component
LSF	Least Squares Fit

List of Tables

List of Tables

Chapter 1

Introduction

This thesis focuses on the usage of micro-pixelated light-emitting diode (micro-LED, or μ-LED) arrays with electronic control as part of an automated, mask-less photolithography system. This chapter serves as an introduction to LEDs, focussing on Gallium Nitride (GaN) μ-LED arrays. The chapter starts with the motivation behind this work, and the historical development of LEDs. Then some theory and physics behind μ-LED devices are explained, and characteristics are presented that need to be determined for the μ-LED devices to operate at peak performance. The subsequent sections detail lithography, photolithography, and the concepts behind the automation in the system: structured illumination, single pixel imaging, and fluorescent markers.

The rest of the thesis is as follows. Chapter 2 explains the μ-LED based direct writing system, characterises it, and shows the results of photolithography with the system. Chapter 3 then explores Deep UltraViolet (DUV) photolithography with the system, using DUV μ-LEDs. This includes a brief size-dependent study showing how different sized DUV μ-LEDs affect the structures cured by the system. Chapter 4 then adds intelligence into the direct writing system by utilising Hyperspectral Single Pixel Imaging (HSPI) to differentiate between similarly coloured fluorescent markers used for positioning. This is done by looking at how the brightness of the markers changes with a changing μ-LED array pattern, with each coordinate position assigned a unique fingerprint pattern. Finally, Chapter 5 summarises the key findings of this thesis and outlines further work with the system.

1.1 Motivation

A motivator for structured illumination in the context of photolithography is to add intelligence to photolithography through closed loop process control. This is where a system will automatically detect process parameters, and use the results as an input into itself [1]. It is possible to use this approach for positioning [2], where the position of a marker can be found and then used as a signpost through further processing.

Currently, mask-less photolithography is more suited to low volume production and prototyping than mass production that is prevalent in semiconductor processing. Mask-less photolithography removes the requirement for the fixed-format hard masks, and is used in areas such as device prototyping. This technique has compatibility with numerous types of wafers or device structures, resulting in bespoke processes for each project and wafer. A traditional masked lithography system can be cumbersome, as a mask for each design needs to be manufactured and stored, with financial and storage concerns. Mask-less photolithography offers an attractive alternative for prototyping where patterns can either be embedded within the curing system, or given as instructions to a direct writing system, where the spatial modulation is in the light source itself. μ-LEDs can be used for direct writing photolithography [3] [4]; they have a low size, weight, and power plus cost (SWaP-c), are easily controlled by electronics, and are easy to maintain.

Structured illumination and compressive sensing can be used for low light level imaging [5], or to correct for image distortions. This capability is useful for delicate samples, such as in the life sciences, or organic chemistry in structured illumination microscopy.

1.2 History of LEDs

The light-emitting diode was discovered by accident by Henry Joseph Round [6]; by applying 10 Volts across a crystal of Silicon Carbide (or carborundum as it was known), a yellow light could be seen. This was electroluminescence and was described in more detail by Olec Lossev in the 1920s, who characterised his device further and showed

how the current through the device changed with applied voltage, signifying its diode nature [7].

Thirty years later, Roosbrock et al. explained the electroluminescence previously discovered as the result of electrons and holes recombining [8], and this physical process was soon after commercially exploited. The 1960s brought the first commercial LED, with Monsanto making red-emitting Gallium-Arsenide-Phosphide (GaAsP) LEDs in 1968, which were used for displays, and then in traffic lights.

Rapid innovation in the area of blue LEDs began in the 1990s by Shuji Nakamura, Hiroshi Amano and Isamu Akasaki, whose work earned them the Nobel Prize for Physics in 2014 [9]. By using Aluminium-Indium-Gallium-Nitride (AlInGaN) semiconductor alloy technology, blue LEDs were made at a much higher efficiency than previous indirect bandgap blue LEDs, allowing for the full visible spectrum to be spanned by LED technology. By covering a blue LED with a suitable rare earth phosphor to output a yellowish hue, LEDs were demonstrated to output white light as seen to the human eye, making such devices suitable for many lighting applications, thus ushering in the era of solid-state lighting. Today, LEDs have widespread applications such as street lights, headlights in cars, with indoor lighting and even for use in televisions. White light sources based on LEDs are far more efficient and robust than incandescent and fluorescent bulbs.

1.3 Research overview in Maskless Photolithography

This section will discuss prior research in maskless photolithography, with sections dedicated to direct writing using lasers and LEDs. Direct writing with a laser requires some form of external spatial modulation, most commonly a Digital Multimirror Display (DMD). However, [10] reports using a mercury lamp with a DMD chip to facilitate maskless photolithography, and feature sizes of approximately 50 μm with a 20 μm resolution. Mercury lamps are commonly used in masked photolithography.

1.3.1 Direct Writing

Lasers

Lasers are a direct competitor to μ-LED arrays as an illumination source for maskless lithography, but as previously stated, require some sort of spatial modulation. [11] reports using a UV laser for direct writing; a third harmonic Nd:YAG laser at 355 nm is focussed onto a sample with a thin film of Indium Tin Oxide. This is an early attempt at using lasers to create circuits on Indium Tin Oxide glasses as a dry etch technique, which do not require other chemicals. The spatial modulation in this paper comes from a linear motor stage that moves the film to create the patterns in the film.

In [12], a GaN-based diode laser at 375 nm was used to photo-cure a photo-resist based on 1,4-cyclohexyldimethanol divinyl, while a translation stage was used as the spatial modulation. From this system, a Lissajous structure was written into the photo-resist, showing that curves are indeed possible using translational stages. Being used as part of a wet etch technique, [12] is much closer to the experiments performed in this thesis.

However, it is not solely needed for the stage to move for laser direct writing. [13] reports using a galvanometer based optical scanner for the spatial modulation with a laser at 355 nm. This paper proves it is possible to create microstructures down to 500 μm, which were used as part of a flexible piezoresistive sensor. By changing the speed of the laser across the sample, the ability to create different shapes of structures was reported.

LEDs

Direct writing can be performed with LEDs of varying sizes, alongside laser-based systems. [14] reports use of a 5 mm wide UV LED coupled into a 3 mm pinhole which was again coupled into a microscope setup. A stage attached to a moving piston provides the spatial modulation. Structures in the shape of dots, lines, and crosses were reported using this system.

[15] was used as the inspiration behind this work, and reports using a μ-LED array for the purposes of photolithography; more specifically, a CMOS (Complimentary Metal-Oxide Semiconductor) controlled μ-LED array. The main differences between this work and the work presented in this Chapter 2 are from the difference in the peak wavelength of the exposing LEDs (370 nm instead of 405 nm reported in this thesis), and the fact that this system uses a microscope objective to couple the μ-LED illumination into the system. This objective lens would have a far smaller Numerical Aperture than the coupling lenses that were used in this thesis; as a result, far fewer μ-LEDs can be coupled into this system compared to the system that is presented in Chapter 2. As a result, the positioning work would not be possible using the system presented in [15]. This work utilises two different types of spatial modulation: firstly, a linear stage is used to expose the linear structured reported in this paper. However, multiple pixels, or LED devices, can be turned on simultaneously to expose and cure multiple structures, showcasing a different type of spatial modulation.

[16] presents an improvement on [15] by using LEDs with a smaller active region, 14 and 24 μm in diameter compared to 72μm in [15]. A demagnification of 10:1 was used to make structures 500 nm in width. Once again, a moving stage or simultaneous device illumination can be used in order to provide the spatial modulation in this system. A maximal exposure dosage of 3.75 Wcm^{-2} at 370 nm was reported in this system.

[17] showcases that much like for a laser or mercury lamp, it is possible to use an LED with a DMD to supply the spatial modulation. In [17], an LED operating at 405 nm is coupled into a DMD array, and then a microlens array, utilising pinholes in order to focus the light onto the samples that are being exposed. As pinholes are being imaged onto the sample, this means that the structures made are far smaller than what is possible in the system presented in Chapter 2, but would have a much lower fill factor, defined as the ratio of the area of focussed light compared to the full illumination system. This system has a spot size of 4.4 μm, and distance between adjacent spots of 110 μm, compared to a spot size of 20 μm, and distance between adjacent spots of 33 μm.

[18] indicates the state of the art in the Institute of Photonics when the work presented in this thesis started. In [18], a single μ-LED array is coupled into an aspheric lens and then demagnified before being coupled into an objective lens. As before, there are two potential avenues for spatial modulation: from the motorised stage, and illuminating numerous array pixels simultaneously. It can be seen that when multiple adjacent μ-LEDs are used for exposure that the structure made can lose the resolution of individual spots. This could be potentially due to over-curing, as the array used does seem to have higher power output pixels around the edges of the LED array used. Note this paper does not showcase any of the positioning work undertaken in this thesis, and uses only one μ-LED array.

1.4 LED Theory

1.4.1 The p-n junction

LED operation is based on the recombination of carriers (electrons and holes) in what is known as a p-n junction. This is formed by growing two consecutive doped layers of semiconductor, one of each type, creating a band diagram as shown in Figure 1.1. In Figure 1.1, Ecp and Ecn refer to the energy level of the conduction band in the p- and n- doped material, Evp and Evn refer to the energy level of the valence band for the p- and n- doped material, Efp and Efn refer to the Fermi levels of the p- and n- doped material, Eg is the energy gap between the two bands, and eV_D is the depletion energy, defined further below.

Between the two types of material lie the depletion region, which is where recombination occurs; here, a potential difference is created between the two areas of semiconductor, V_D, known as the depletion voltage, opposing the flow of carriers. This means that there is an associated barrier energy eV_D that the carriers must overcome for them to flow across the barrier. The size of this depletion region is dependent on the concentration of the dopants. By applying a forward bias on this junction, the potential energy barrier is decreased, allowing the carriers to recombine. This happens because the Fermi level in the p-doped side is higher than the n-doped side, allowing electrons

to freely and easily move across the junction to recombine with the holes. Applying the biases showcases the diode nature of the device, as the energy levels will also move with a negative bias applied, but instead in the opposite direction; this widens the energy barrier, ensuring that very little current will flow across the device.

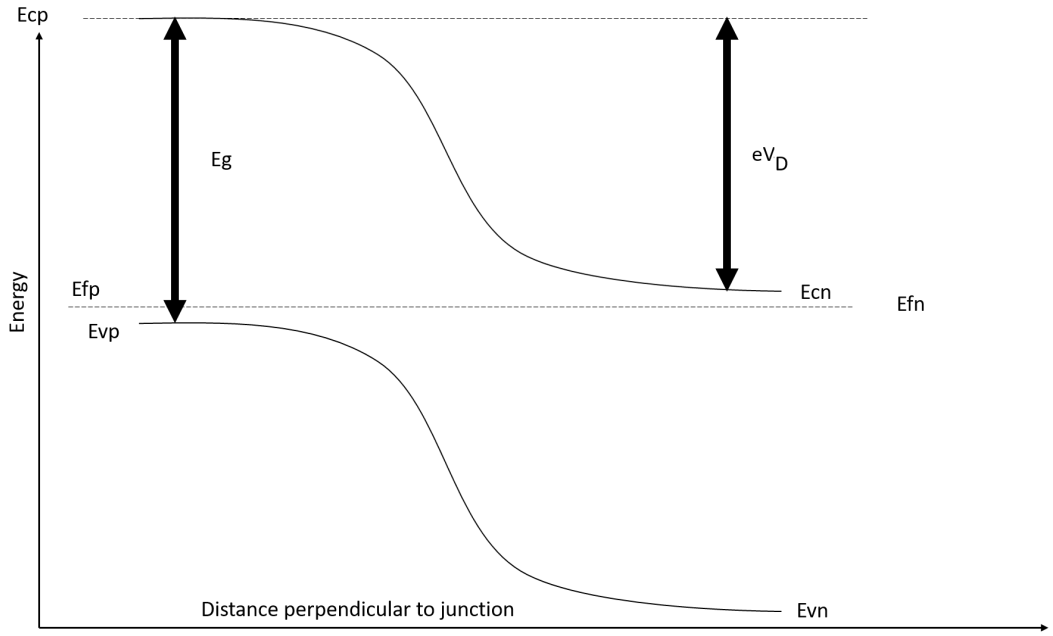

Figure 1.1: Schematic showing a p-n junction.

By physically confining the carriers in the material, the carrier concentration can be increased [19]. In modern LEDs, this is done by use of Multiple Quantum Wells (MQWs), which are placed between the p and n type material, and made of a different material, with a smaller bandgap. As a result, there is a potential difference at the interfaces between the two materials, trapping the carriers in the well. By making these wells very thin, on the order of 10 nm, their width becomes on the same order as the de Broglie wavelength of the electrons in the material. This allows the system to function as a potential well with discrete energy levels, and by carefully choosing the gap between the energy levels, specific wavelengths of light can be emitted.

Further confinement of the carriers, typical in nitride device structures, is done by adding an Electron Blocking Layer (EBL), between the MQWs and the p-type material, which has a higher conduction band level than the p-type material. This again makes

an energy barrier, and reduces electron leakage directly to the p-contact, where non-radiative recombination occurs.

1.4.2 LED Format

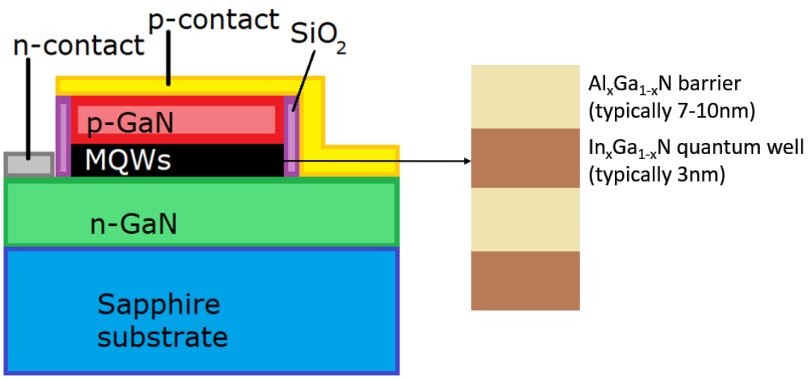

Figure 1.2: Diagram showing the cross-sectional schematic of an LED. There would often be more MQWs than labelled here, about 10.

A cross-sectional schematic of an LED is shown in Figure 1.2. This shows an individual LED, which for a μ-LED would be less than 100 μm in diameter. In the case of an array, there would be a common cathode (n-contact) between all the μ-LEDs and individual anodes (p-contact) for each LED. The LEDs used in this thesis are made by a process known as flip-chip bonding, which attaches the GaN epi-layer structure to a heat sink. This improves the thermal dissipation of the LED and thus its light-extraction efficiency. Flip-chip bonding requires the anode material to be reflective, to allow light to leave through the sapphire substrate, which is optically transparent at visible wavelengths.

The experimental work in this thesis was achieved through the use of custom Si-CMOS (Complimentary Metal-Oxide Semiconductor) electronic drivers. The dimensions of the drivers are the same as the array, such that each device has its own driver with a bond pad of 50 $\times$50 μm^2, with a 100 μm pitch. The drivers have their own individual logic circuitry, allowing the device to be operated in a pulsed mode, down to 300 ps.

A example circuit diagram of a CMOS μ-LED driver is shown in Figure 1.3, from

[20]. The two separate ground levels are necessary to drive the μ-LEDs above the nominal 3.3 V that is used for driving the logic circuit, by changing the ground level of the μ-LED to have a negative bias.

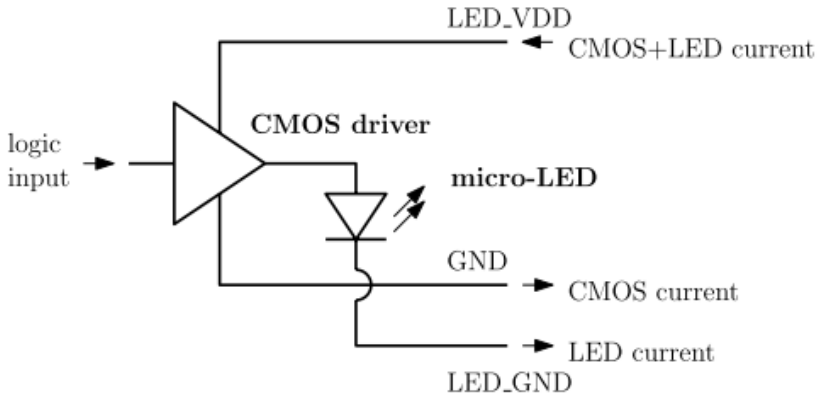

Figure 1.3: Circuit diagram for the μ-LED driver circuitry. From [20].

1.5 LED Characterisations

Before any μ-LED device is used in scientific or instrumentation applications, it must first be characterised to determine its electrical and optical properties.

1.5.1 Electrical Properties

The electrical properties of an LED that are of primary interest are the current draw and voltage drop. Figure 1.4 shows representative curves showing the drawn current from an applied voltage (IV). The IV curve shows typical diode characteristics with the current draw in two regimes: the exponential part, where the diode resistance is more than the load resistance, and the linear part, where the diode resistance has reduced from higher voltage being applied and so the diode behaves as according to Ohm's Law. The point where this changes is called the 'turn on' voltage, found from finding the gradient of the linear section of Figure 1.4 and finding the x-intercept value[21]. To aid in finding this x-intercept, the dotted diagonal line continues the gradient of the linear portion of Figure 1.4, and the intercept itself of approximately 3.8 V is noted by the

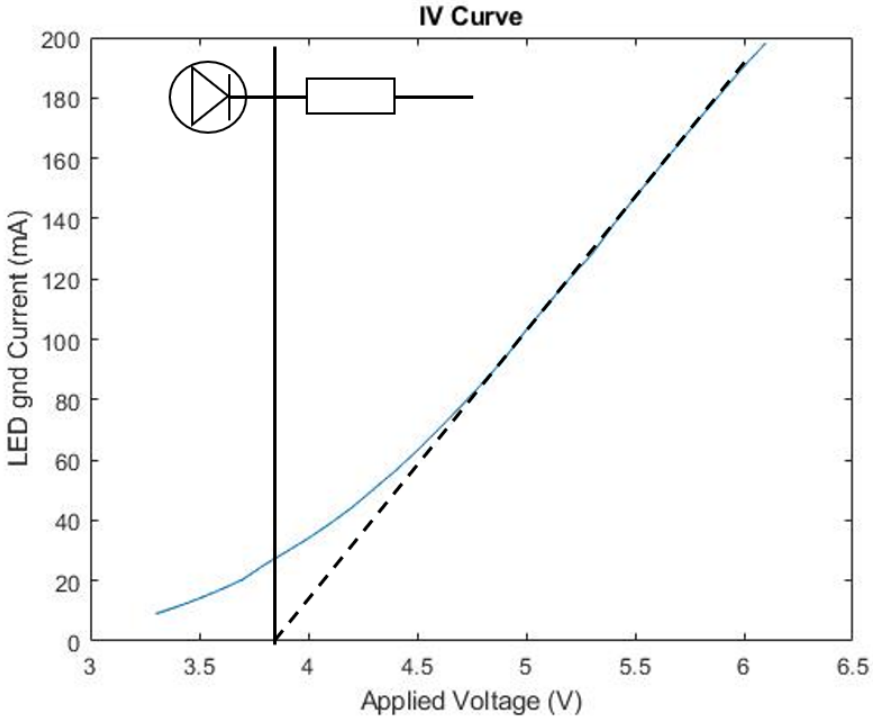

Figure 1.4: Graph showing how the current draw through a representative nitride LED changes with applied voltage. Note the non-zero x-axis origin.

solid line, which indicates the change from diodic to ohmic behaviour.

For an efficient and optimised LED, this should be close to the bandgap energy of the semiconductor in the LED, approximately 3-5 V for a nitride device. In Figure 1.4, 'gnd' is short for ground, and the dotted line indicates the turn-on voltage, where the IV behaviour changes from exponential to linear. This particular μ-LED had a peak wavelength emission at 505 nm, and was part of a 40×10 array.

1.5.2 Optical Properties

Figure 1.5 shows a representative graph of the associated light output from a given current flow through an LED. This LI curve shows a linear increase in light output with current until thermal effects start to degrade the performance of the device. The compromise between device lifetime and output power requires the current used to be approximately two thirds on the linear section of the curve, as over driving the LEDs can lead to device damage [22].

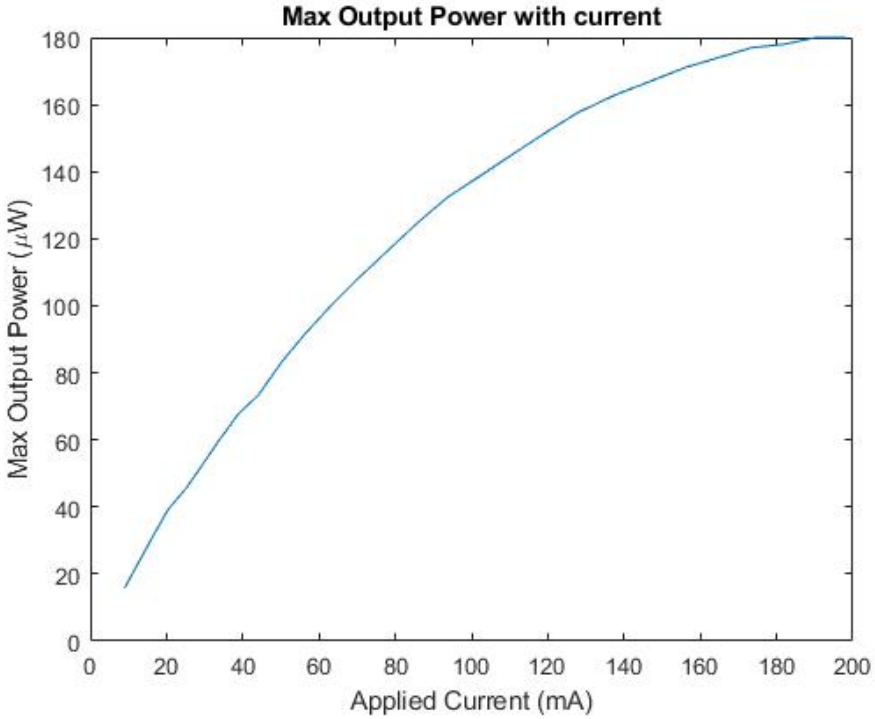

Figure 1.5: Graph showing how the output power of the same 505 nm μ-LED pixel used in Figure 1.4 changes with applied current.

The emission spectrum is an important optical property of an LED, with an example spectrum of a blue InGaN device shown in Figure 1.6 a). The peak LED wavelength (on this example, at 450 nm) is important to ensure proper use, and in Figure 1.6 is the output of the quantum wells. There is also a 'yellow band' emission, as shown in Figure 1.6 b), which is due to defects in the active layer material [23], [24]. As this thesis uses the phenomenon of fluorescence for positioning, particularly in Chapter 4, it is important to be aware of the yellow band emission when analysing the spectral data. The spectral width of the main emission peak has many sources. One of them is due to the energy levels being broadened by the carriers' thermal energy and follows the Boltzmann distribution. The peak of such a distribution is $E_g + \frac{kT}{2}$, where E_g is the energy gap of the material, k the Boltzmann constant, and T the temperature and the Full Width Half Maximum (FWHM) of 1.8 kT. Other sources for an LED's the spectral broadening are strain in the active material, fluctuations in quantum well width, and changes in the semiconductor composition [25, 26].

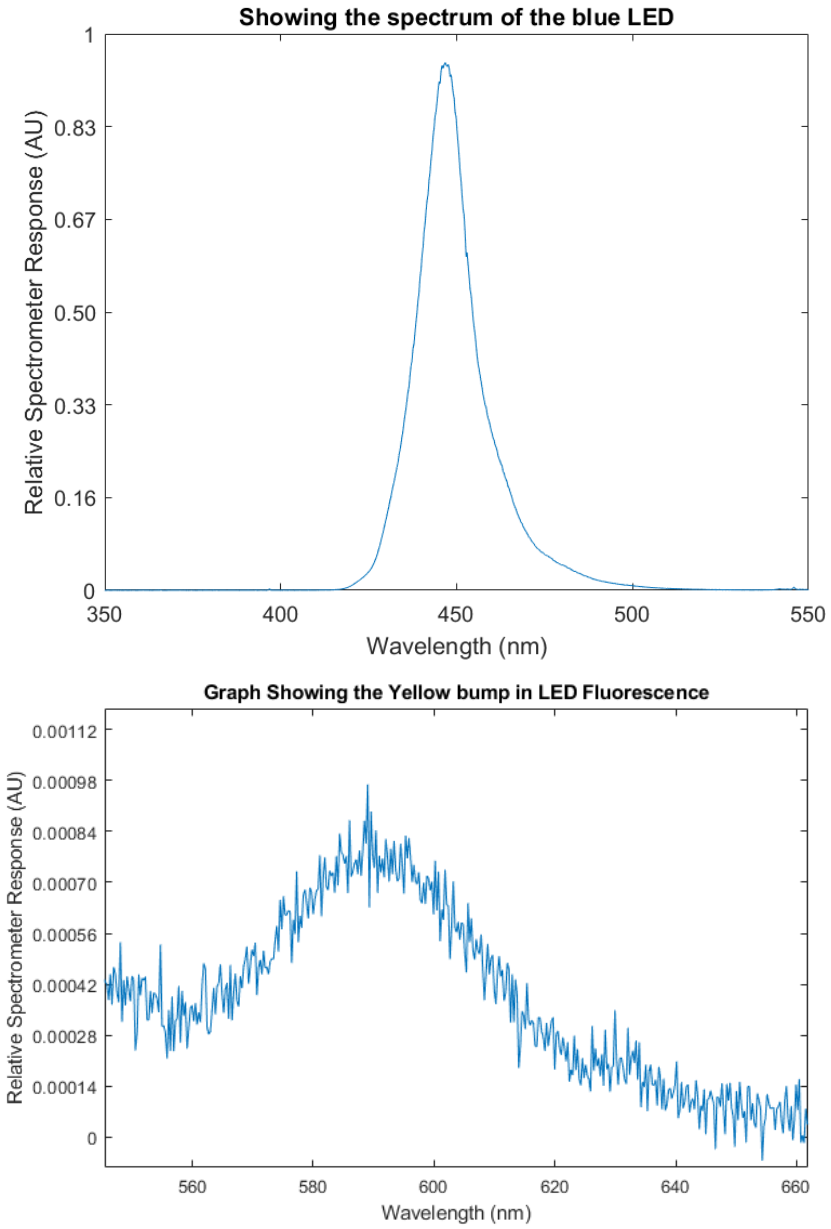

Figure 1.6: Blue LED emission spectra. a) shows the full spectrum of a blue LED, and b) shows the 'yellow band' emission from the same LED as used in part a). The y-axis values of part b) are scaled in relation to the peak value in part a), to show their relative heights.

The linewidth of a blue μ-LED is approximately 0.15 eV.

1.5.3 Efficiency

There are three main efficiency values for LEDs: the External Quantum Efficiency (EQE), the Internal Quantum Efficiency (IQE), and the Wall Plug Efficiency (WPE). The EQE is defined as the ratio of the number of photons emitted to the number of electrons passed over the p-n junction; it is related to the WPE, which is the ratio of the output light power to the input electrical power across the device (voltage $\times$ current). The IQE is the proportion of electron-hole recombination events that are radiative, and is therefore embedded in the EQE. The EQE is more commonly cited, as it includes the IQE via the light extraction efficiency, or the proportion of photons that exit the device. Figure 1.7 shows a representative EQE curve as a function of current, using the same 505 nm μ-LED pixel as used in Figures 1.4 and 1.5. As the current increases, the EQE increases at first and then decreases after a peak point. There are many theories detailing why this might be the case, where the leading ones include the change in the non-radiative recombination of carriers in the material [27], or an increase in parasitic current [28], thus reducing the IQE and therefore the EQE.

1.5.4 Pixel Geometry

The main advantage μ-LED arrays have over broad-area devices is their smaller pixel size when compared to conventional LEDs. μ-LEDs have an active region of less than 100 μm^2 [29], which gives distinctive physical properties largely originating from the high current density the devices can sustain [30]. Their small size lead to two advantages over larger conventional LEDs: a lower capacitance, leading to fast switching speed, and a small spot size, leading to high illumination intensity. Combining these advantages together, GaN μ-LED arrays are particularly suitable for electronic visual display purposes due to their brightness and efficiency, allowing a high density of pixels and high frame rates, with applications in augmented reality headsets [31].

In the μ-LED arrays used in this work, there were two types of pixel geometry used: square pixels, which are 98 $\times$98 μm^2 across, with a pixel pitch (the distance between

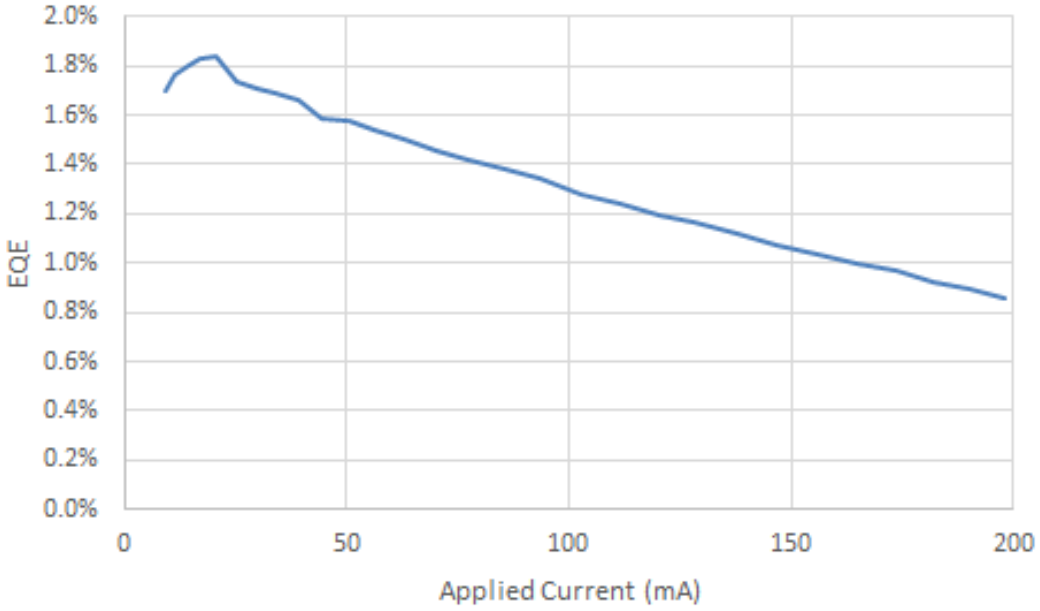

Figure 1.7: Graph showing the EQE as a function of current, for the same 505 nm μ-LED device used in Figures 1.4 and 1.5.

the centres of two adjacent pixels) of 100 μm, and circular pixels 72 μm in diameter, again with a 100 μm pixel pitch. A micrograph of the square pixel μ-LED array is shown in Figure 1.8, and circular in Figure 1.9. The fill factor of an array is the ratio of the active area of the pixels in the array divided by the overall area of the array. In the square pixel array shown in Figure 1.8, the fill factor is very high, at 98 %. The circular array has a fill factor of 41 %.

The μ-LED arrays used in this thesis are active-matrix; that is to say, that there is a switch device actively maintaining the pixel state for each pixel in the array. By addressing the switch, it is theoretically possible to drive an array with 3 connections: a data connection and two power connections for the array.

In comparison, passive arrays have a signal for the row where all the pixels in the row are switched on, with each column having its own individual signal, meaning that the pixels maintain their state passively, without active driving circuitry. This requires $m + n$ connectors to address the entire array, where m and n are the dimensions of the array. Active matrix arrays are in use throughout this thesis as passive arrays cannot display arbitrary patterns in continuous wave output, such as the Hadamard pattern

Figure 1.8: Micrograph of a μ-LED Array. The 99×99 μm^2 square pixels are immediately visible in the array.

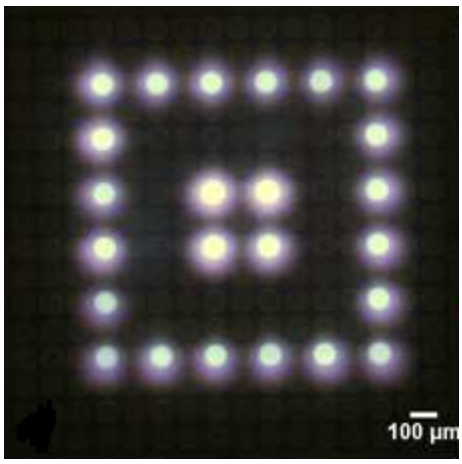

Figure 1.9: Micrograph of a μ-LED Array illuminating a pattern [15]. Here, the circular pixels are 72 μm in diameter.

that will be explained in Section 1.11.5.

1.5.5 Frequency response

The maximum operating modulation frequency of an LED is defined by its modulation bandwidth, the frequency where the the amplitude of the LED output has halved compared to low frequencies. This is dependent on the capacitance and carrier lifetime

of the diode. μ-LEDs demonstrate higher bandwidth than conventional conventional LEDs, on the order of gigahertz, due to their small size reducing capacitive effects and shorter carrier lifetimes [21].

1.6 Fluorescent markers

A key topic throughout this thesis is the alignment of micro-fabrication tools to fluorescent markers. Fluorescence is the absorption and subsequent emission of light at a longer wavelength than the absorbed light. It is important to note that fluorescence is not always the same colour as the object appears, for example, green chlorophyll fluoresces in a red colour. Fluorescence is often excited with UltraViolet (UV) light, but the use of UV sensitive photo-resists make UV light unsuitable for this work. For this reason, fluorophores that do not require UV light to fluoresce are used. This section will focus on the marker types that were used in this work: quantum dot clusters and polyethylene microspheres.

1.6.1 Quantum dot clusters

Quantum Dots (QDs) are nanocrystals of semiconductor material, often less than 10 nm in size, consisting of a few thousand atoms. Due to their size, they can be thought of as a three-dimensional quantum well (hence 'quantum dot'), confining carriers in each crystal spatial dimension. This means they have quantised energy levels, based on the size of the dots. The dots absorb energy when the light incident upon them has a larger photon energy than the band gap between the valence and conduction bands. The emitted wavelength is strongly dependent on the size of the quantum dots. The quantum dots used throughout this thesis are in fact clusters of quantum dots, so as to be visible on the micro scale. These QD clusters have a ZnS outer shell with a inner core of CdSe, suspended in deionised water; the shell improves the quantum efficiency of the dots by removing the surface defects [32].

An example emission spectrum of QD clusters is shown in Figure 1.10. This is a Gaussian with a peak at 580 nm, the width of which is determined by the size distri-

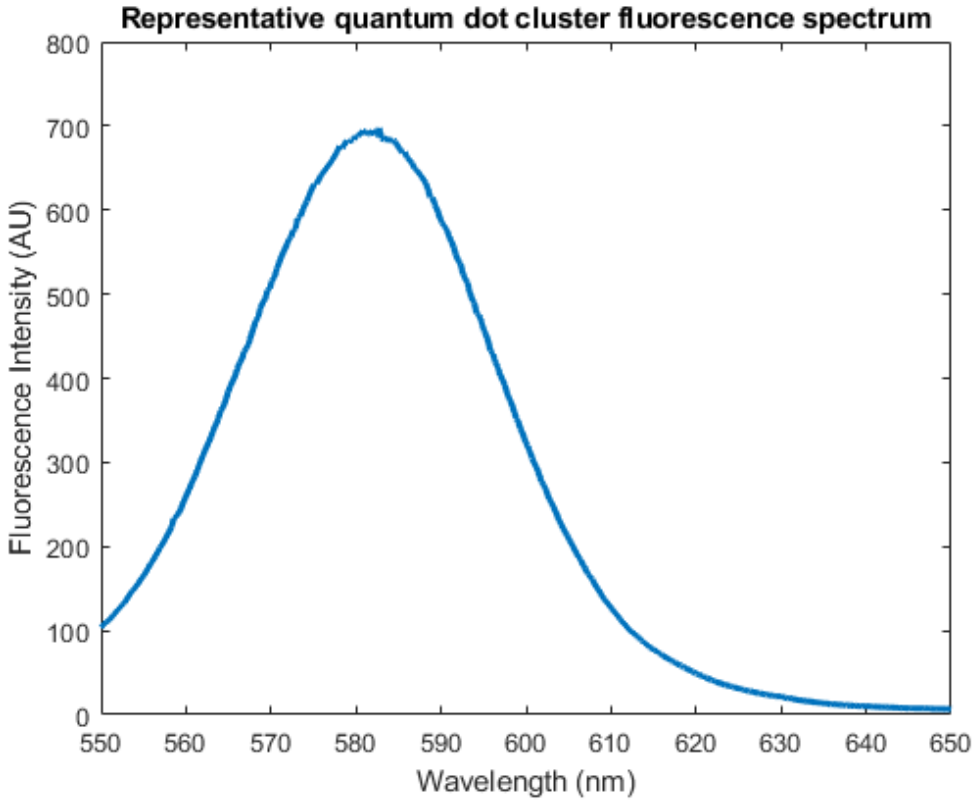

Figure 1.10: Example of a quantum dot cluster emission spectrum.

bution of the QD clusters of 20 μm. The wide emission range makes them suitable for use in many applications, such as colour converters in LEDs [33], markers in biological samples [34], [35], and cryptography [36],[37].

1.6.2 Fluorescent dyed polyethylene beads

Another type of marker that is used in this thesis is polyethylene beads, dyed with a fluorescent dye. These beads are used in biomedical research, often with magnetic separation to determine the concentration of other chemicals [38], or visualisation and analysis of fluid flow [39], [40].

The bead emission spectrum is shown in Figure 1.11 when excited with 450 nm illumination, as shown in Figure 1.12 where a bead is being excited in a microscope setup. The dye used is a trade secret, and the beads themselves are 10-22 μm in size.

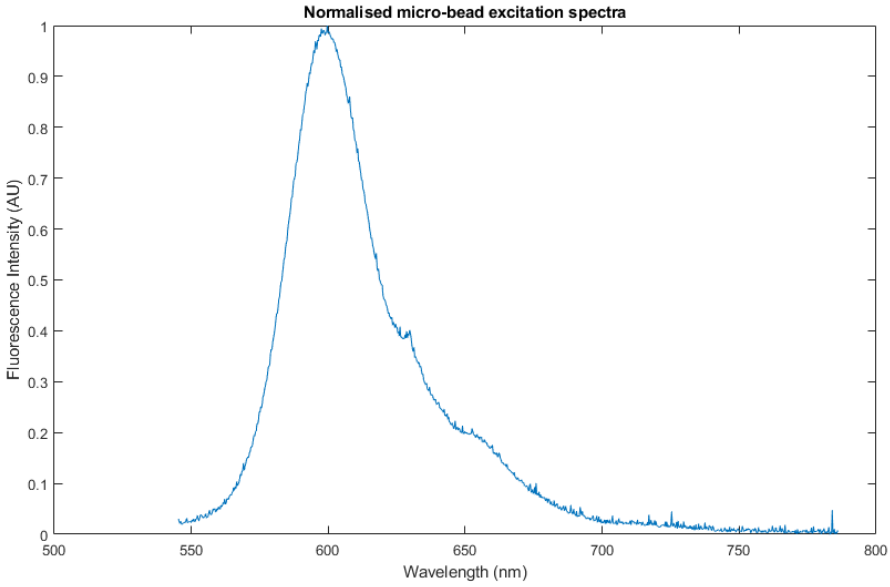

Figure 1.11: Graph showing the spectral response curves emission of the fluorescent dyed micro-beads used throughout this thesis. Light at 450 nm was used to excite the micro-bead [41].

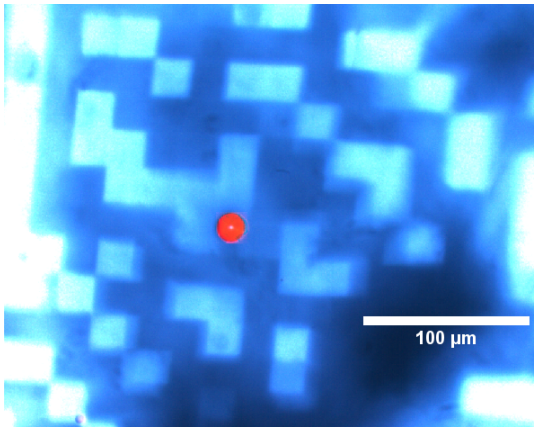

Figure 1.12: An excited fluorescent micro-bead. The bead is being illuminated with 450 nm LED light.

1.7 Photolithography

Micro-patterning is the method of transferring a pattern onto a substrate, commonly done during the micro fabrication of semiconductor devices. It has applications in areas including integrated circuits and photonic circuits [42, 43], LEDs [44], [45], and organic electronics [46], [47]. One of the most common methods of micro-patterning is called photolithography, or optical lithography. This section will give an overview of photolithography as an example of micro-patterning and its history.

1.7.1 History

Photolithography as it is currently known was invented by Alphonse Poitevin in 1855 [48], making a lithographic printing plate using potassium bichromate and albumin, where the ink only adhered to the parts of the plate which had been exposed to the light. Over time, to help facilitate the cylindrical rotary presses of the time, the plates were changed from limestone to metal plates, where Poitevin's technique was used. In the 1950s, American military researchers took inspiration from photosensitive liquids used to protect aircraft wings and used them to protect semiconductor material, reducing the size of electronic circuits in the process [49]. This was the first time the term photolithography was applied to electronics circuits and it has grown since then to the widespread masked version used today.

1.7.2 Photo-curing theory

Photolithography works by coating a substrate with a layer of light sensitive material called a photoresist, and then selectively exposing the sample with a known light pattern. The photo-resist is chemically altered when exposed to light of a suitable wavelength, either by decomposing into a soluble chemical for a so-called positive photoresist, or solidifying into a solid structure for a so-called negative one. Normally, a positive photoresist is used, so that less exposure is required. The maximum achievable resolution with optical sources is given by the diffraction limit via the Rayleigh Criterion. In equation form this is:

$$d = \frac{\lambda}{2NA} \tag{1.1}$$

where d is the diffraction limited spot size, λ the wavelength of the light used and NA the numerical aperture of the focussing optics. In practice, the latter is the most used method to change the smallest possible spot size. A large change in the wavelength of the emitted light is required for an appreciable change in the beam spot size, requiring there to be a change in the optics as well; therefore, changing the optics by themselves is more practical.

From Equation 1.1, a reasonable assumption would be to use the shortest possible wavelength for photolithography. Extreme UltraViolet (EUV) uses light with a wavelength of 13.5 nm [50] for features under 100 nm. This wavelength of light does not propagate through air [51], and so this lithography technique is done in vacuum. EUV can make the smallest size features from a photolithography technique, but due to the requirement for a vacuum, and expensive high-NA optics [51], the cost of large scale EUV lithography for chips and wafers is high. Typical laboratory photolithography therefore uses mercury lamp spectral lines, including i-line (365 nm), h-line (405 nm), and g-line (436 nm).

Photoacid Generation

Photo-resists contain chemicals called photoacid generators, molecules that release hydrogen ions on absorbing UV light, thus becoming more acidic. An example of a photoacid generator is shown in Figure 1.13. Here, the UV light breaks the chemical bond between the Phosphorus Fluoride ion and the rest of the generator[52], a process known as photolysis. This creates an acidic ion, used as a catalyst for photopolymerization of monomers in the photoresist into a polymer [52].

The acidic ion transfers to a monomer in the photo-resist, thus becoming charged. The charged monomer is then attracted to the double-bond in another monomer molecule due to the relative high electron concentration in the double bond and reacts to it, forming a positively charged two unit length polymer. This process continues to form the polymer as many units in a link. During growth, polymer chains can be chemically

linked to each other. This results in a crosslinked polymer, also known as a polymer network. [53]. Photolithography allows fine spatial control of this polymer network. The number of crosslinks in the polymer network, known as the crosslinking density, is dependent on the excitation dosage on the sample. The crosslinking density also determines the solubility of the polymer in a solvent, called the developer. This developer is chosen so that it will dissolve either the polymer or monomer, but not both. In order for the photoacids to be made, the photo-resist must absorb the illumination used, so matching the absorption spectrum of the photo-resist to the emission spectrum of the curing illumination is vital. Common photoresists include Microposit 1805, a positive photoresist and SU-8, a negative one. Both of these photoresists have a very high absorption at deep ultraviolet wavelengths below 300 nm, reducing as the wavelength increases. Figure 1.14 shows this behaviour with 10 μm films of SU-8.

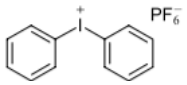

Figure 1.13: Chemical composition of a photoacid generator.

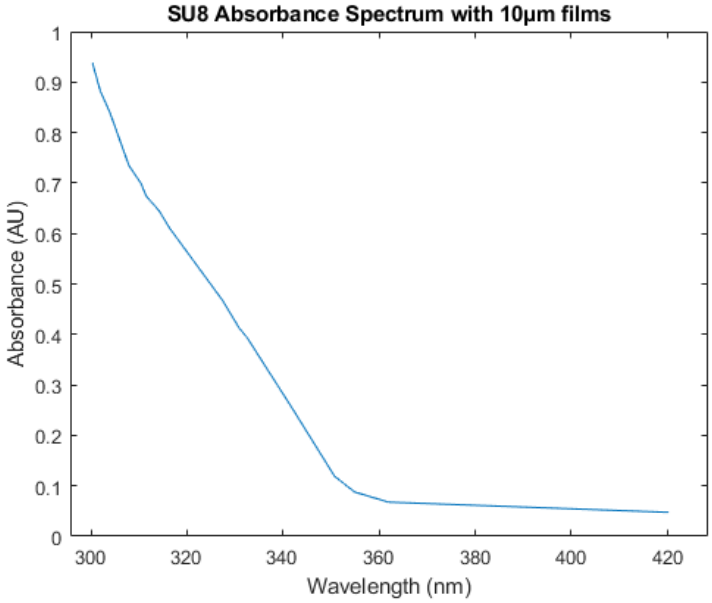

Figure 1.14: Absorption spectrum for SU-8 photo-resist.

In this thesis, photolithography will be done with photo-resist films with a thickness on the order of a few microns. The films were made by spin coating, where drops of photo-resist are placed on a clean, dry substrate to be cured and spun at several thousand revolutions per minute (rpm). This ejects the top layer of resist from the sample, while the bottom layers of resist move radially from the drop site towards the sample edge. If the photo-resist is viscous, this can result in a ridge or bump in resist at the sample edge. After the film has been made and cured, it is developed to reveal the pattern within the photoresist, and the sample is then often baked to improve the durability of the cured structure. The sample can then be used for further processing.

1.8 Patterning Methods

There are many ways to pattern photoresist onto a sample, and an overview is given in this section.

1.8.1 Multi-step processes

Mask Aligners

Traditionally, photolithography is done with UV lamps, which are large, inefficient and rely on toxic materials, both in the lamp and the photo-resist. The patterns are traditionally made by shining the light through a stencil known as a mask, which is near to or in contact with the sample. The masks are made of glass covered in either Cr or Fe_2O_3 and depending on the type of photo-resist used, will either have the negative pattern or positive pattern on them. It is important to note that once the masks are made, they cannot be changed, and a different mask is required for each photolithographic step, meaning that there are typically many masks for one device [54]. As a result, it can be expensive to design, make, and store all the masks required for a device, especially with numerous circuit designs being made. Therefore, alternatives for mask aligners are being sought for low volume production, such as in customisation and prototyping.

Figure 1.16 shows a camera image of a mask aligner as used in the clean room in the Institute of Photonics. The yellow lighting is required to not unnecessarily expose photo-resist or other photosensitive chemicals that might be used in the clean room. The mask and sample are in the black drawer in the centre of the image, with micrometre screws for fine adjustment of the position. There is a microscope objective lens and eyepiece for looking at the sample. Figure 1.15 shows the schematic of a mask aligner as shown in Figure 1.16. Figure 1.17 shows a sample that has undergone the masked photolithography process; the small black dots are microscopic dents in the substrate.

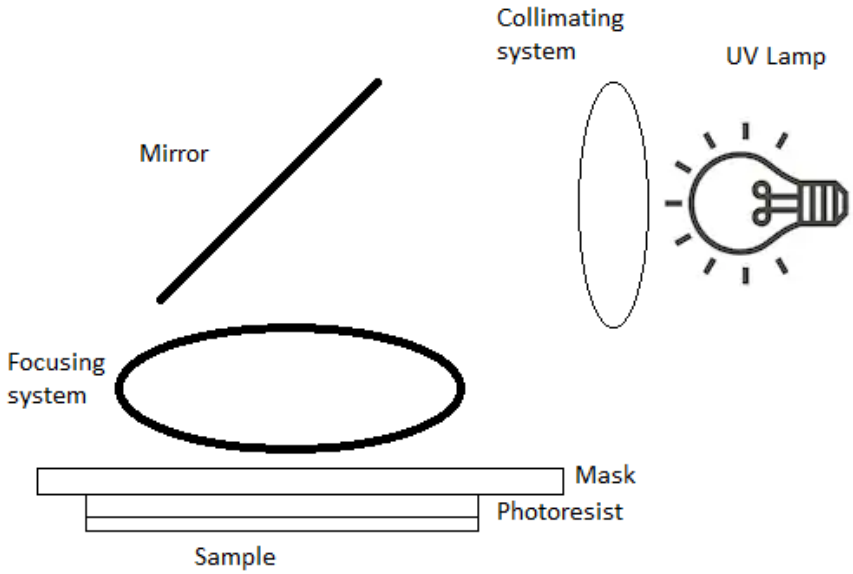

Figure 1.15: Simplified schematic of a mask aligner.

Figure 1.16: Photograph of a mask aligner in the Institute of Photonics cleanroom.

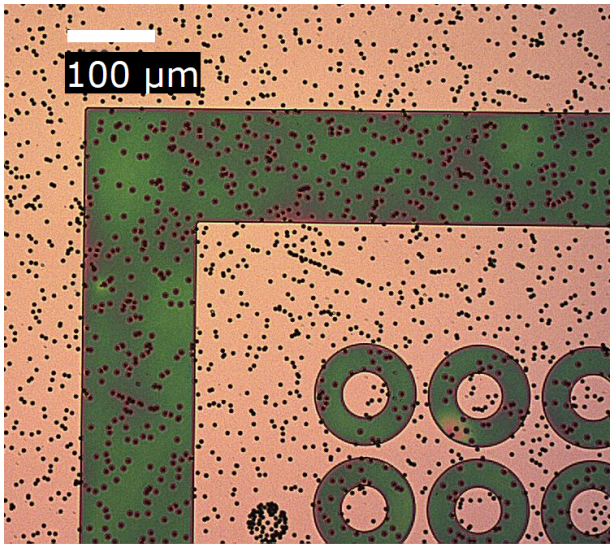

Figure 1.17: Showing a sample photocured with the mask aligner in Figure 1.16. The black dots in the image are microscopic dents in the substrate.

μ-LED Direct writing

This thesis concentrates on μ-LED direct writing; that is, shining light directly on the photo-resist film in narrowly focussed beams to cure the photo-resist. Commercially available direct writing photolithography is most commonly done with lasers, but μ-LEDs are a capable and attractive alternative, with qualities such as being smaller [18] and more energy efficient [30]. In direct writing, patterns are made by moving the sample, and/or by patterned exposure from an array of sources.

The size of these cured areas depends on the Field of View (FoV) of the μ-LED array, or the size of the projected μ-LED spots on the sample. Therefore, having a large fill factor is important; with a small fill factor, there will likely be large gaps between μ-LED spots, meaning that there will not be uniform curing, which results in holes in the cured structures, which would be unsuitable for devices. Each individual μ-LED's performance affects the curing, and for this reason, having a uniform power output across a μ-LED array is important for curing uniformity when using an array of pixels. Figure 1.18 shows a schematic of an μ-LED based direct writing system. The single curing μ-LED is collimated by the lens, and the light then goes into a microscope

objective and is focussed onto the sample. The projected size of the curing μ-LED can be reduced by using two lenses to demagnify the curing light. The XYZ stage is required to move the sample to make lines and shapes in the photo-resist. See Chapter 2 for more detail.

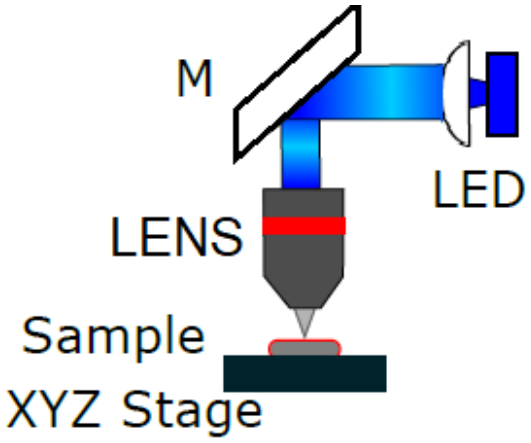

Figure 1.18: Schematic of a μ-LED-based writing system. The μ-LED at the appropriate curing wavelength is imaged through the collimation lens, which is then reflected off the mirror and then through the objective lens onto the sample. The mirror is used to ensure that any light that misses the collimation lens does not accidentally cure the photo-resist.

1.8.2 Other lithography techniques

While photolithography is a common technique, light is not the only way in which to pattern a photoresist. For example, electron beam lithography is similar to direct laser lithography, but instead uses electron beams for direct writing [54]. Due to the shorter de Broglie wavelength of electron beams than DUV, on the order of pico metres, this allows for much smaller feature writing than other types of photolithography, but it is limited to small volume production due to the timescales involved. Masks for masked lithography are often made via electron beam lithography, where a focussed beam of electrons is used to pattern samples. Thanks to the smaller wavelength of electrons compared to visible light, this results in resolution down to 10 nm, with pattern areas on the millimetre squared scale. For large masks, stitching between the areas is required, aided by automated positioning and closed loop process control to ensure fine precision.

Nano-imprint lithography is another lithography tool with very high resolution, down to 10 nm [55], [56]. This is where a mould or other stamp creates a pattern by deforming an imprint resist, which is then processed, and cured during the imprinting. This can be done with heat or light. Given the 10 nm resolution, being aware of the position is vitally important for large volume manufacturing using this method; misaligning the stamp can potentially ruin the process. The added intelligence of structured illumination and feedback control ensures that the stamp or mould will be in the correct place, down to the resolution of the projected spot size used for positioning [57].

1.8.3 Translation stages

With a single light source such as a single μ-LED, a translation stage allows the drawing of lines and shapes in photo-resist, and for larger areas to be cured. It also makes a mask unnecessary for direct writing. Linear motorised stages allow fine control of the position, with their positional accuracy limited by the smallest step size of the stage and the error in the step size. In this thesis, linear servo motors are used with encoders to provide better control of the stage movement. These were chosen due to their ability for external, autonomous control, as this would allow more intelligence to be embedded in the system by direct control of the stage position. However, the movement process involves mechanical slippage, which can induce systematic or random error; the motor used had an encoder resolution of 30 nm but the stage itself has a repositioning accuracy of 2.5 μm.

1.8.4 Alignment Markers

For many applications of photolithography, it is essential to have a reliable and repeatable process of aligning the pattern to existing structures on the sample. In this thesis, the ideal marker would not react with any part of the sample in any way and would be easily visible by a detector, with no inaccuracy in its position. The errors involved with such an alignment marker depend on how precisely the edges of the markers can be aligned.

In masked photolithography, the reflective alignment markers are included into the mask, an example of which is shown in Figure 1.19. Alignment can be done with the micrometre screws previously mentioned, and aligning with a straight edge results in an error on the micron scale [58].

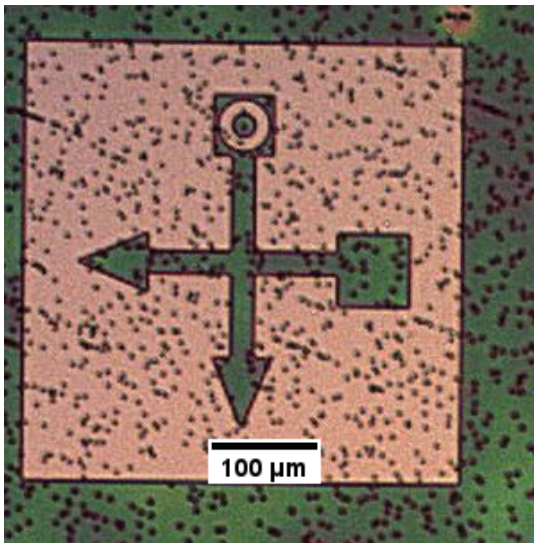

Figure 1.19: A reflective alignment marker as used in a mask aligner; the same microscopic dents in the substrate can be seen as in Figure 1.17.

1.8.5 Fluorescent Alignment Markers

The reflective alignment markers used within mask-based systems are not the only type of alignment markers used. Throughout this thesis, fluorescent markers are used, which are added to the sample itself. The fluorescence of the marker is used to determine the marker's position, allowing the markers to be a functional part of the device, as well as a fabrication aid.

As an example, a fluorescent micro-bead used as an alignment marker could have electrical contacts fabricated onto it. The marker can be either used as a termination point of the contact (start or finish), or the sample can be moved before the contact can be printed. From this, the contact would be part of an opto-electronic device. Thinking to the future, such a capability could be used for example to make an LED with a single QD as the opto-electronic emitter. This would have an atom-like nature,

and would allow direct electro-optic stimulation and access to quantum effects.

As noted previously in this thesis, colloidal alloyed core QD clusters and polyethylene dyed micro-beads are used as fluorescent markers for direct writing (see Chapter 2 for more detail). They are small, respond to non-curing wavelengths with eye-visible fluorescence, and are unreactive with the photoresist. The markers can be taller than the height of the layer of photo-resist that is being cured, and current positioning techniques do not allow for control of the marker positions. This means that subsequent procedures need to align to the marker positions. Fluorescent markers are not the only kind that can be used for positioning in this way; the markers can be reflective or transmissive instead. If using reflective markers, there should be some way of determining when the marker is illuminated. An example of a fluorescent marker as used in this thesis is shown in Figure 1.12, which is approximately 20 μm wide.

1.8.6 Closed Loop Process Control

In this thesis, closed loop control is used in the automated photolithography system as part of the alignment methods. In a closed loop system, a controller will give a signal to a motor to move to a given point. A feedback system is in place to automatically determine the output of the movement and give feedback into the controller, to send a new control signal if necessary. This has applications where the system is fully automated as it can correct itself to a target value.

PID (Proportional Integral Derivative) is a common control algorithm used for automation, and is used in the experimental work in this thesis. It comprises of three elements: the proportional element, which looks at the difference between the current and target values; the integral, which looks at the sum of these differences between measurements; and the derivative, which controls the rate of change of the value. By tuning these three elements experimentally, an ideal response can be made to automate a system to get an object, such as a fluorescent marker, to an predetermined position.

1.9 Exposure Dosage Calculation

The exposure dosage calculation estimates the amount of light energy incident onto the sample during the curing process of photolithography. Estimating the dosages ensures the photo-resist will be sufficiently photo-cured and allows comparison with other photolithography arrangements. Dosage calculation for a static photolithography sample is trivial: the output power of the curing illumination at the sample position is multiplied by the time that the sample is illuminated for. This assumes an even spread of light throughout the sample without any reduction in curing power. This can be done by being spread over a large enough area that there is no noticeable reduction from a Gaussian light distribution at the illumination edge. If the sample is moving, the calculation is more involved, as described by the following equation:

$$E = \frac{2P}{\pi R^2 v}\sqrt{R^2 - y^2} \tag{1.2}$$

where E is the dosage in Joules/cm^2, P is the curing device power, R is the projected spot radius, v is the speed of the stage, and y is the coordinate perpendicular to the movement [15]. This assumes that the projected spot is circular, with a constant movement speed and a uniform stage speed. By looking at the centre of the cured structures, i.e. where y = 0, this reduces the above equation to the following:

$$E = \frac{2P}{\pi R v} \tag{1.3}$$

A non-linear solvent can reduce the curing dosage required to start curing in a photo-resist [59]. This can be done with a contrast enhancement layer, such as a photo-bleachable dye, on top of the photoresist. The dye changes the refractive index during photo-curing to be slightly larger than the photo-resist [60]. This makes a lens in the polymerised contrast enhancement layer, focusing the photo-curing illumination and increasing the curing illumination efficiency.

1.10 Sample Characterisation

After the sample has been made and cured, characterising it allows determination of how well it matches the intended structure. Some of the criteria that are examined are the height and uniformity of the structure, the angle of the structure edge walls, and the presence of debris on the sample. The profile will show the beam shaping of the curing illumination through the photolithography system, and the suitability of the cured structures for the intended applications such as waveguides. The following section will explain some techniques used throughout this thesis to examine structures after the photolithography process.

1.10.1 Optical Microscopy

Optical microscopy, where a sample is placed in an optical microscope and viewed, is a non-invasive examination method. The ease of changing the objective lens allows looking at different length scales; a low magnification to search for the structure at first and then a higher magnification for close examination, such as the smoothness of the structures' edges. An example of an optical microscope image of a fabricated structure is shown in Figure 1.20, with different objective lenses, to show the difference in scales and magnification. Quantitive data of the structure size requires a calibration with an object of known size. The resolution limits of an optical microscope depend on the optics used, with the NA, or Numerical Aperture, of the objective lens used having the largest effect on the resolution at a fixed wavelength, with a higher NA value resulting in a higher resolution.

Surface Profiling

Optical surface profiling is a non-invasive method that uses the reflection of light at different places and the resultant interference pattern to determine the roughness of a surface [61]. It allows estimation of the height of the structure as well, when considered that the structure itself is the roughness to be measured by the profiler. The profile of the structures shows the uniformity of curing in that dimension and the sharpness of

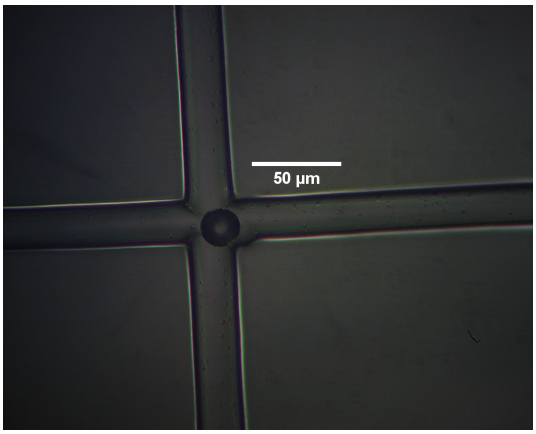

(a) Seen though a x40 microscope objective.

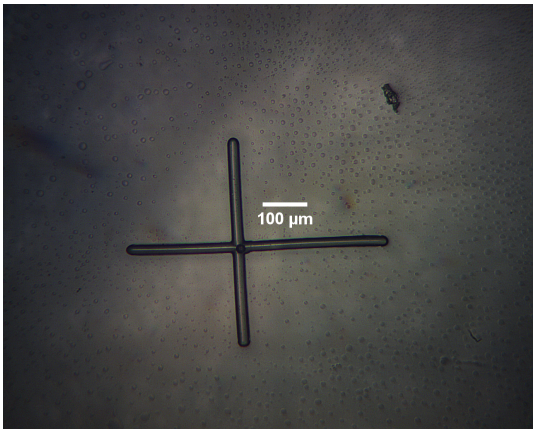

(b) Seen through a x10 microscope objective.

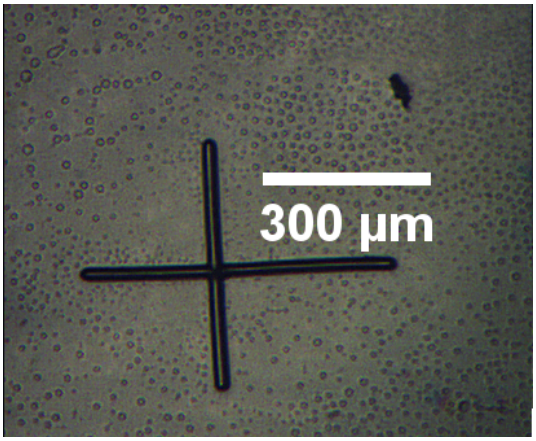

(c) Seen through a x4 microscope objective.

Figure 1.20: A cured photolithographic structure viewed through a x4, x10 and x40 microscope objective lens. The bubbles that can be seen around the structure are unwashed excess photo-resist.

the curing illumination can be seen by the gradient of the structure's edges. A near-vertical edge means that the curing illumination is sharp, allowing for higher resolution during curing. A large spread of the illumination is reflected in the structure having a shallow gradient of the side wall.

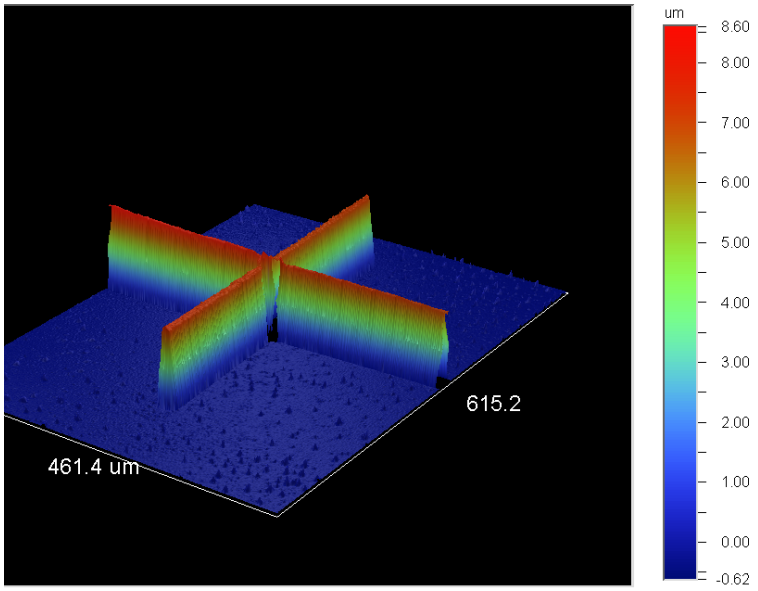

Figure 1.21: The same photolithographic structure from Figure 1.20 as seen in an optical profiler. Note the false colour scale on the right when examining the figure.

Examples of data taken by an optical profiler are shown in Figures 1.21 and 1.22. In these, a cross that has been cured via photolithography had its profile measured. Over the whole sample, this also measures the height of the structure. The cross was determined to have a uniform height over the whole sample of approximately 8 μm, as shown in Figure 1.21, meaning that the curing illumination is uniform. The side walls of the structure can be seen to be steep as well, testifying to a low spread of the curing illumination. It can be seen that the two profiles are different in width (Figure 1.22), estimated to be 25 and 28 μm, for the x and y profile, respectively. The difference might be due to having a different spread in the two axes or a change in the stage speed, if piezoelectric motors are used for curing, or is a potential sign of aberrations in the system, leading to the focussed spot being different sizes in each in-plane axis. Checking the profile of the cured structures via their shape can show if a structure is

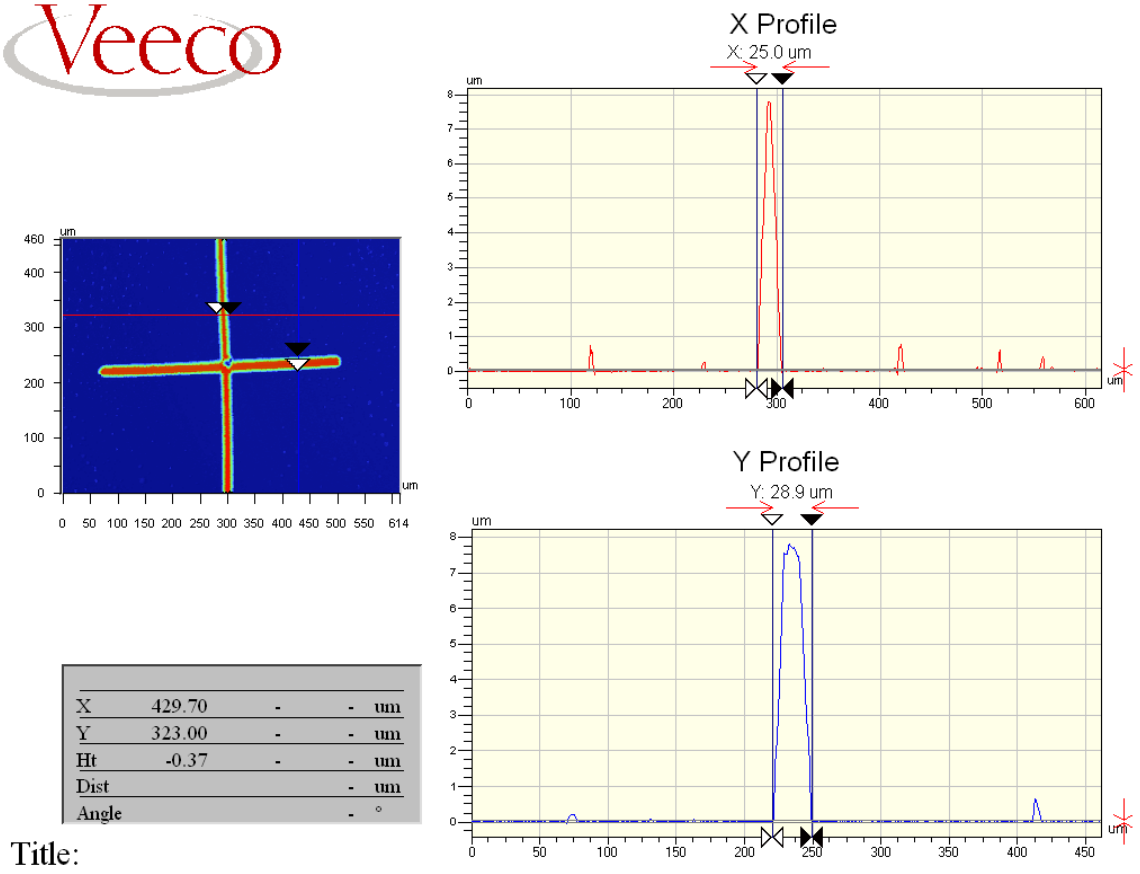

Figure 1.22: The same photolithographic structure from Figure 1.20 as seen in an optical profiler. This shows the profile of the structure across its two arms.

over or under cured; given the expected Lambertian output of the LEDs, this affects the LED output [21]. The in-plane resolution of such a system is dependent on the objective lens of the system, as with optical microscopy. The out-of plane resolution for measuring the height of the cured structures is done by interference patterns in the system and thus is dependent on the resolution of these patterns.

1.11 Structured Illumination Methods

Structured Illumination is the use of spatial modulation with an illumination source, allowing the projection of a spatially sectioned pattern, which changes the illumination as a function of position within the projected image. In doing so, information and communications can be encoded in the spatial composition of the illumination, also known

as space-division multiplexing [62]. This section will look at methods and applications of structured illumination.

1.11.1 Structured Light Illumination Sources

The μ-LED arrays used throughout this thesis allow structured illumination. By individually turning each element in the array on or off, framed illumination pattern sequences can be projected from the array. This approach is called self-emissive as each individual element in the array emits light. Self-emissive displays have a wider colour gamut, higher brightness [63], and a faster response time than their backlit, externally illuminated alternatives [64, 65].

In contrast to the self-emissive methods, a backlit structured illumination source has a single illumination source that illuminated a spatially modulated reflector or transmitter. Digital Micromirror Devices (DMDs) are commonly used spatially modulated reflectors, or Liquid Crystal Displays (LCDs) for spatially modulated transmitters, with a beam-expanded laser an example of the single illumination source. This is used where a laser would be the preferred illumination source due to its optical properties.

1.11.2 Structured Illumination Patterns

A key component of any structured illumination system are the light patterns that are projected (discussed in detail in later sub-sections). Illuminating an area with a suitable pattern allows information gathering of the surface or contents in the Field of View (FoV) of the illumination. This is a scalable method; on the metre scale, for example, this can be used as the basis for an indoor navigation system [66], [67], done by modulated LED ceiling lights. Here, each illuminated 'cell' within the field of view receives a unique binary pattern sequence when monitored through a complete cycle of frames from the structured illumination (μ-LED array) source. Thus, for example, a smartphone could track or navigate people moving through a supermarket or museum. This can then be used to enhance the user experience by offering deals or information about nearby objects, and/or combined with GPS systems to offer seamless indoor and outdoor positioning simultaneously. Indoor navigation using structured illumination is

especially useful where GPS is unsuitable, such as in hospitals, making optical navigation an attractive option. On a smaller length scale, structured illumination can be used for 3D imaging on the centimetre scale, and the micrometer scale used for micro photolithography as in this thesis [68].

Many techniques can be used for positioning, such as triangulation [69], time and angle of arrival [70], and fingerprinting [67]. The work presented in this thesis uses fingerprinting. Fingerprinting projects a pattern where each individual coordinate in the projection will have a unique binary modulation data stream, called the fingerprint. When using a fingerprint pattern, to maximise the Signal to Noise Ratio (SNR), each frame should be orthogonal with respect to the frame after it; that is to say, the inner product of the matrices that describe the illumination of successive frames should be 0 [71]. Many different pattern sequences meet the criteria for fingerprinting. The ideal one would use the smallest sequence length possible, while giving each pixel position its own unique pattern sequence.

When sampling the patterns to take measurements, the sampling rate is important. The Nyquist Shannon sampling theorem says that a signal can be perfectly reconstructed through sinc interpolation, if its highest frequency is less than half of the sampling rate. In the context of the thesis, this means that for a pattern sequence being sent, as long as more than two measurements are made from each projected frame sent by the illumination source, then it will be fully reconstructed. Practically, three or more measurements per projected frame are made, so that a measured frame in the middle of the pattern sent can be used, safe in the knowledge that the entire measurement will only be in that pattern.

The following subsections will present some of the pattern projection sequences that are used throughout this thesis, and the different pattern types that are commonly used. The pattern projections will be used upon a chequerboard style grid projection illumination, as appropriate to a square pixel μ-LED Array.

1.11.3 Manchester Encoding

Throughout this thesis, the projected pattern sequences use Manchester Encoding. In Manchester Encoding, the data bits are encoded in the transitions of the data rather than the individual amplitude level, which is a method called differential signalling [72]. This means that low to high and high to low are the two bits being sent in a binary system, mapped to 1's or 0's [73]. Thus, the clock information is embedded into the signal itself, allowing for synchronisation during decoding. It also allows variance in the amplitude levels of individual pixels, as long as the values for low are smaller than the values for high. This does, however halve the data rate due to needing to have two logic levels detected instead of one for each bit being sent.

1.11.4 Raster Scan

The raster scan is the simplest pattern sequence that gives a unique spatio-temporal fingerprint; one pixel element is turned on at a time, cycling through the entire μ-LED array. For an array with N pixels, a pattern sequence of length N is required [68]. While simple and easily programmed, the linear scaling of the pattern sequence length with array size means that the amount of data to be taken and analysed scales linearly. This can be an issue where a high pixel resolution is required for higher positioning accuracy in a given FoV. Raster scanning typically requires synchronisation of some description between the emitter and detector. It lacks rotational symmetry, and each pixel has a low duty cycle, being on for only $\frac{1}{N}$ of the time [74]. These factors make raster scanning unsuitable for general purpose illumination, which requires flicker-free illumination as seen by humans. This pattern sequence requires high frame rate emitters and detectors, with very high precision timing requirements, both of which would scale linearly with the array size. However, the orthogonality requirement is simple to achieve with the raster scan, as the matrices that describe the raster sequence only contain one non-zero element in each of them; therefore, each frame is orthogonal to each other frame.

1.11.5 Binary Pattern Sequences

This section will discuss important examples of pattern sequences that can be used as an alternative to raster scanning. For a square array of dimension m (so that the arrays size $n = m \times m$), it is desirable to design sequences of binary illumination patterns that enable positioning. Such sequences can be designed to trade off sequence length, signal to noise ratio, and resilience to background signals. For a 2×2 array, the following three matrices provide a useful alternative to a raster scan:

$$B^1 = \begin{pmatrix} 1 & 0 \\ 1 & 0 \end{pmatrix}$$

$$B^2 = \begin{pmatrix} 1 & 1 \\ 0 & 0 \end{pmatrix}$$

$$B^3 = \begin{pmatrix} 1 & 0 \\ 0 & 1 \end{pmatrix}$$

These three matrices are the basis for many different types of binary search patterns. For example, by taking the B^1 and B^2 matrices and expanding upon these over a larger matrix, a row and columns pattern sequence is made, where each column and then row is sequentially illuminated. This is simple to grasp and for a square array would have the shortest pattern sequence length. Figure 1.23 shows the first two patterns of the rows and columns sequence. This pattern is not orthogonal with every frame, with $\frac{1}{4}$ of the frames not orthogonal with the previous frame, affecting the SNR of the positioning.

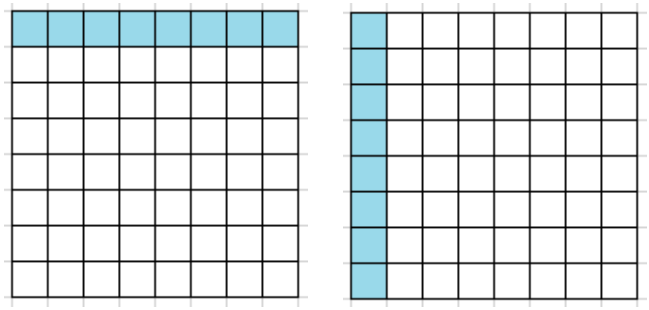

(a) First frame (b) Second frame

Figure 1.23: The first two frames sent in the row and columns sequence.

By taking the rows and columns pattern sequence described previously and increas-

ing the duty cycle to 50%, done by increasing the width of the rows and columns to half the array, the robustness of the patterning sequence is increased due to the higher number of pixels on at any one point, making it more suited for general purpose illumination. This 'moving bars' pattern approach has an advantage in that it can be displayed by a passive-matrix LED array. Figure 1.24 shows the Moving Bars Frames as used in this thesis with a 16×16 μ-LED array.

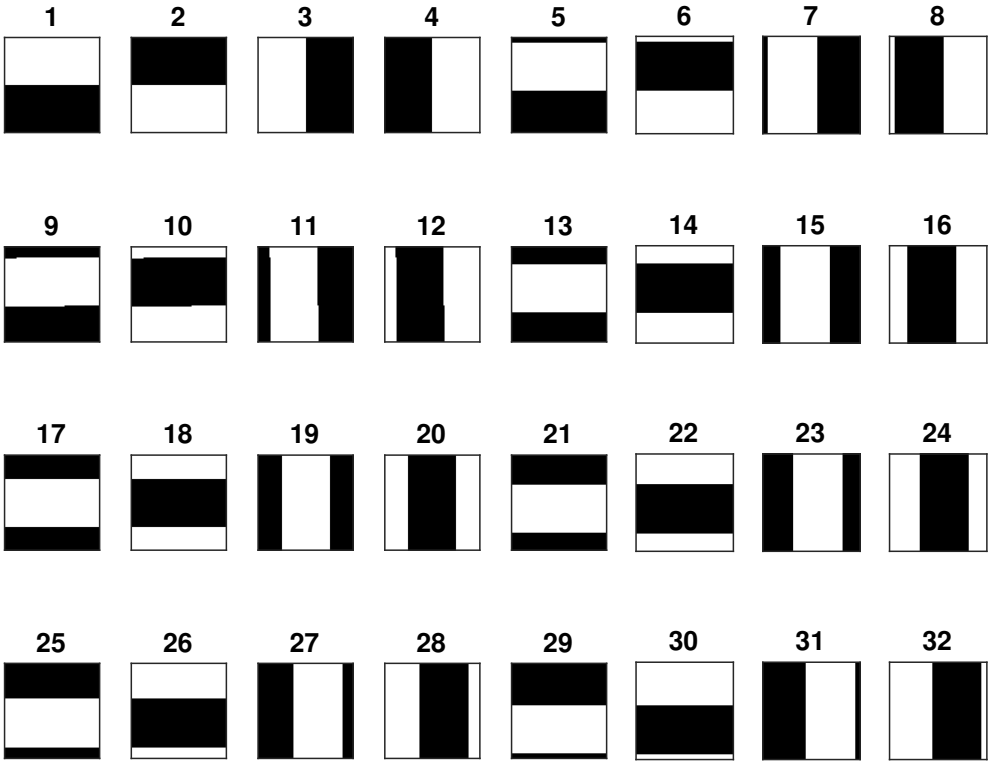

Figure 1.24: The moving bar frames used in this thesis.

1.11.6 Hadamard patterns

The matrices B^1 to B^3, when combined with their inverse, make a pattern sequence known as the Hadamard pattern sequence for $m = 2$, suitable for $2^n \times 2^n$ tracking. While this is not the minimum length that a sequence can have (this would be length $l = 2log_2(n)$), having additional frames improves the reliability, as any errors in the minimum sequence length will affect the positioning. Due to the higher duty cycle of 50 %, this pattern sequence is more suitable for spatio-temporal fingerprinting in general illumination than a raster scan. Each Hadamard pattern has rotational symmetry from the requirement that the inner product of a Hadamard pattern and its inverse must be an identity matrix [75], allowing an even spread of light. These two characteristics make the Hadamard sequence suitable for indoor lighting applications, where over a large enough area and a high enough frame rate, it can be used for indoor positioning simultaneously alongside illuminating the room [76] [77], and only requires a subset of the full pattern sequence, of length $k = 2log2(N)$, where N is the number of μ-LED elements, for positioning[71]. Using a subset of the full pattern sequence is known as compressive sensing, and is key for this thesis as it allows less data to be taken for positioning or imaging. As an example, with an 8×8 array, 12 patterns are required for positioning with Hadamard patterns, compared to 64 patterns in a raster scan, and 16 in the rows and columns pattern sequence. This does not mean that the rest of the pattern is wasted; adding extra frames improves the Signal to Noise Ratio (SNR) [76]. Examples of Hadamard patterns are shown in Figure 1.25; the light blue pixels indicate pixels that are on, and the white pixels are off. Figure 1.26 shows a μ-LED array emitting an example Hadamard Frame onto a piece of paper. Here, however, the white pixels on the laptop screen show an emitting pixel on the array.

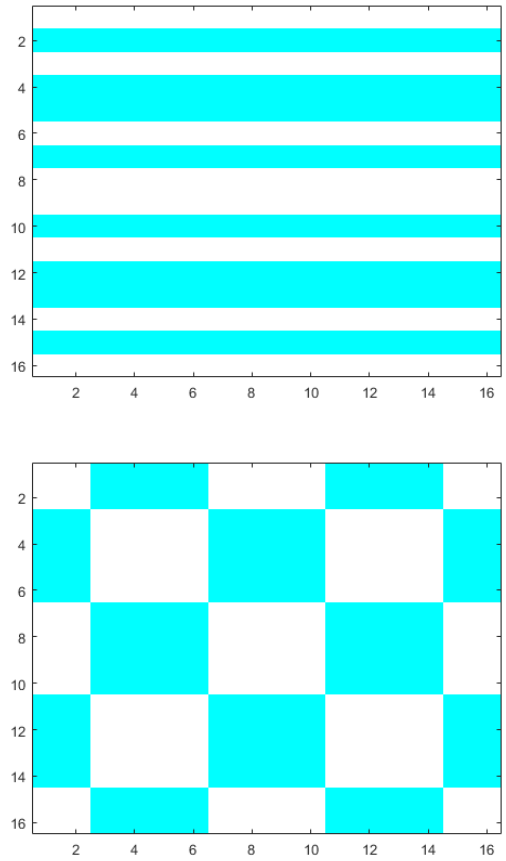

Figure 1.25: Examples of Hadamard frames used in positioning. Here the patterns are illustrated for a 16×16 element emitter device.

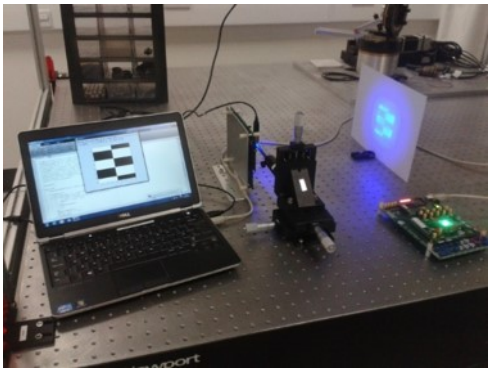

Figure 1.26: Photograph showing a μ-LED board emitting a Hadamard frame. Here, white signifies that a μ-LED is switched on instead of off as in Figure 1.25.

1.12 Structured Illumination Applications

1.12.1 Visble Light Positioning

Visible light positioning is an application of Structured Illumination, possible with self emissive and backlit systems. For any positioning system, a coordinate system needs to be implemented in the illumination field of view. This allows a framework for understanding the object's position in the FoV and quantifies the distance between points within it. Where two or more pixelated systems are within the optical path, such as a μ-LED array projecting onto a DMD, the smallest area that can change in a structured light situation projected on the sample is used as the coordinate system. If there is only one pixelated element (such as a beam expanded laser hitting a DMD) then that element's pixel system is used.

In a structured light visible light positioning system, data are encoded in the position of the data stream, and each position has its own unique data stream, resulting in spatio-temporal fingerprinting. In the μ-LED arrays used in this thesis, there is a pre-determined coordinate system. This can result in coordinate (1,1) not being in the upper left hand corner as expected. This happens when the image of the illumination source is rotated with respect to the detector, either through the optical system or if the two use different schemes.

A practical example of visible light positioning is indoor navigation, applicable to such as a supermarket or warehouse, to improve accuracy where global positioning system signals are inaccurate, or for areas where radio signals are unwanted, such as in hospitals. To determine the position, a receiver, such as a mobile telephone that is within the lighting's field of view can use the principles of compressive sensing and single pixel imaging to find its position within the illumination. This is where a single detector in each device is used to record the illumination that hits it. The recorded measurements are then ordered to find the start of the illumination sequence from which the patterns can be used to find its position.

1.12.2 Compressive Sensing

This section will illustrate compressive sensing and single pixel imaging and how they can be used for visible light positioning. As mentioned above, compressive sensing is a signal acquisition technique used for imaging with under-determined linear systems, where the pattern sequence length is shorter than the total number of illumination pixels in the array. Therefore, more than one pixel is shown in each pattern, while ensuring that the frames are orthogonal to each other. This results in an effect called compressive sensing [78], while the orthogonality reduces the number of frames required for the imaging to work [79].

Compressive sensing differs from conventional compression as the data acquisition is itself compressed, whereas conventional compression requires all the data to be taken before compression can commence [80]. Therefore, this reduces the amount of data taken in the first place.

In the practical application of compressive sensing with structured illumination, the main figure of merit is the compression ratio. This is shown by the following equation:

$$CompressionRatio = 1 - \frac{NumberOfMeasurements}{PixelCount} \tag{1.4}$$

Where Pixel Count measures the number of pixels in the array. It is common these days to see compression ratios of over 90 % [81].

1.13 Single Pixel Imaging

Single Pixel Imaging (SPI) can be thought of as the opposite of imaging that is done with a digital camera, with a single light source and a multi-pixelated detector supplying the spatial information. Instead, the light source is pixelated with a temporally changing illumination pattern, imaged with a single detector [68] [82], such as a photodiode. By knowing each pattern sent and the corresponding measurement on the detector, an image can be reconstructed [83]. The maximum resolution of the output image is the same as the resolution of the illumination [84], [74]. For this reason, SPI aims to use the largest illumination resolution, to maximise the resolution of the output

image. This technique is often used where detectors are expensive to manufacture, such as for wavelengths outwith the visible, or detectors that work on a very short timescale.

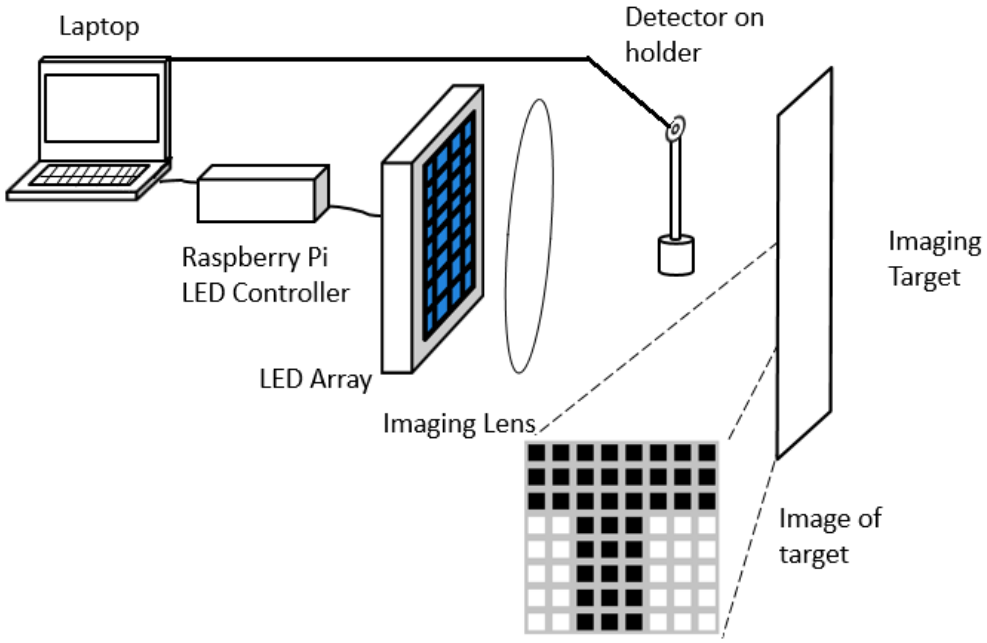

Figure 1.27: Diagram of a Single Pixel Imaging setup.

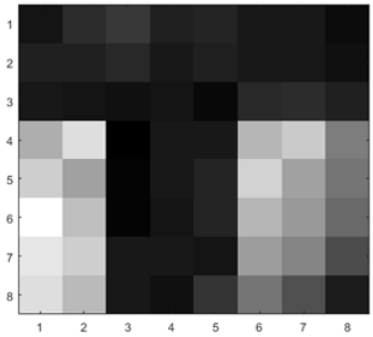

Figure 1.28: Example single pixel image.

Figure 1.27 shows a representative setup used for Single Pixel Imaging. The spatially dependent light source is imaged and directed onto a target (the 'T' shape). The detector fibre then detects the light reflected from the target, which is then sent to the detector and its intensity measured. A lens could be placed over the detector's fibre

holder to match the FoV of the detector and illumination source, thus collecting more reflected light from the target, improving the SNR.

The detector and illuminator are synchronised, either by a trigger signal or embedding a clock in the illumination pattern sequence, allowing one intensity measurement taken per illumination frame. By combining the frame sent with the measured intensity for that frame, a single pixel image can be taken, of which an example of this is shown in Figure 1.28.

1.13.1 Hyperspectral Single Pixel Imaging

Hyperspectral Single Pixel Imaging (HSPI) is a hyperspectral imaging method where spatial information is obtained by using a structured illumination source, and a single pixel detector is used with a narrow spectral resolution. A spectrometer with a fibre input makes an ideal HSPI detector due to combining both of the spectral factors previously stated with a small SWaP-c, allowing it to act as a point detector. HSPI differs from MultiSpectral Imaging (MSI) due to the number of spectral channels used. MSI is often used with CCD cameras as they have three channels, one for red, green and blue parts of the visible spectrum, or with a small number of bandpass or edge pass filters. Spectrometers used in Hyperspectral Imaging typically have a few 1000 channels can be measured with a spectral resolution on the order of 1 nm. HSPI is used in applications such as plant phenotyping, [85], astronomy, [86], [87] and environmental monitoring [88], [89].

Figure 1.29 shows a representative setup for HSPI. The illumination is imaged onto a target, which is then picked up by the fibre in the fibre holder post and then sent to the detector, which has a fine spectral resolution.

When looking at hyperspectral images, many methods are available to analyse the spectra. The peak wavelength and intensity of a given spectrum is a simple yet useful measurement. While it gives only two values per pixel (the highest numerical value and associated position), it can be used to map the spatial distribution of spectral features, which may be associated with spatial distribution of the fluorophores.

The Full Width Half Maximum (FWHM) of a spectrum is the difference between

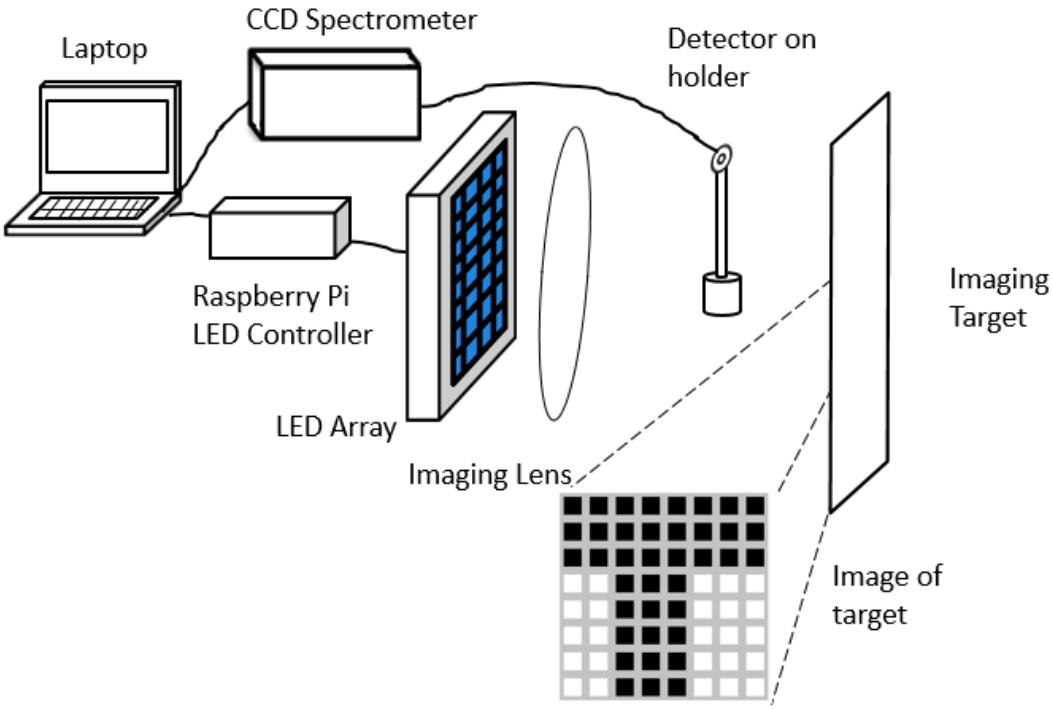

Figure 1.29: Diagram of a Hyperspectral Single Pixel Imaging setup. This is similar to Figure 1.27, but here the CCD spectrometer affords spectral imaging capabilities.

the wavelength positions of the two values that are equal to half the maximum intensity value. The FWHM gives a measure of the spectral width of the luminescence or fluorescence; it does not inherently give any information about the wavelength of the fluorescence. For this reason, it is often combined with other analysis methods such as determination of the peak wavelength, but if each different fluorophore has a different FWHM, then it can be used as an identifying feature.

A least squares fitting can be done on each recorded frame, with prior knowledge of each spectral profile. Through this, it is possible to recreate the spectra taken. The least squares fitting will then return multiplier values for each component, showing the relative emission strength of each component. If desired, the original recorded frame can be reconstructed by multiplying the returned value from the least squares fitting and multiplying it by the normalised spectra, which are then summed.

Finally, and the most involved method of the ones mentioned here, the recorded spectrum can be split into its constituent principal components, such as illumination

and each fluorophore, and is called Principle Component Analysis (PCA). This allows direct measurement of each component in every frame, along with their relative brightness, and assumes that each component is orthogonal to each other component.

1.14 Summary

In this chapter, the fundamental concepts and background knowledge for the thesis were explained. The history, theory and characterisation techniques for LEDs were discussed with an explicit interest in blue and Deep UltraViolet (DUV) LEDs. Then the fluorescent markers that are used throughout this thesis were explained, describing how they are made and used throughout all of the results chapters. Photolithography was then introduced, with its history, how photo-curing works from the optical theory to photoacid generation, film creation and patterning methods, a key technique in Chapters 2 and 3. Sample characterisation methods were also discussed. Structured illumination was then explored: how images are made, the patterns that are sent, and how this can be used in imaging and positioning. Finally, single pixel imaging, and more specifically, hyperspectral single pixel imaging were explained, as these will be imperative in Chapter 4.

Chapter 2

μ-LED based Direct Writing System

Direct writing is a type of photolithography where the radiation is focussed to a narrow beam to expose a pattern in photo-resist, a method also known as mask-less photolithography [14], [90]. The tightly focussed beam makes the mask used in flood illumination photolithography unnecessary, as moving the narrowly focussed beam or sample platform provides the spatial control for exposure that would otherwise be afforded by the mask [11]. There are two main methods of mask-less photo-lithography: either using lasers [13],[91], or LEDs [92], [93], [15], [16]. Lasers are often used as they are tightly focusable, the output wavelength is easily tunable, and they can be used at high output powers, often on the order of 10s of μW[12]. When used with digital multi-mirror displays[17], lasers can produce patterns over relatively large areas.

The main advantage that μ-LED arrays have over other forms of direct writing, however, is their direct electronic control. By using CMOS (Complementary Metal–Oxide Semiconductor), fine control of μ-LED arrays is possible, meaning that the frame rate and duty cycle (the amount of time in a given window where the μ-LED is switched on) can be externally programmed [94], [95]. This allows control of the amount of light that is hitting the sample, so that extra energy is not being wasted unnecessarily curing the sample, which would make the structures larger than intended.

This chapter discusses such a direct writing setup using μ-LED arrays for both

micro-alignment and photolithography. The experimental setup and design choices of the system will be explained. Sample handling and the photo-resist used will be discussed. The automated positioning will then be explored and the algorithm used for this detailed. Finally, the results of photolithography using the system are shown, and numerous parameters of photolithography explored for the cured structures. The key results for this chapter have been published in [1] and [2].

2.1 Direct Writing Setup

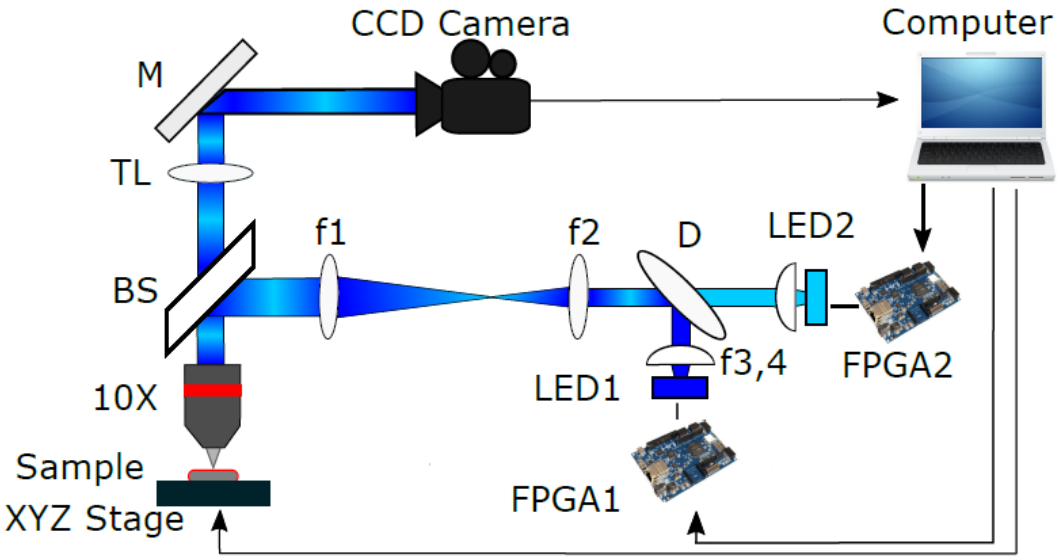

Figure 2.1: Diagram of the μ-LED based direct writing setup.

A diagram showing the μ-LED based direct writing setup is shown in Figure 2.1, which consisted of the following components:

- f1 - Spherical Lens (Thorlabs LA1461-A), f/10
- f2 - Spherical Lens (Thorlabs LA1131-A), f/2
- f3/f4 - Aspheric lenses (Thorlabs AL1210M-A - Ø12.5 mm S-LAH64), f/0.8
- D - 425 nm wavelength transmission long-pass dichroic mirror (Thorlabs DMLP425L)

- LED1 - 405 nm emitting circular μ-LED array of size 16×16, diameter 72 μm, 100 μm pitch
- LED2 - 450 nm emitting square μ-LED array of size 16×16, 98 μm wide, 100 μm pitch
- FPGA 1,2 - Xilinx Spartan 3, driven by Opal Kelly driver XEM3010-1000.
- BS - 50/50 beam splitter (Thorlabs BSW16)
- X10 - x10 Zoom Microscope Objective Lens Thorlabs (RMS10X)
- XYZ Stage - Motorised XYZ translation stage (Newport 9064-XYZ-PPP), and driver (Newport 8742-4))
- TL - Tube Lens Thorlabs TTL200-A)
- M - Mirror Thorlabs (PF20-03-P01 - Ø2 ")
- CCD Camera (FLIR CM3-U3-13Y3C)

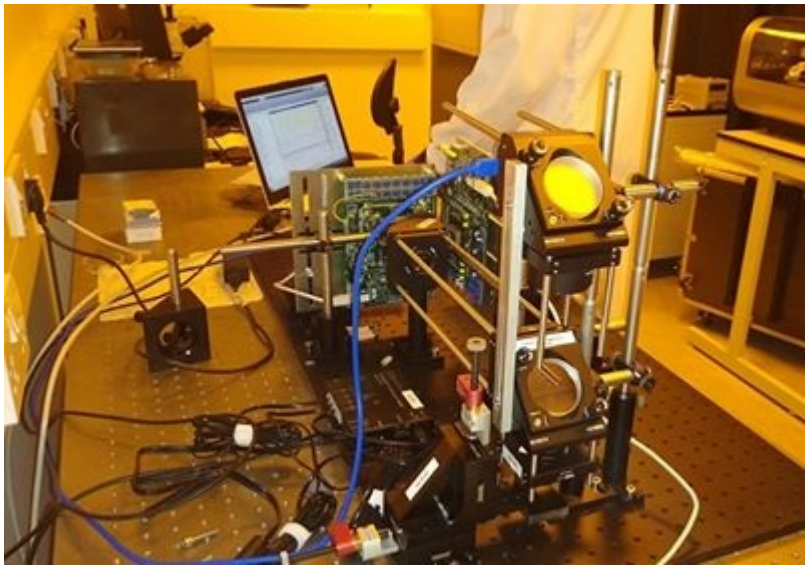

Figure 2.2: Photograph of the μ-LED based direct writing system, c.f. Figure 2.1.

A photograph of the setup is shown in Figure 2.2, and a photograph of a μ-LED array on a daughtercard is shown in Figure 2.3; the array itself is indicated by the arrow,

and was fabricated by David Massoubre as per [95]. On the left hand side of Figure 2.3, the Field Programmable Gate Array (FPGA) can be seen, with a white USB connector leading off the top left corner of the image. The FPGA module provides routing of the digital signals throughout the device and electronic test points. It also supplies voltage to the μ-LED array daughtercard and the CMOS technology that controls the μ-LED array. This device has a modular design, allowing the μ-LED array and FPGA module to be easily changed for each experiment as appropriate. The rest of the image shows the control electronics required for the μ-LED array. The arrays that were used were manufactured in-house at the Institute of Photonics. CMOS control, using technology developed at the University of Edinburgh, was used for the emitters as it allows a high frame rate and high fidelity pattern projection.

The spherical lenses are used to demagnify the μ-LED arrays, resulting in projected μ-LED spot sizes of 20 μm, for a demagnification factor of about 4:1. LED1, with its peak emission wavelength of 405 nm, is used for photo-curing and is representative of h-line photolithography, and LED2, with its 450 nm peak emission wavelength of 450 nm, is used for marker positioning. A cage system is used to simplify the alignment process for the system (see Figure 2.2); it ensures that all the optical elements are aligned with each other so that the light path is centred within the elements. The dichroic was used to reflect light at a shorter wavelength than 425 nm. With μ-LED arrays of wavelength 405 nm and 450 nm, the dichroic reflects the curing light while transmitting the positioning light at 450 nm and thus the system only requires one dichroic. The arrays are physically close to the dichroic to reduce the external light that would travel though the system.

The μ-LED Arrays are aligned so that both arrays have roughly the same Field of View (FoV) and the projected pixel illumination is the same between the arrays. This required full control over the alignment and position of the arrays in relation to the dichroic, and many rounds of alignment of the distance between the μ-LED array and the dichroic. The coupling of the μ-LED array into the system also requires fine control, enabled by mounting the μ-LED array on an XYZ precision stage. Figure 2.4 shows the emission spectra of the two types of μ-LEDs used in this work; the violet μ-LED

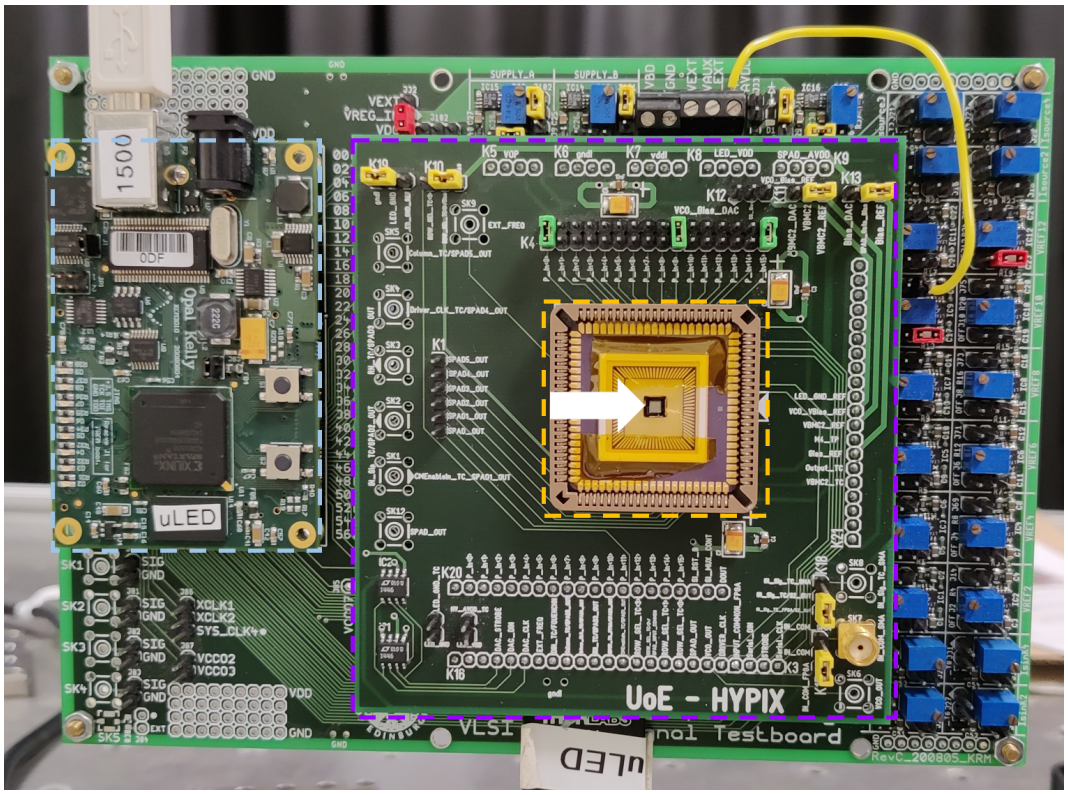

Figure 2.3: Photograph of a μ-LED array used, with the white arrow pointing to it. The CMOS/μ-LED array itself is held within the orange dashed square, on a daughter card, which is the PCB surrounding the array, in the purple dashed square. The daughter card is placed attached to a larger motherboard. Also connected to the motherboard, to the left of the μ-LED array daughtercard is an FPGA board (the cyan dashed rectangle) with a USB cable out of the top of it, connecting it to the controller PC and is the only external connection from the board.

has a FWHM of 12.95 nm, whereas the blue μ-LED has a FWHM of 16.5 nm. The spatial output of the μ-LEDs in good approximation followed a Lambertian emission pattern, where the output is proportional to the cosine of the angle between the line of sight and the surface normal to the μ-LED [21]. The 450 nm emitting μ-LED array was chosen for the structured illumination based positioning, as its wavelength did not cure the photoresist and has a high fill factor of 99 %.

While an XYZ stage was used in this system, the focus in the z-axis was found by eye. Methods are available to actively control and adjust focus during operation, and these could in principle be used alongside the method described here. The stage was first used to align LED2 with an alignment marker by means of the process described

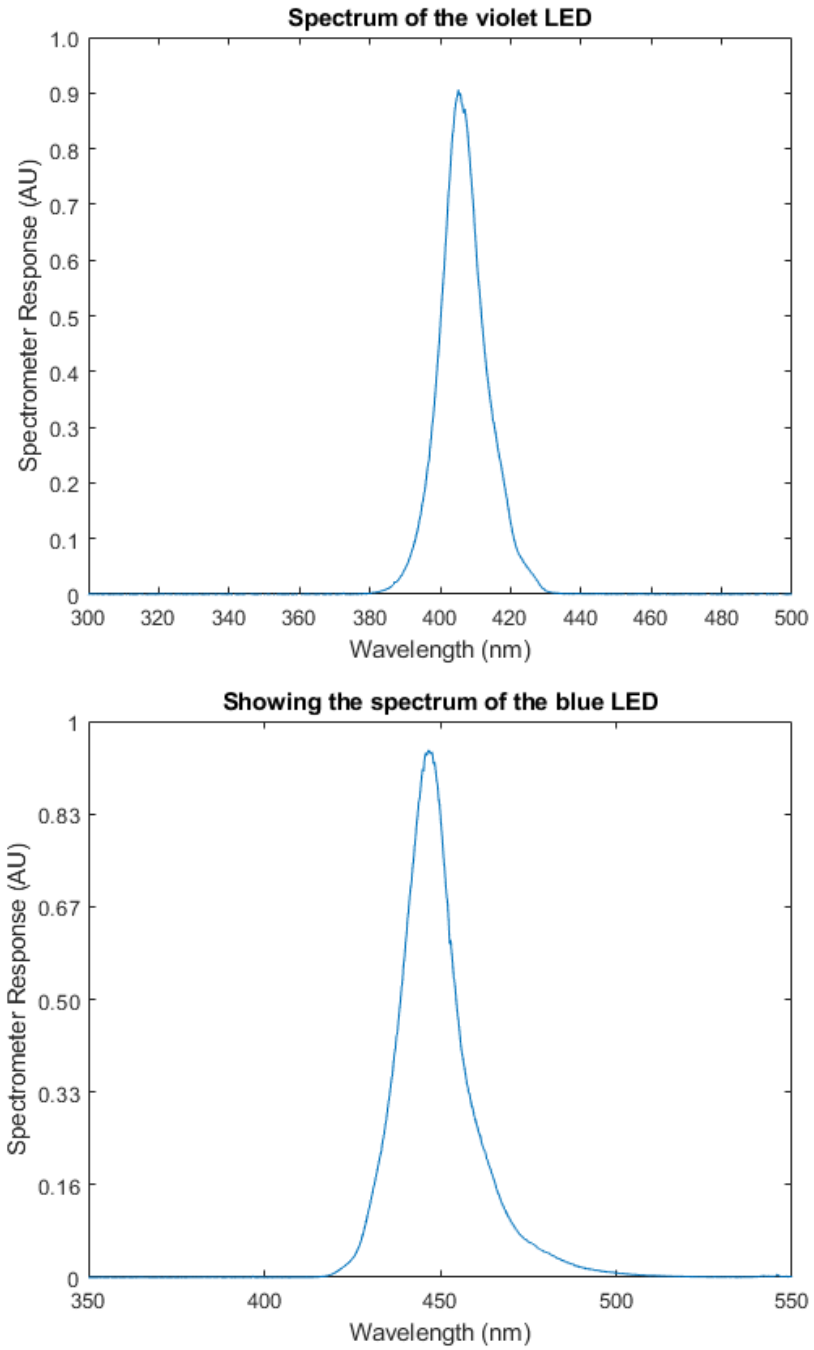

Figure 2.4: Emission spectra of the μ-LED types used in this chapter. Top: A violet LED with a peak wavelength of 405 nm. Bottom: a blue LED with a peak wavelength of 450 nm.

in Section 2.3, and then in a second step it was also used during photolithography. Photo-resist structures were made by moving the stage with a single 405 nm μ-LED curing the photo-resist.

2.2 Sample Preparation

Throughout this thesis, borosilicate glass slides have been used as a substrate for photolithography.

The glass slides were first cleaned, by use of a triple solvent rinse. The slides were placed in a glass dish, with enough space for them to not overlap each other. Then acetone was poured over the slides to cover them, the dish placed in a ultrasonic cleaner, which was operated for 5 minutes. Afterwards, the acetone was poured out, taking care to not pour out the slides. This process was repeated with methanol, iso-propyl alcohol (IPA) and deionised (DI) water. After the DI water was poured out of the dish, the glass dish was placed on a hot plate at 110 °C for 20 minutes, keeping an eye on the slides and occasionally moving them so that they were easily removable after drying.

When illuminated with a pattern sequence from the 450 nm μ-LED array, micron-sized fluorescent markers placed on the sample can result in a fingerprinted spatio-temporal fluorescent emission. This enables the system to self-calibrate for position-defined direct writing into photoresist. Two types of fluorescent markers were used in this Chapter: red-emitting CdSe colloidal alloyed core Quantum Dot (QD) clusters, 20 μm in diameter and fluorescent dyed micro-beads, (Cospheric fluorescent red polyethylene micro-beads), 10-25 μm in diameter. The excitation spectra of the beads are shown in Figure 1.11. The term "marker" used henceforth refers to both the QD clusters and the micro-beads, and the experiments shown here can be done with either marker type.

When using the QD clusters as markers for positioning, they need to be added to the substrate before the photo-resist is applied. The clusters were chosen for their fluorescence at 630 nm, absorbance at 450 nm and incorporability in water. The QDs were mixed in DI water and were drop cast onto the glass substrates, then allowed to evaporate to dry at room temperature. It was found that one to two drops of QD

clusters was enough in this process. The photo-resist was then applied, also drop cast onto the substrate. Enough drops of photo-resist needed to be applied for a thin film to be visible after spin coating; for a 10×10 mm^2 glass slide, two drops of photo-resist were required, and for a 15×15 mm^2 slide, 5 drops were required. The sample was then spun on a spin-coater at 3200 rpm for 20 seconds.

With the micro-beads, these were directly added into a small amount of the photo-resist, which was then drop cast onto the sample and then spun at the same spin speed as before. The photoresist that was used was a UV sensitive resin (brand Anycubic), originally designed for 3D printing, due to its sensitivity at the curing wavelength of μ-LED1 at 405 nm, while being unaffected by the wavelength of μ-LED2 at 450 nm. A concentration of approximately 2 mg of beads per ml of photo-resist was found to work well and struck a balance between having enough beads to find them easily without much wastage, while also having a low enough concentration to have only one bead in the FoV. It is important to have only one bead in the FoV for the positioning algorithm to work properly, as will be explained in section 2.3.

After photo-curing, acetone was applied to the sample to develop it by submerging the sample in a glass dish with acetone and gently agitating for 30 seconds. This removed any uncured photo-resist. The sample was then cleaned following the triple rinse procedure detailed above, but for only 30 seconds in the ultrasonic bath for each solvent rather than 5 minutes. The sample was then dried by gentle application of a nitrogen gun.

2.3 Automated Positioning

This section covers the automated positioning, the algorithm that was used for positioning, and how this was applied practically within the autonomous direct writing system. Automated positioning offers many advantages. It can be quicker and more precise than manual alignment, due to the computing power behind it and the increase in positioning resolution offered by autonomous systems [96], [97]. The autonomy of the system allows feedback loops to input the measured position of the marker back into the setup, allowing for numerous alignment steps during positioning, known as

closed loop process control [98]. The positioning can be directly linked to the photolithography capabilities, so that curing can start immediately after positioning, without human interaction [2].

The first thing to consider was the speed of the system. This was limited by the computer's ability to read and write pictures to and from the hard drive, and the largest camera frame rate that could be reliably achieved was 12 Frames Per Second (FPS). In order to provide sufficient margin to the Nyquist-Shannon sampling limit, 3 camera frames were taken per illumination frame, so the system was ran at 4 FPS.

2.3.1 The Automated Positioning Algorithm

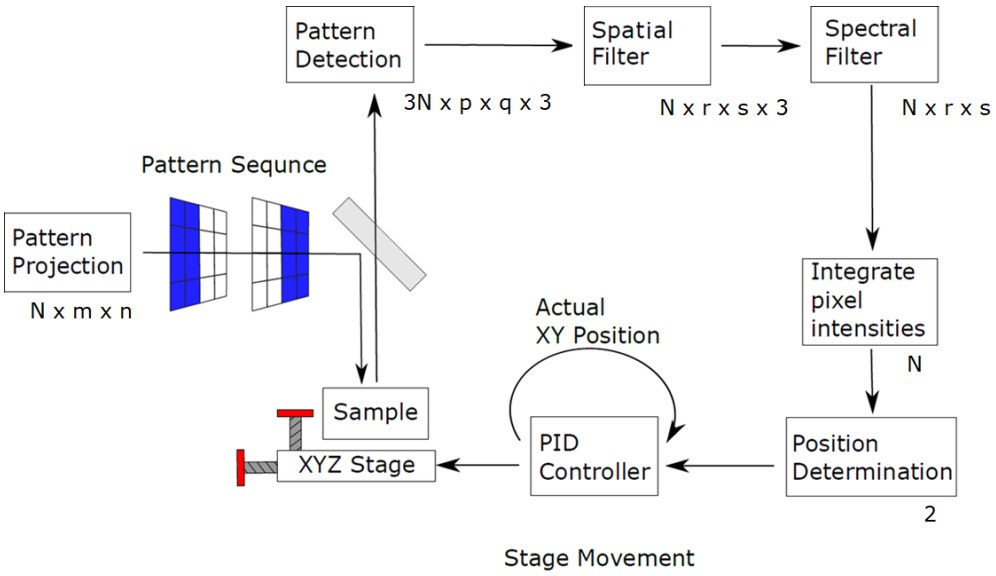

Figure 2.5: System Flow Diagram of the automated positioning. The dimensions of the output from each step are noted. Here, N is the number of frames, m and n are the LED array co-ordinates, p and q are the dimensions of the CCD camera, and r and s are the dimensions of the spatial filter.

Figure 2.5 shows the system flow diagram for the automated positioning algorithm, with the dimensions of the data cube after each step in the system flow diagram listed underneath that step. Firstly, N patterns of size $n \times m$ are projected. These are detected by the camera, which takes 3 pictures of size $p \times q \times 3$ for each projected

pattern, where p and q are the dimensions of the CCD camera's detection pattern and the 3 is from the three colour channels for each image, Red, Green and Blue, for a data cube of size $3N \times p \times q \times 3$. The middle frames of each pattern projected by the μ-LED Array are selected for analysis. Then the spatial and spectral filters are applied to the frame and the intensity of pixels that meet both criteria are summed. This results in a single numerical value for each projected pattern, allowing the ideas of single pixel imaging as described in Section 1.13 to be used. The rest of this section will describe these steps in further detail.

The spatial filter, as shown in Figure 2.6, is required as the edge of the μ-LED die is reflective. Therefore, some edge μ-LEDs are seen twice by the camera, as light is being coupled through reflection off the die edge. In Figure 2.6a, the μ-LEDs at the left hand edge of the array can be seen twice, along with a (in this case reflective) target in the projected μ-LED array. As a result, the FoV of the camera is artificially reduced by selecting the area over the projected μ-LED array, removing the reflections, and this area is used for positioning, as shown in Figure 2.6b. The size of the data cube after the spatial filter is an image of size $N \times r \times s \times 3$, where r and s are the dimensions of the spatial filter.

The spectral filter is then applied to only show the fluorescence in the images. An RGB CCD camera stores images in three channels, respectively corresponding to Red, Green and Blue detectors on the CCD Camera. The frames corresponding to the Red, Green and Blue channels for each image are extracted, which because the illumination and fluorescence are different colours, allows the filter to be applied. This is done by applying a minimum and maximum value for each colour channel that corresponds to the fluorescence, so that the only pixels that are counted are the ones that have colours that resemble the fluorescence. This results in a binary mask for the image. The output of the spectral filter, when applied to the full data cube, is a data cube of size $N \times r \times s \times 3$, with the pixel values unchanged if they are within the spectral filter, and 0 otherwise. Figure 2.7 shows what happens during the spatial filter, with a fluorescent bead.

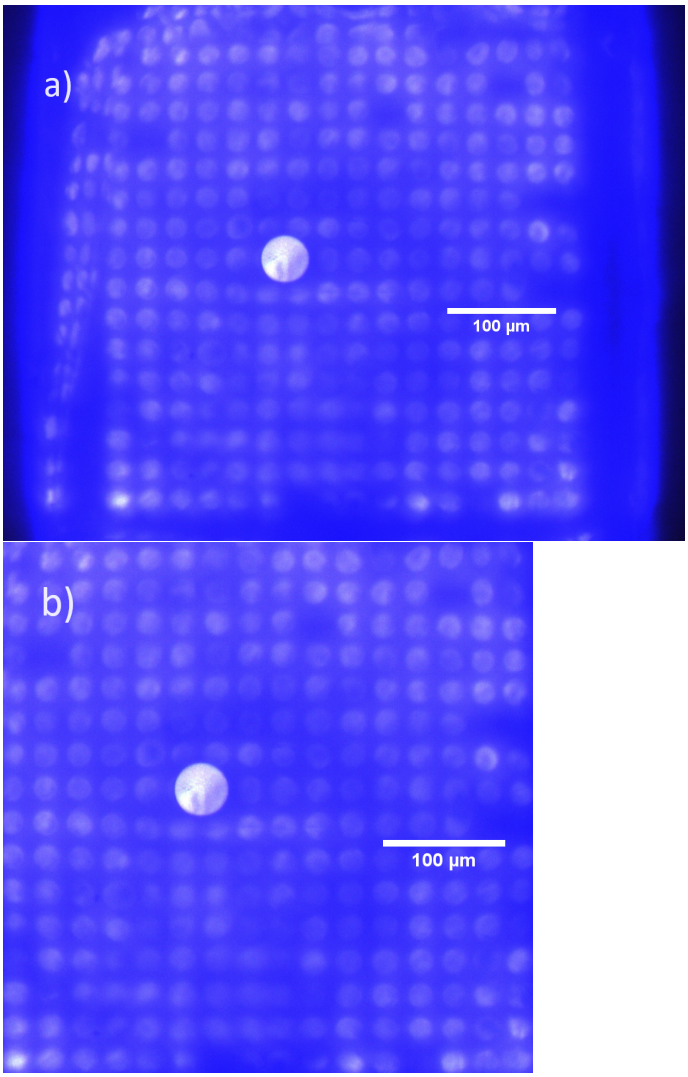

Figure 2.6: This shows the effect of the spatial filter. a) shows a bright reflective target in the projected μ-LED array. The reflection off the LED die can be seen on the left hand side of the image. b) shows the same area as a) with the spatial filter applied.

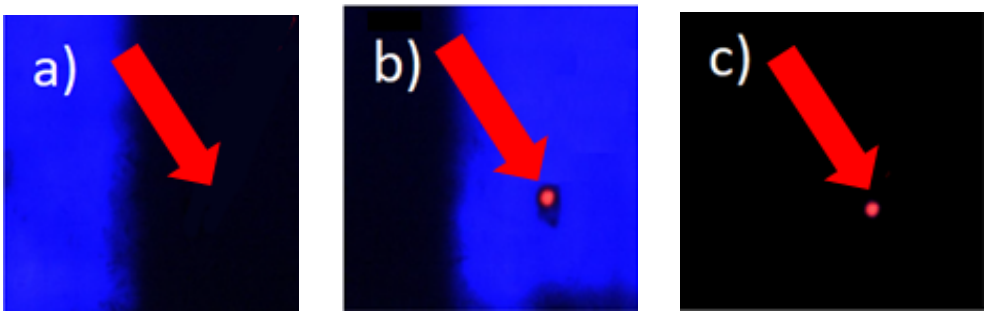

Figure 2.7: Shows a fluorescent bead during the positioning process. a) shows the bead when it is not illuminated. b) shows the bead when it is illuminated by the blue μ-LEDs. c) shows b) after the spectral filtration process is done to it. The blue areas in a) and b) are representative moving bars patterns from LED2.

After the spatial and spectral filtering, each image is then summed, to count the intensity of pixels in that image are within the spectral filter, summing over all three colour channels to output a single value for that image. This results in a data cube of size N for the whole positioning dataset, one value per image, to make the Temporally Modulated Fluorescence (TMF).

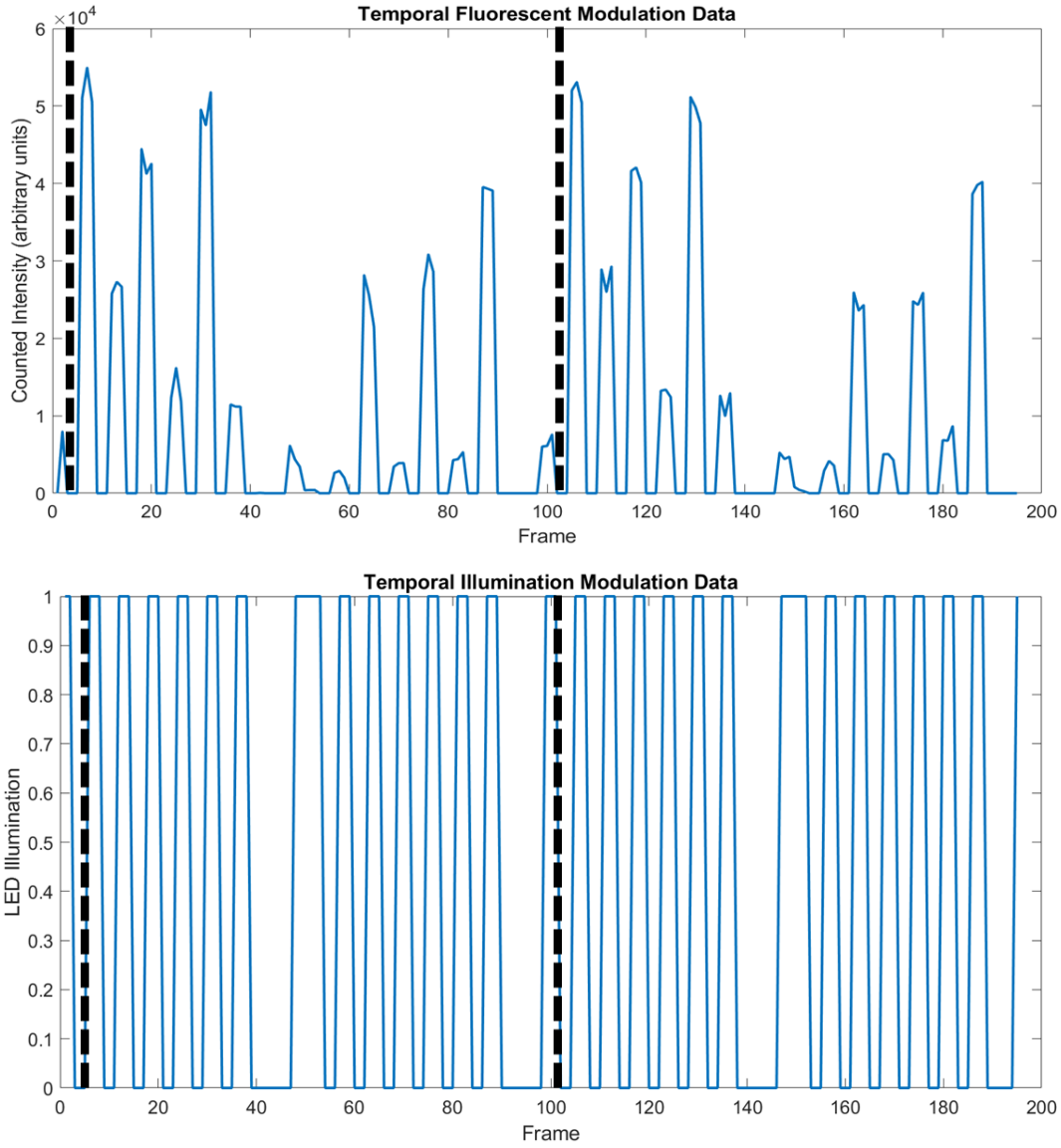

Figure 2.8: Example TFM data taken of a marker (a, top), and the Temporal Illumination Modulation (TIM) data at that position (b, bottom). The bold dotted line shows the start frame of the illumination pattern.

These TMF data are shown in Figure 2.8 a), which shows the spectral response from each measurement recorded for a representative marker at a random position in the FoV of the blue μ-LED. As each measurement is shown, the three measurements taken per pattern in the sequence can be seen, where values roughly match in groups of three. The bold dotted line shows the start frames used in the system, with the earlier start frame used for positioning as that will have the full imaging sequence, and the middle frame from the sets of three used as the single pixel imaging dataset used for positioning.

The large difference shown in Figure 2.8 a) between the on and off frames when the marker is fully in the illumination of the μ-LED array reduces the inherent errors when using this data for positioning purposes. While it might be expected that the data have higher values when within the μ-LED illumination, closer to a binary data set, the marker might be on the edge of a particular pixel during the positioning. This would mean that less illumination would fall upon the marker, thus reducing the resulting fluorescence. This could potentially be considered as the basis for a sub pixel positioning arrangement, where if the data can reliably show this, positioning within a pixel's projected spot size might be possible.

Figure 2.8 b) shows the Temporal Illumination Modulation (TIM) data, the illumination of the μ-LED array at the marker's position. As a simulation, the TIM data is a binary encoded sequence and is compared with the TFM data (Figure 2.8 a)) as a Ground Truth for positioning. There is a strong correlation between the TFM and TIM data sets, showing that this method of positioning works well.

In order for the positioning to have any real meaning, co-ordinates need to be assigned in the FoV of the chequerboard illumination array. This allows visualisation of the marker in the μ-LED array illumination and gives a familiar numerical result from positioning. Here, the same coordinates as originally designated within the μ-LED array are used, so that (1,1) in the algorithm refers to the μ-LED designated (1,1) in the array. This allows consistency between the μ-LED array and the positioning algorithm.

To output a co-ordinate value, the TFM data were first analysed to determine which

frames the marker is present in through each frame's summed intensity value, resulting in a binary sequence of numbers for each axis in the projected μ-LED illumination. With the moving bar pattern (see Section 1.11.5), each position in the array has a unique sequence associated with it [76]. In each axis, the associated sequence and the measured sequence for each position was compared and the difference calculated. To find the position of the marker in the array, a brute force minimum search is applied to the sequence, with the position with the lowest difference between the measured and associated sequence is output as the position in that axis. From an initial data cube of size $3N \times p \times q \times 3$, 2 values were output from the algorithm. This algorithm was simple to implement and has little computational difference when compared to the extra development time required for a more sophisticated algorithm to be made.

The determined position is then compared to the marker's target position, with a PID loop (Proportion, Integration, Derivative, see Section 1.8.6) used to control the movement of the marker. The entire positioning is then redone to check that the marker is at the correct position, and if required, more cycles of positioning are done, which circumvented inaccuracies in the hardware.

Figure 2.9 shows the results of aligning a randomly placed marker, here seen to be at coordinate (13,11) on the CCD camera, which was then moved to a pre-designated target location of coordinate (15,15). Figure 2.9a) shows, as a function of time, the movement in one axis, designated the x-axis, and b) shows the movement in the y-axis, orthogonal to the x-axis. Two cycles of movement were required to get to the target, requiring three cycles of positioning: one to establish the starting position and then one after each cycle of movement. In this Figure, the actual position is the position seen on the CCD camera, with computed position the output of the positioning algorithm. There is a slight discrepancy between the two initially, and after the first movement cycle, but the two eventually come together with the algorithm eventually outputting the target coordinate, showing that the system is capable of positioning to a pre-designated target position. The starting discrepancy might stem from the initial position of the marker within the projected μ-LED spot. If the marker was at the edge of the spot, then the algorithm may erroneously output the neighbouring coordinate.

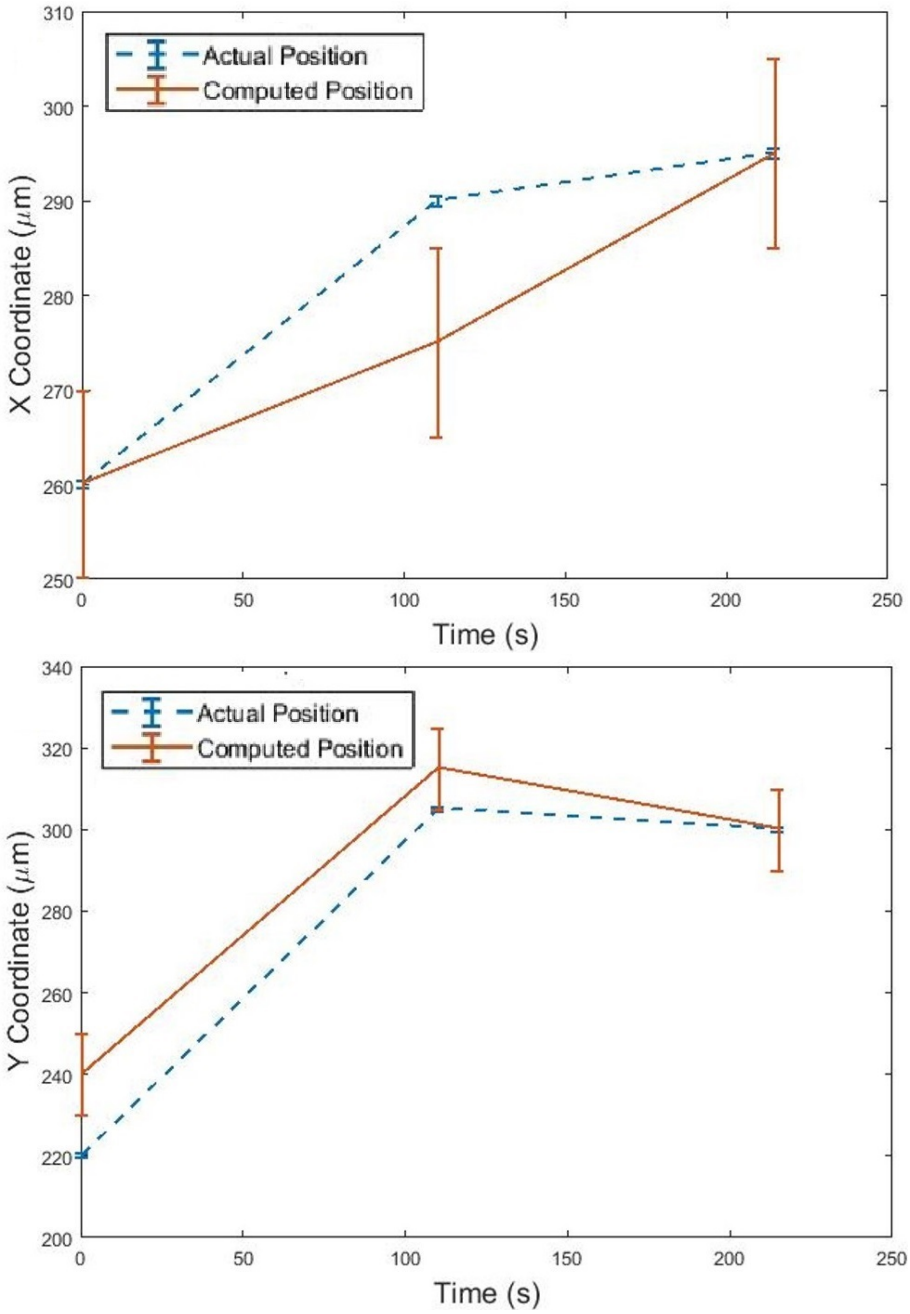

Figure 2.9: Plots showing how a marker's computed and measured position changes with time. The Actual position used the CCD camera to establish the position of the marker, with Computed position being the output of the positioning algorithm.

2.4 Photolithography

2.4.1 Structures made

After the sample has been prepared, the markers added, and the sample aligned, photolithography can begin. Photo-curing was done with a single 405 nm μ-LED to increase the curing dosage of that μ-LED, and to reduce cross-talk between μ-LEDs. Using multiple 405 nm μ-LEDs results in dead zones between projected spots, due to the 41 % fill factor of the device used, meaning that the resulting structures will not be uniform. Curing was initially done by turning the 405 nm μ-LED on for 100 % of the time and moving the motorised stage as quickly as possible. Figure 2.10 shows a structure cured using the system without the positioning; this was done as proof that photolithography could be done with this system and that patterning lines, right angles, and crossing over the same area were all possible. The structures in Figure 2.10 are approximately 65 μm wide, larger than the μ-LED spot size of 20 μm, which is expected to be the smallest structures possible with this system.

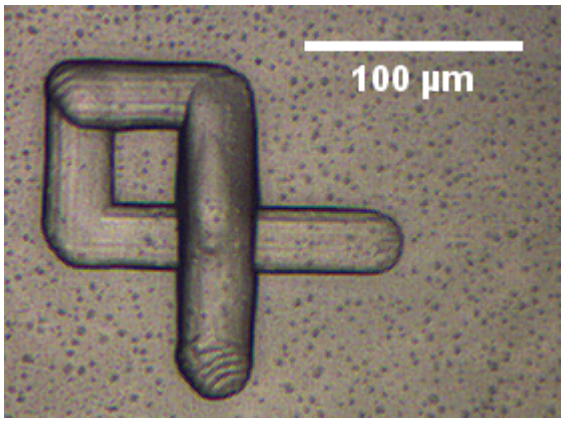

Figure 2.10: Example of a structure cured in the Anycubic resin. The dots seen in the background are excess resin that has not been washed off.

Figure 2.11 shows the first structure that was cured with the positioning: at the centre of the cross, there is a fluorescent colloidal quantum dot cluster used for positioning, inside the orange circle. The position was carefully chosen due to the fact that the cluster was the only one visible within the FoV of the μ-LED board during positioning. This shows that the system is capable of multi-step alignment during curing.

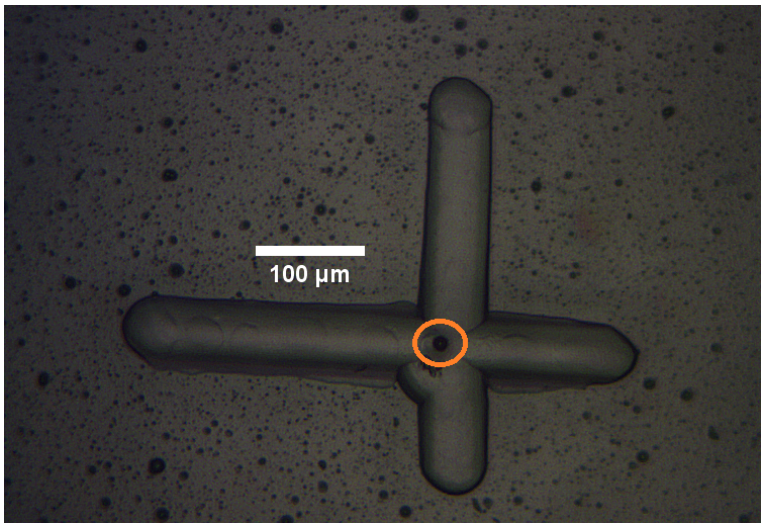

Figure 2.11: Micrograph showing the first cross made with the automated positioning tool. A positioning QD cluster can be seen in the centre of the cross, in the orange circle.

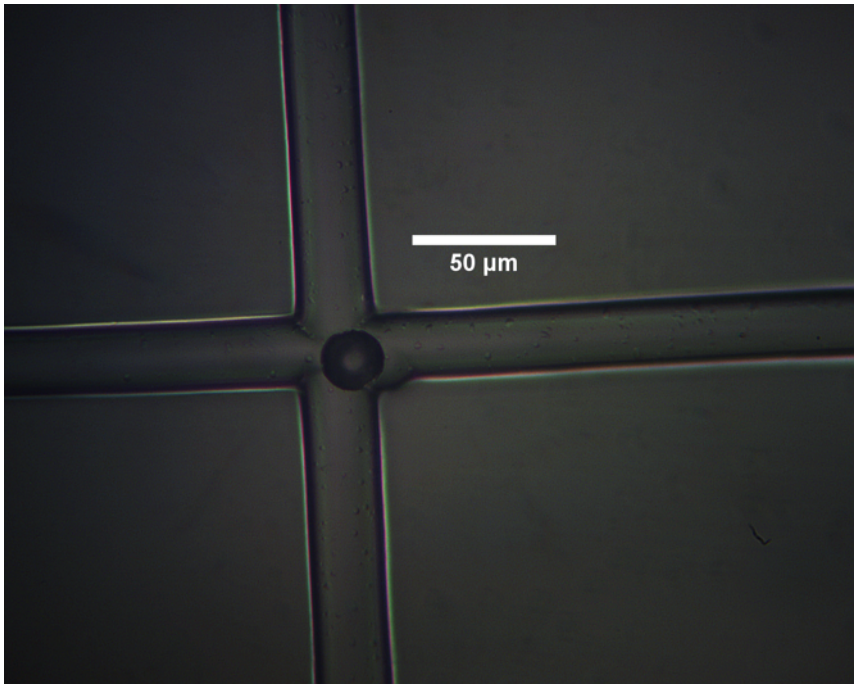

Figure 2.12: Micrograph of a cross shaped structure cured with a marker bead in the centre of the cross, showing how the positioning can be accurately done multiple times.

Figure 2.12 shows a sample similar to Figure 2.11, where the triple rinse was done, showing how much cleaner the sample is after the triple rinse, forming the standard

for the post-curing procedure. This structure was cured after the duty cycle work was undertaken later on in this Chapter to finalise the settings used.

The fluorescent markers can be used for more than purely alignment. When the markers are embedded into the photoresist, as they are here, they offer the possibility of further functional use; for example, the marker can be embedded into a polymer waveguide. This allows the fluorescence from the marker to be guided away from the marker's original position by a polymer waveguide, allowing its detection elsewhere on the sample. Figure 2.13 shows a structure similar to that shown in Figure 2.12 when imaged via an environmental SEM (thanks go to Emma Butt of the University of Strathclyde in assisting with acquiring Figure 2.13).

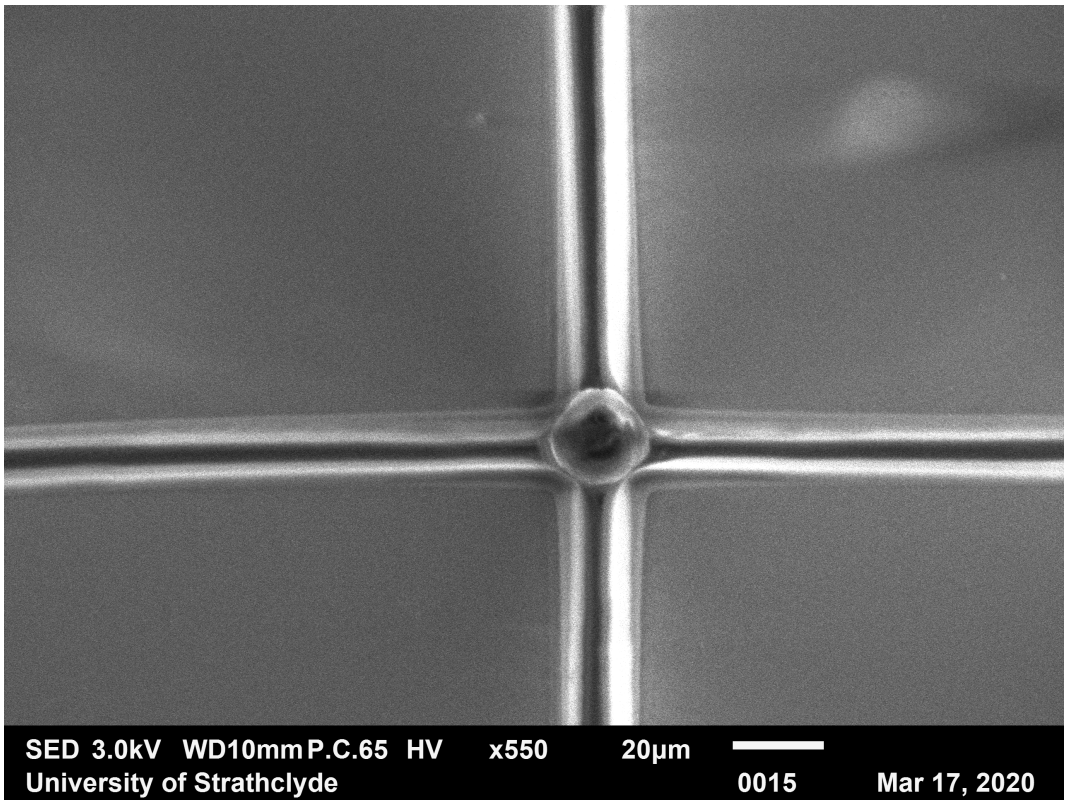

Figure 2.13: An ESEM of a sample similar to the one shown in Figure 2.12, but with cured features below 20 μm in width.

2.4.2 Characterisation of the structures

The structures in Figure 2.10 are approximately 65 μm wide at their widest, larger than the μ-LED spot size of 20 μm. This is because the dosage is too high and a result of the Lambertian output of the LEDs, where the curing dosage will be dependent on the cosine of the angle between the surface normal and line of sight [21]. Therefore, as the curing dosage increases, so too does the area cured. The dosage is dependent on a few factors, mostly the stage speed and the output μ-LED power [15], as will be explored in Section 2.4.3. Having a higher stage speed reduces the dosage, but the stage was already set to the maximum speed here. The CMOS control of the μ-LED array, while capable of many things, is not capable of reducing the μ-LED output power due to the binary control it offers. However, the duty cycle of the μ-LED, the percentage of time that the μ-LED is on in a given period, can be reduced. The CMOS control affords change in the frame rate and duty cycle (the percentage of time that the LED is switched on) of the curing μ-LED separately, giving fine control of the dosage.

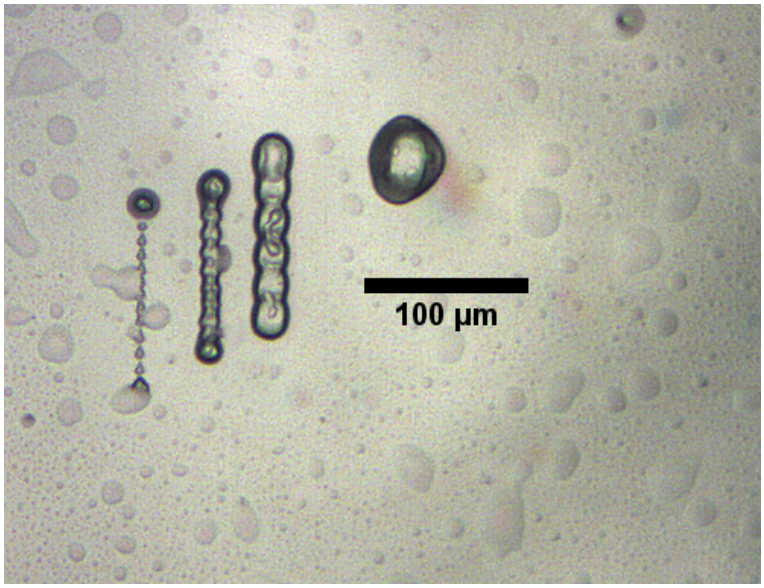

Figure 2.14: Micrograph of a sample where the frame rate and duty cycle were changed simultaneously while curing, while their product remained constant. It was thought that this would keep the dosage the same. The structures seen used a period length of 1, 0.5 and 0.4 s, respectively. More structures were cured, but the dosage was insufficient to cure the photo-resist.

It was originally thought that with a higher frame rate, a lower duty cycle was needed in order to keep the dosage the same. Figure 2.14 shows a set of structures made by the photolithography system where the product of the frame rate and duty cycle was 0.031. A reference dot was cured to orientate the sample, seen at the right of the figure, and then lines were cured with a series of frame rates and duty cycles, with the product of the two was kept at 0.031. It was thought that this would keep the dosage the same. However, not all the structures can be seen, signifying that they have not been cured sufficiently; the structures being a series of dots rather than solid lines shows the effect of period length on the cured structures. This figure shows that instead of a combination of the frame rate and duty cycle, only the latter affects the curing dosage, and that the higher the frame rate, the more dots are in the cured structures, eventually becoming a smooth line.

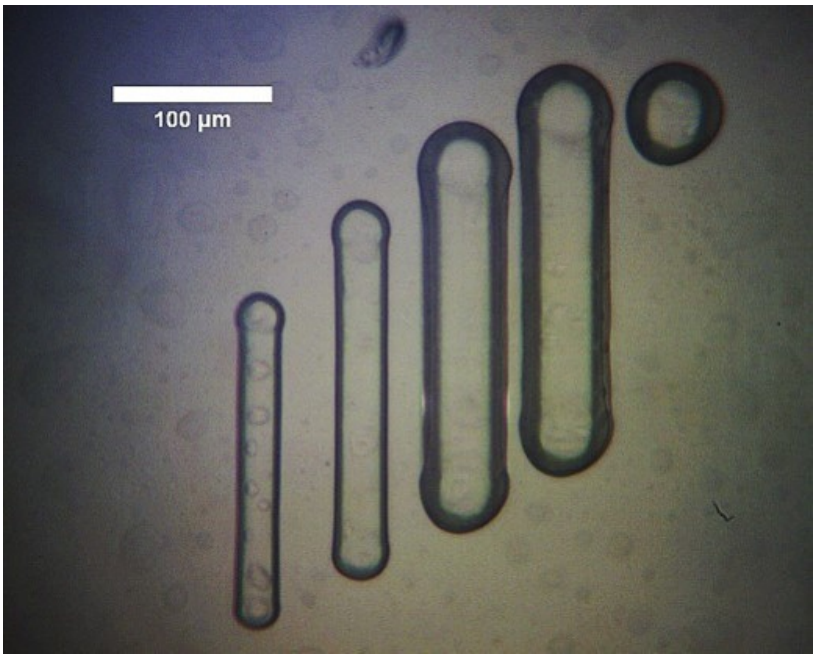

Figure 2.15: Micrograph of a sample where the duty cycle is changed between each structure cured, with a 100% dot cured for orientation purposes. Duty cycles used for this sample: 100%, 50%, 10% and 5% are visible. A duty cycle of 1% was used, but did not cure structures.

To test this, Figure 2.15 shows the effects of changing the duty cycle of the curing μ-LED by curing lines with different duty cycles, at 500 FPS. The duty cycles used were

as follows, from right to left: 100, 50, 10, 5 and 1 %. The large dot at the far right was again made to orientate the sample. There are only 4 lines visible in Figure 2.15 as the 1 % duty cycle did not cure the photo-resist and was washed away during development. As the frame rate was increased, so too were the smoothness of the structures as shown previously. Because of this, frame rate was kept as high as possible; the rest of the structures in this chapter were cured using a frame rate of 500 FPS.

Figure 2.16 graphically shows the relationship between duty cycle and cured structure width; the shape of the graph indicates that the cured structures near 100 % duty cycle were reaching the maximal structure width available with that size μ-LED [99]. Combined with Figure 2.15, this confirms that the size of the cured structures is affected by the duty cycle, and is directly proportional to the curing dosage.

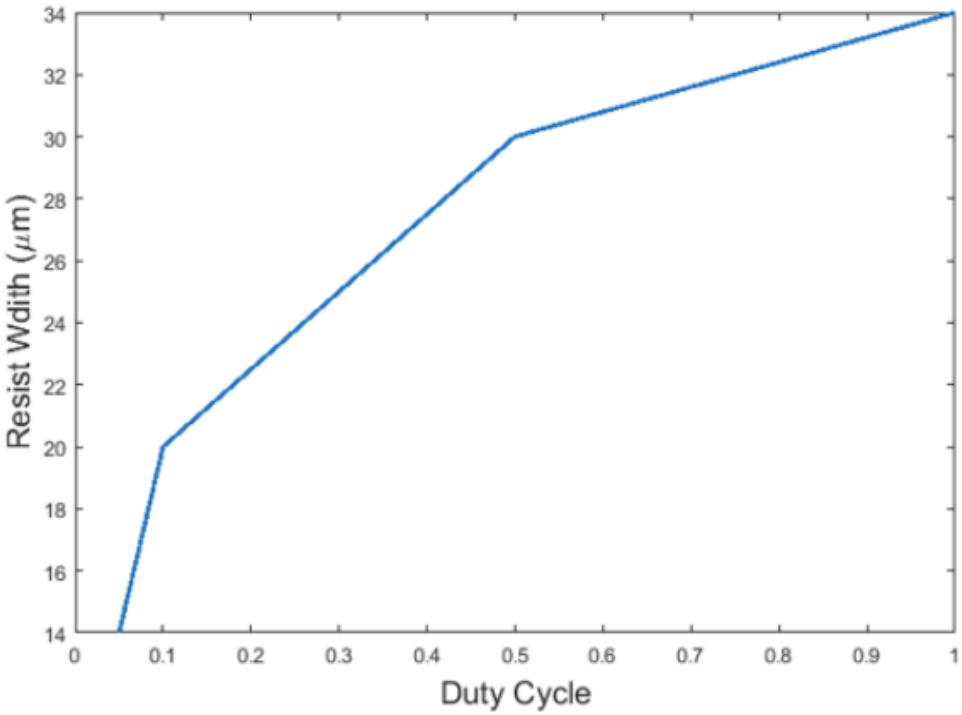

Figure 2.16: Graph showing how the width of the cured structures from Figure 2.15 change with duty cycle of the curing μ-LED.

While the structures made are smooth, some of the samples are dirty. For example, quantum dot clusters can be seen around the structure in Figure 2.11, requiring the

sample to be cleaned properly after curing. In order to do this, a triple rinse in an ultrasonic bath was used, where a small glass dish was filled with acetone and the sample placed inside, which was placed in the ultrasonic bath for 30 seconds, removed and the excess acetone discarded. This was then repeated with methanol, IPA and DI water before being air dried. The sample could be placed for longer in the ultrasonic bath, but this showed little improvement in the cleanliness of the sample, and affected the structure itself. Figure 2.17 shows the underside of a sample with a cured cross after too much cleaning in an ultrasonic bath. The edges of the structure can be seen to lift off the sample, evidenced by the out of focus parts, shown here in white. The under-etching is particularly visible at the top of the sample, on the right hand side. To reduce this effect on the structures, 30 seconds was chosen for the duration in the ultrasonic bath.

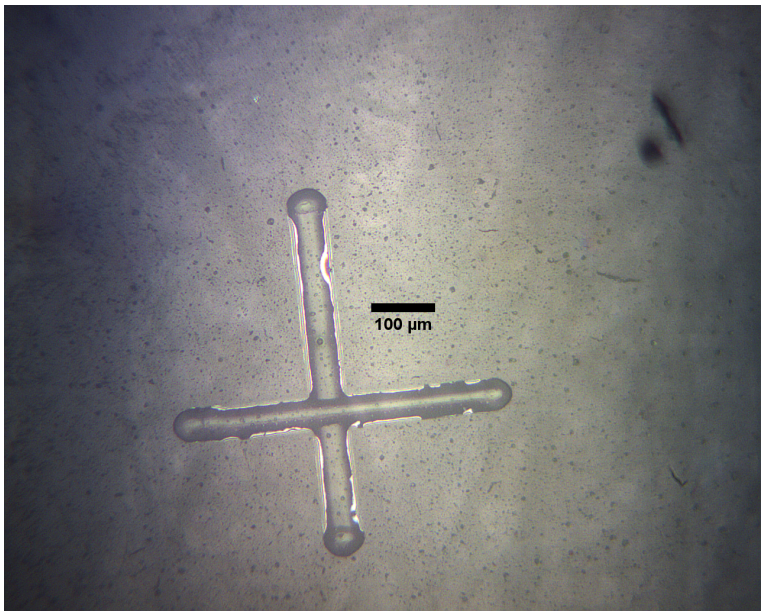

Figure 2.17: Micrograph showing the underside of a cured structure after cleaning. The edges of the structure are starting to peel away.

2.4.3 Dosage Calculation

It is important to calculate the dosage of the photolithography system. This is covered in more detail in Section 1.9, but the equation that was used for estimating the maximal

dose in the centre of the moving photolithographic structures was given as [15]:

$$E = \frac{2P}{\pi R v} \tag{2.1}$$

Where E is the dosage in Jm^{-2}, P the illumination power, R the distance from the centre of the photolithography source, and v the stage speed. Therefore, in order to estimate the maximal dosage by the photolithography system, the size of the projected μ-LED spot, the speed of the stage, and the power of the curing μ-LED all need to be measured.

To measure the projected spot size of the μ-LED, a sample with a previously known size can be used as the basis. For this estimation, a reflective sample of size 300 μm was used, originally a template for μ-LED array manufacture. The exact metallic composition of the reflective sample is unknown. A microscope image of the reflective target used for the spatial calibration is shown in Figure 2.18. There are 8 circular, reflective targets of diameters between 20-500 μm. All of the μ-LEDs will then be turned on and the reflective sample placed at the sample position. The amount of μ-LEDs that light up that can be seen using the visible sample with one of the larger targets can then be used as an estimate of the projected spot size. A larger target is used to get a better estimation of the μ-LED size. Figure 2.19 shows said reflective sample with all the μ-LEDs on, which can be seen on the centre-right of the image. Nine μLEDs fit within the 300 μm reflective target, between the green lines, estimating the spot size as 33.3 μm across.

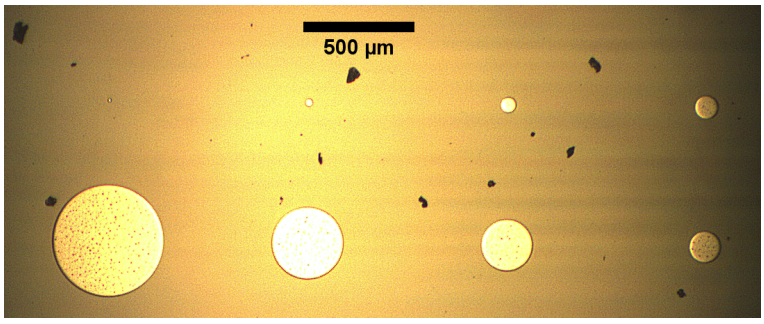

Figure 2.18: Shows a microscope image of the entire reflective target used during spatial calibration. The circular reflective targets are, anticlockwise from the bottom left, 500, 300, 200, 100, 80, 60, 40, and 20 μm in diameter, respectively.

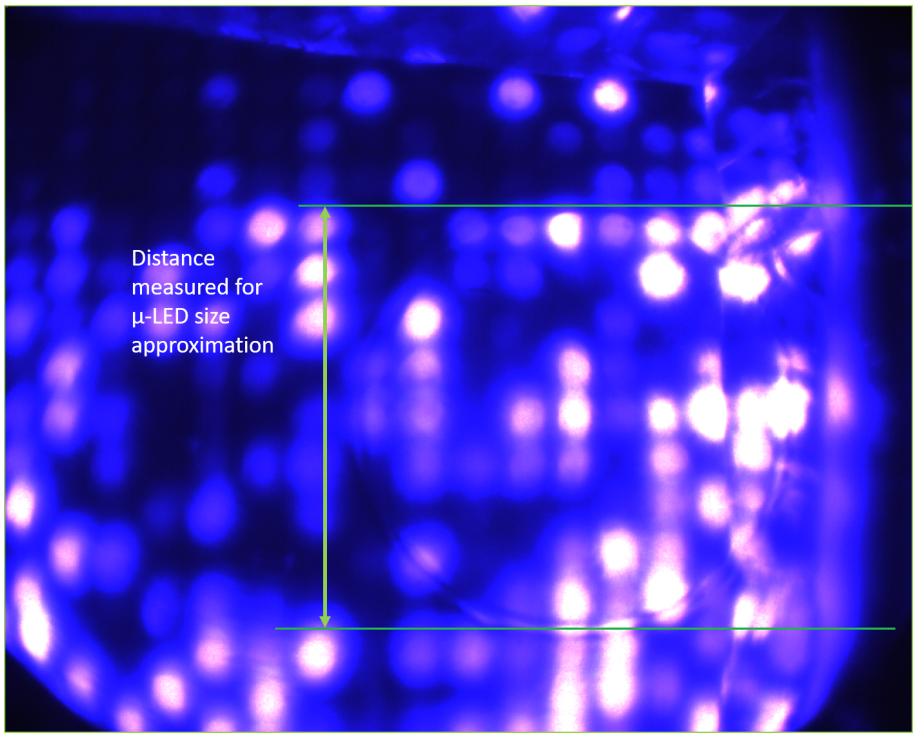

Figure 2.19: Shows the curing μ-LEDs on the 300 μm reflective target. The green lines indicate the distance that was used to measure the 300 μm wide target: the target outline can be seen within these lines.

To measure the stage speed, the time taken to move to move 7 projected spot sizes was measured and repeated several times for accuracy. This averaged out at 3.4 seconds. Given that the spot size is approximately 33.3 μm, this estimates the stage speed at 68 μms^{-1}. This was done at the maximum stage speed value of 2000; reducing it had an inconsistent response on the distance travelled and the speed recorded.

To measure the power of the curing μ-LED, an optical power meter head was placed at the sample position and the curing μ-LED was turned on using the same conditions (duty cycle and frame rate) as used during photo-curing. The Thorlabs S120VC power meter head was connected to a Thorlabs PM100A power meter and the head was moved until the maximal reading of the μ-LED power was recorded, this being 7.8 μW.

Inserting these values into Equation 2.1 estimates the maximum dosage of the photolithography setup as 2200 Jm^{-2} or 220 $mJcm^{-2}$. The manufacturer for the photoresist does not make the curing data available to the public due to the resist's intended

use in a 3D printer.

2.4.4 Optical Profiler Data

An important aspect of characterising the photolithographic structures made is the spatial profile of the cured structures, see Section 1.10.1. This not only confirms the width of the structures, but also measures their height and shape. The results here will present the height of the structures in the axis perpendicular to the stage movement, and can show if the curing setup is misaligned, along with the relative over- or under-curing of the photo-resist.

The profiles were taken using a Veeco NT1100 optical profiler, allowing accurate measurement of the profile and the structure sizes using light as a non-invasive measuring tool. Thanks go to Jack Smith of Strathclyde University for assistance in acquiring these images.

Figure 2.20 shows the profile of the same sample as shown in Figure 2.15. The sample and the profiler are aligned identically, so the structure on the far left is the 5 % duty cycle structure, going to the 100 % duty cycle structure on the right. This is proof that as the dosage increases, so too does the width and height of the structures, implying that over-curing results in over sized structures. The 50 and 100 % duty cycle structures have similar height and widths, showing that the photo-resist was spun to a height of 7 μm, and that the over-curing was approaching the maximal value at these dosages. The additional bumps shown in the cross section profile are from dust, debris, or droplets of unwashed photo-resist.

Figure 1.22 shows an image of the sample in Figure 2.12 in the optical profiler. The structure is approximately 9 μm high, and the numbers on the image are the measurement of the length of the cured lines, being 461 and 615 μm respectively. The lines have similar height throughout, showing the uniformity of the curing dosage. This is due to the stage speed being uniform during curing. Figure 1.22 measures the width of the profiles as 25 and 29 μm, respectively, compared to the 34 μm estimated by the imaging system, with Figure 2.21 showing where in the structures the profiles were taken.

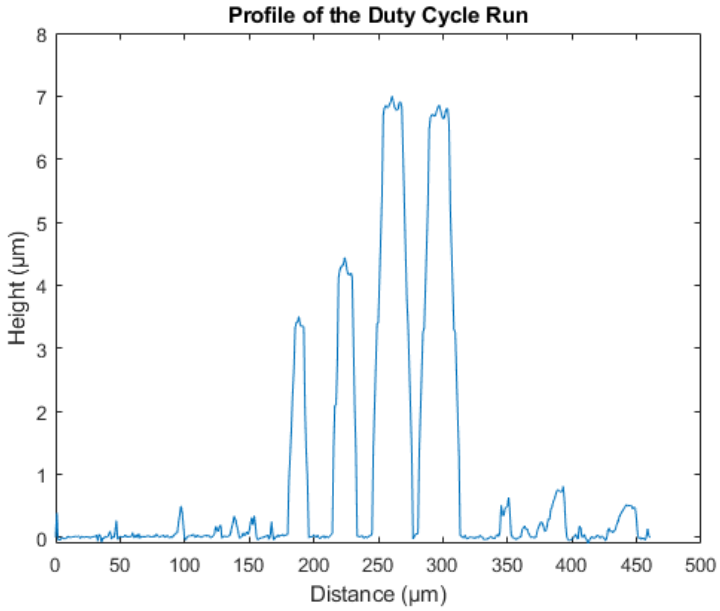

Figure 2.20: Shows the height profile data of a cross section from Figure 2.15, showing the height of each structure cured. The structures match the previous image, where the 5 % duty cycle structure is on the left, going to the 100 % duty cycle structure on the right.

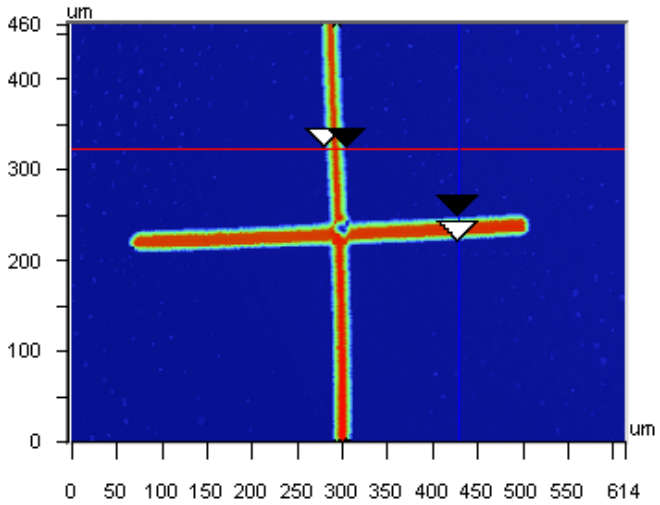

Figure 2.21: Indicates where the measurements took place on the strucutres cured in Figure 2.12.

2.4.5 Smaller Structures

In this section, efforts towards reducing the size of the cured structures are presented. From Figure 2.15, it is known that having a lower dosage will result in the structures being narrower, but this runs the risk of the structures not being fully cured. The optics in the system can also be changed, either via the size of the curing μ-LED or via the lenses used. An obvious choice might be to change the microscope objective lens (X10 in Figure 2.1), but this would result in having a smaller field of view. As one of the advantages of this setup was the larger field of view in comparison to previous work [15], this approach was not followed.

2.4.6 Lens change

The first option that was attempted was to change the lens in front of the curing μ-LED, to a lens that would result in a smaller projected μ-LED spot size. As only one μ-LED pixel is used for curing currently, this does not affect the field of view of curing, provided that the lens is large enough to capture the diverging light of the curing μ-LED. A Thorlabs C240TME lens was chosen as it has a 20 % shorter focal length while having the same 12 mm diameter of the lens previously used. This theoretically should decrease the size of any cured structures by 20 % as well by reducing the size of the projected μ-LED spot.

An issue with changing the lens to have increased optical power is that of multiple exposure. This is seen in Figure 2.22; one μ-LED was switched on, and one structure was made with a visible inner section of width 15 μm. However, there was also a wider surrounding section of width approximately 100μm. It is thought that the wider structure is from the μ-LED being reflected off the bottom of the slide, with both being of sufficient dosage to result in photocuring. However, when a smaller dosage was attempted by reducing the duty cycle, no change was seen in the structure width.

There are a few reasons as to why this might not have worked. The original assumption that the μ-LED power would not be affected by the change in lens might be wrong and that the measured power at the sample level might have changed, either from the change in lens or in the time since the original curing dosage was calculated.

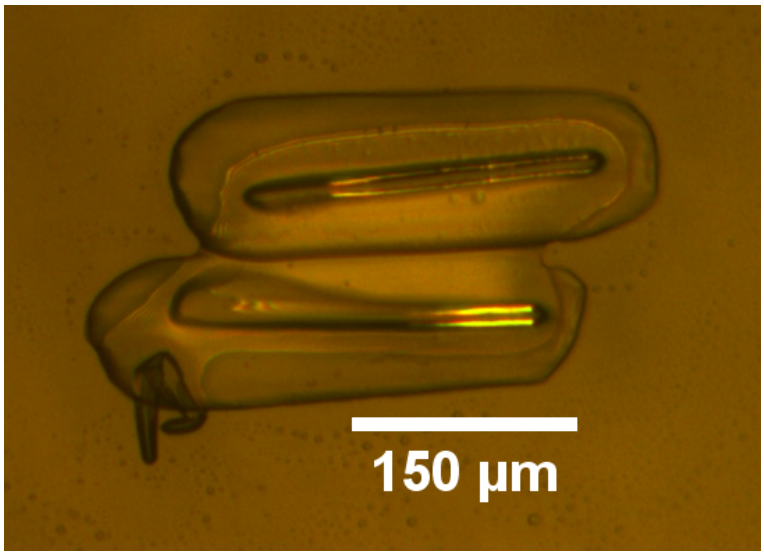

Figure 2.22: Shows a structure made with the shorter focal length lens in front of the curing μ-LED. While only one structure was cured, two separate sections of it are visible: an inner section of width 15 μm and a wider surrounding section of width approximately 100μm.

More rigorous testing would need to occur to check this assumption, which might result in changes in the duty cycle or the stage speed to get to the dosage level of 220 mJcm^{-2} seen previously.

2.4.7 CCD Camera Investigation

Figure 2.23 shows the same μ-LED output but with different integration time on the CCD camera: 5 ms and 30 ms, respectively. As the integration time increases, so too does the apparent spot size, from 5 μm to 12 μm as the camera picks up more light. This results from the camera having a non-linear response to light intensity from a gamma correction, a non-linear response curve applied to the received light from the CCD camera to make its output more comparable to human perception, being applied to the images, but was unable to be turned off. As a result, it is important to normalise the images, and look at the cross-section of the μ-LED spots at the two integration times. Figure 2.23 c) and d) are normalised versions of a) and b), respectively. The normalisation was done by taking an average of all three CCD channels for each pixel to create a greyscale image which was then divided by the peak value in part b). It can be

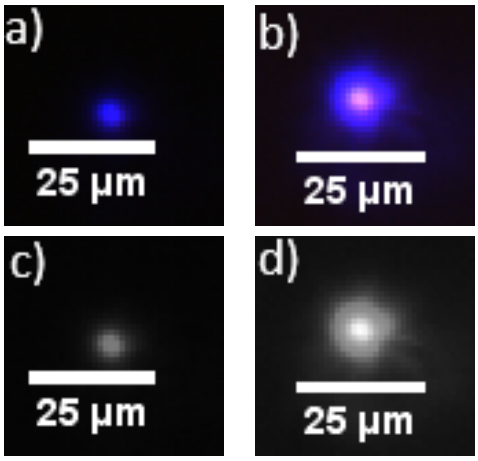

Figure 2.23: Shows the difference that changing the integration time has on the measured spot size. Both pictures show the same μ-LED, but for a), on an integration time of 5 ms has been used, whereas for b), an integration time of 30 ms has been used. c) and d) are normalised versions of a) and b), with the peak value of part b) used as a normalisation factor.

seen that when normalised, the centre of part d) becomes more pronounced, allowing a more direct comparison between it and part c), which look to be similar in size at 5 μm. However, the images were overly saturated and gamma corrected, the latter of which was unable to be changed. As a result, it is impossible to make comparisons between images, due to the gamma correction potentially changing between images. If it were possible to change the settings to remove the gamma curve, it would mean that the measured spot size of the LED would be easily determined.

However, this investigation has unanticipated consequences on the dosage calculation, given that the CCD camera was used in the earlier spot size estimation. If it is not possible to accurately measure the spot size of a given μ-LED using the camera, it is reasonable to ask how it can be used in the dosage calculation given earlier in this chapter. The answer lies in using the μ-LED centre to centre pitch instead of the size of an LED. Using the centre to centre pitch ensures that the nonlinear effects seen on the camera can be discarded, as the central position of the LED should not change with the CCD camera settings, until the point where two adjacent LEDs are indsitinguishable from each other.

To help prove this, an intensity profile through the spots at both integration times

is required, as is shown in Figure 2.24. This graphs the normalised CCD response as a function of pixel position in the image. The Full Width Half Maximum (FWHM) can be used as a measure of the spot size, and from 5 ms to 30 ms, it increases from 10 to 20 pixels across. This corresponds to a width of 18 and 36 μm, respectively. However, the positions that were used to measure the FWHM for the 5 ms image correspond to a similar jump in the 30 ms integration time image as well. This could be proof that the 5ms image represents the correct spot size of the LED as being 18 μm.

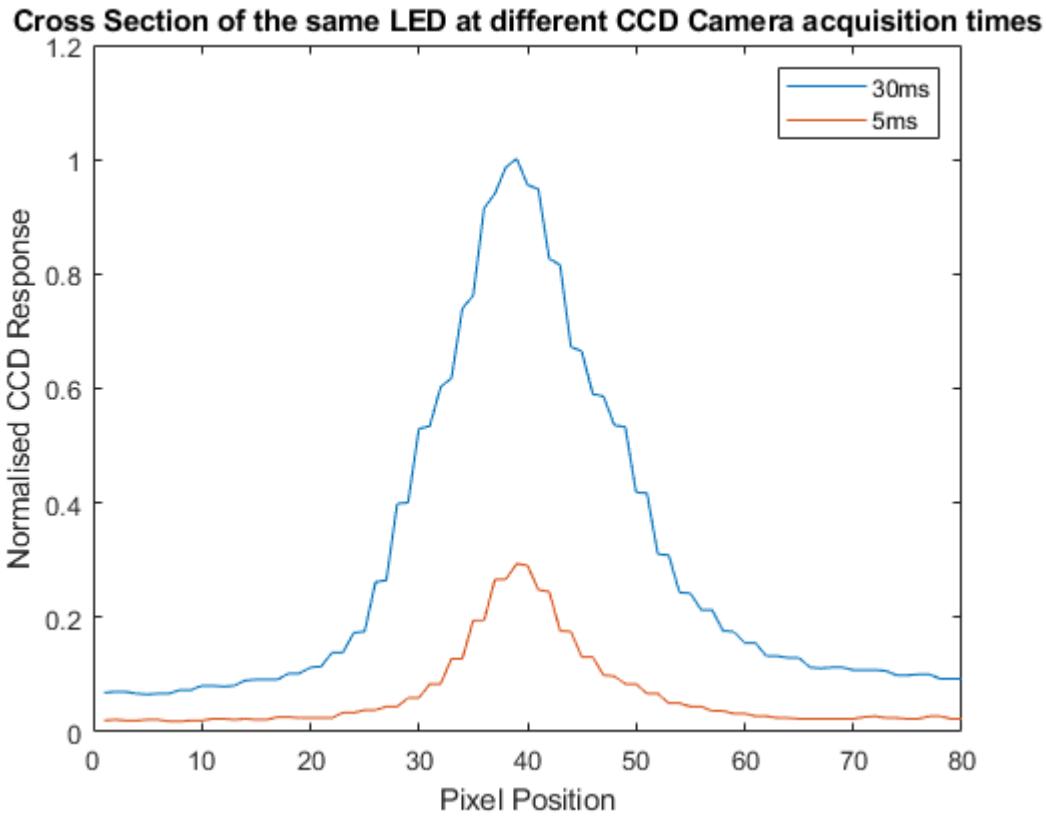

Figure 2.24: Showing the cross section of the normalised images in Figure 2.23.

2.4.8 Smaller μ-LEDs

Another way to have smaller sized structures is to reduce the size of the projected μ-LED. By replacing the μ-LED with a smaller one and keeping the rest of the optics the same, theoretically there would be a smaller projected spot. An array with differently

sized μ-LEDs, centred around 405 nm, was made in house at the Institute of Photonics. These ranged from 75 μm, roughly the same size as the ones used earlier, down to 8 μm. It was decided to use a μ-LED that was 10 μm wide with a measured power of 240 nW.

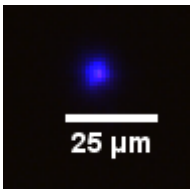

Figure 2.25: Shows the 10 μm μ-LED used in the attempt of curing.

A picture of the projected 10 μm μ-LED spot is shown in Figure 2.25, and is estimated to be approximately 4 μm wide at the sample plane. This device was chosen due to its reasonable power at a significantly smaller mesa size. An example of the projected spot used, alongside its immediate neighbour which was 6 μm across, is shown in Figure 2.26. The latter has an estimated spot size of 2 μm. Figure 2.26 was normalised to the same value as in Figure 2.23.

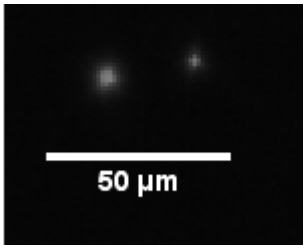

Figure 2.26: Images of projected spots of adjacent μ-LEDs from the array of devices of different diameters. These are of 6 and 10 μm mesa diameter, normalised to the peak value in Figure 2.23 b.

As before, the intensity profile of the μ-LED spots was determined to help ascertain their size, and this can be seen in Figure 2.27. They show that the 10 μm LED had a FWHM of 10 pixels, or 18 μm, and the 6 μm LED had a FWHM of 6 pixels, or 11 μm.

Given that the two spots are visible and of different sizes, curing could now be attempted, with the idea that the smaller μ-LEDs would result in smaller projected spots. As only one μ-LED is on at any time during the curing process, this allows optimising the setup for the curing μ-LED. With this setup, the dosage was estimated at 56 mJcm^{-2}, lower than the dosage with the larger μ-LEDs.

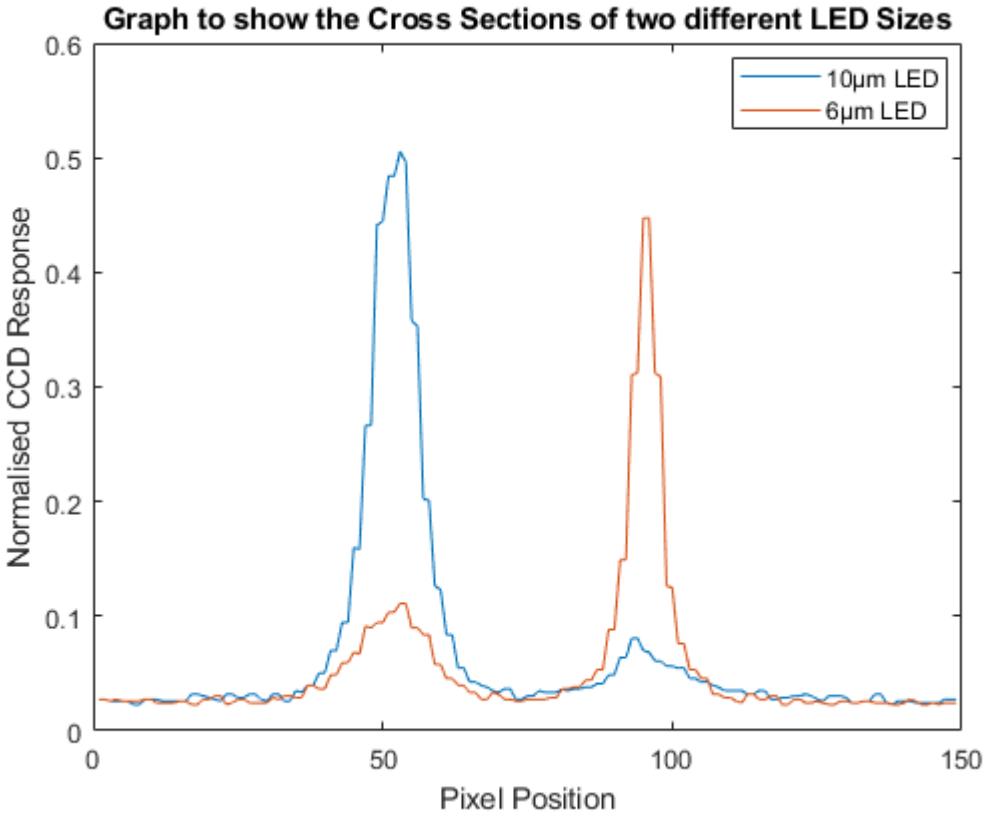

Figure 2.27: Shows the cross section through the centre of the μ-LED projected spots in Figure 2.26.

Because of the reduced dosage, it was decided to first increase the duty cycle of the μ-LED to 100 %, compared to the 6.2 % used previously. This seemed to result in no visible structures being cured, so it was decided to reduce the speed of the stage, halving the value used each time, starting at 2000 (the maximum value). This also did not result in visible structures, even at a stage speed of 10, close to stationary. A structure where the stage is stationary might be possible to cure something visible, but the point of this setup was that the stage would move to make structures with only one curing μ-LED.

Given that the stage speed, μ-LED power and spot size are the only variables in Equation 2.1, which were changed as much as possible to accommodate the μ-LED size, further steps in using this same setup for structures on the order of a micron are uncertain. Ultimately, these findings highlight that changing the μ-LED size alone may

not provide the desired improvement in resolution and resist type and optics choice are important factors.

2.5 Summary

In this chapter, a working visible light direct writing system using μ-LEDs was discussed, which uses structured illumination for fluorescent markers for positioning. The system was explained with reasons given for the main design choices made. The sample preparation techniques were also shown, and the fluorescent markers and photo-resist used were introduced.

The automated positioning algorithm was explained, from design choices made during the algorithm construction to the showing results in the positioning, where two different rounds of alignment were required for successful positioning. Photolithography using the setup was then discussed, and the structures used were shown in detail, with the setup shown to be capable of curing both straight lines and smooth curves. The curing itself was then optimised, with the dosage and width of the structures reliant on the duty cycle of the curing μ-LED; the latter signifying that there was some expansion of the projected μ-LED spot. Having a higher frame rate increased the smoothness of the cured structures and so was kept as high as possible for further work. The post-curing cleaning techniques were then outlined, with careful consideration given to the potential frailty of the cured structures and the capability of the cleaning to uplift the cured structures.

The dosage of the photolithography system was estimated at 220 mJcm^{-2}, as determined by measuring the power and projected spot size of the curing μ-LED, along with the speed of the XYZ stage. An ESEM image and optical profiler data were taken on some of the structures taken to verify the structure sizes and height of the cured structures. Smaller structures down to 10 μm wide were desired and curing was attempted. Two methods were explored: having a collation lens with a shorter focal length of the curing μ-LED, and using a smaller μ-LED for curing.

Chapter 3

Deep Ultraviolet Direct Writing

Deep UltraViolet (DUV) is a region of the electromagnetic spectrum corresponding to the wavelength range 200-280 nm [100]. Research utilising this region of the spectrum is fast moving, especially in LEDs where emitters at this wavelength are starting to be applied in areas such as disinfection [100] and communications [101], [102]. There are already commercially available photo-resists that utilise DUV light, focussing on 248 nm, which is the wavelength of KrF excimer lasers, so adding DUV μ-LEDs to photolithography is a natural and timely application of this emerging technology. At the time of this work being undertaken, DUV photolithography had yet to be reported with μ-LEDs, thus this thesis reports what were to our knowledge at the time, the first structures cured with a DUV μ-LED. Since then, [103] has reported direct writing using a DUV μ-LED array, albeit without CMOS control.

An advantage of using shorter wavelength light is that it can allow for smaller feature sizes compared to visible micro-photolithography such as is described in Chapter 2; from the Rayleigh Criterion, the smallest resolvable spot is dependent on the illumination wavelength [104], as shown in Equation 1.1. However, this requires the curing wavelength to be the limiting factor in improving resolution, which is but one factor. Another advantage of using DUV μ-LEDs in our system is that they offer larger spectral separation between the curing and positioning μ-LEDs, allowing other wavelengths of positioning μ-LEDs to be used. Using a different wavelength of curing μ-LED also allows other photo-resists to be used.

In this Chapter, the setup that was used will be explained, along with the optical and electrical characterisation of the DUV μ-LEDs. A size-dependent array was used to study the effects of the μ-LED mesa size on its electrical and optical characteristics. Photo-curing at 275 nm was explored and the photolithography system itself was characterised by looking at the spot size of each of the μ-LEDs used and the subsequent DUV dosage at the sample level. Finally, the cured photolithography structures that were made with the setup are shown, their profiles and the effects on the structures of applying Pulse Width Modulation (PWM) to the μ-LEDs will also be explored.

3.1 DUV setup

Figure 3.1 a) shows the block diagram of the photolithography system used for DUV photolithography, and a photograph of the setup is shown in Figure 3.1 b). In Figure 3.1 b), the camera is not in the system, but its position has still been noted. As a proof of concept of DUV μ-LED based photolithography, no positioning was done using this system, in contrast to what was described in Chapters 2 and 4. As the general layout had already been shown to work, no systematic changes were required for the setup from the previously working system as described in Chapter 2. While the block diagram setup is similar to that of the previous chapter, the parts were changed to allow for DUV transmission. The parts that were used in this system were as follows:

- L1 - 1" UV Fused Silica Plano-Convex Lens, focal length 250 mm, Thorlabs 4158
- L2 - 1" UV Fused Silica Plano-Convex Lens, focal length 50.2 mm, Thorlabs LA4148
- L3 - 1/2" UV Fused Silica Aspheric Lens, Edmund Optics 87-976
- M - 2" UV-Enhanced Aluminium Mirror, Thorlabs PF20-03-F01
- OL - $\times$10 MicroSpot UV Focusing Objective, LMU-10X-UVB
- PSU - Yokogawa GS610 Source Measure Unit

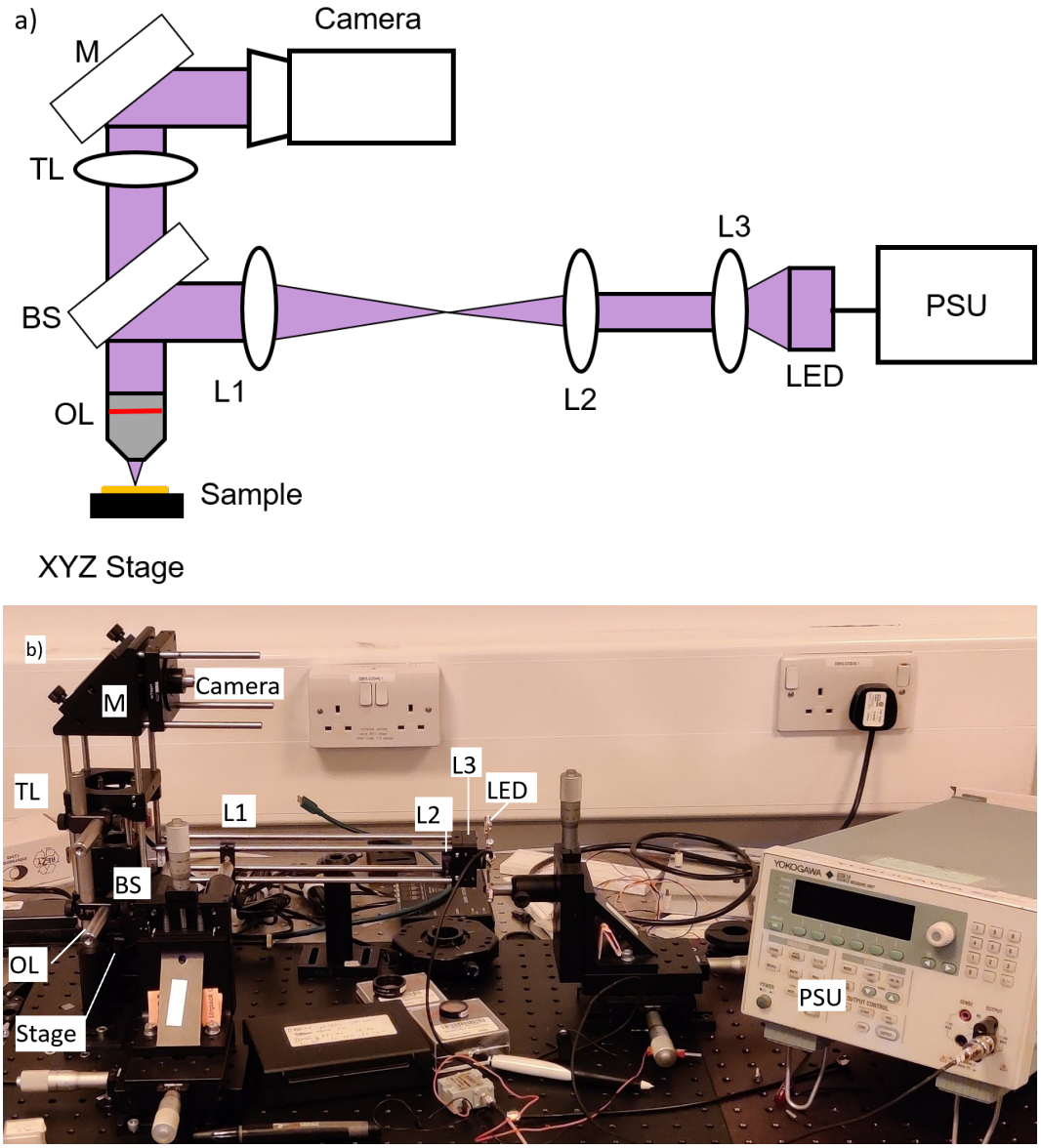

Figure 3.1: Diagram and photograph of the setup used in DUV direct writing. The camera is not in the photograph, but its placement in the setup has still been noted. PSU is the Power Supply Unit.

The same borosilicate glass samples and XYZ stage were used as in Chapter 2. The PSU was instrumental as voltage and current limits could be applied, protecting the μ-LEDs in the event of electrical failure or a faulty connection. The PSU can also simultaneously measure both current and voltage to monitor normal operation of the μ-LEDs. These measures helped extend the μ-LED operating lifetime.

The DUV μ-LEDs that were used were custom fabricated in the Institute of Photonics [105]. They were fabricated on AlGaN-based wafers in a flip-chip configuration, as described in Section 1.4.2. Standard UV lithography and inductively coupled plasma etching processes defined the circular pixels, which then had layers of various materials deposited upon them in an epi-structure as shown in Figure 3.2.

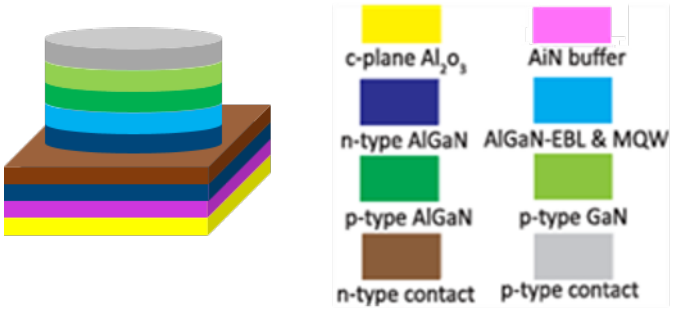

Figure 3.2: Epitaxial structure of the DUV μ-LED arrays used in this work.

A micrograph of a sample array is shown in Figure 3.3; the μ-LEDs in the array have the following diameter mesas: 500, 300, 200, 100, 80, 60, 40 and 20 μm, respectively. Figure 3.3 has two arrays, but only one was used in the experiments, being the one that was wire bonded for contacting. The 200, 80, 60 and 40 μm μ-LEDs from the array were used, as the other μ-LEDs were either inoperable or unsuitable for photo-curing, either because their light output was not constant in time, or did not have an electrical connection wired to it. This system lacks the CMOS control of the μ-LED arrays used in Chapter 2 due to the high drive voltages that DUV μ-LEDs currently require (see below). The duty cycle is therefore controlled by the PSU. Recent developments after the system in Figure 3.1 was made have allowed CMOS to drive DUV μ-LEDs in an array format [106], by optimising the contacting and reducing the ground voltage. Future iterations of the work presented here should therefore be able to utilise CMOS functionality.

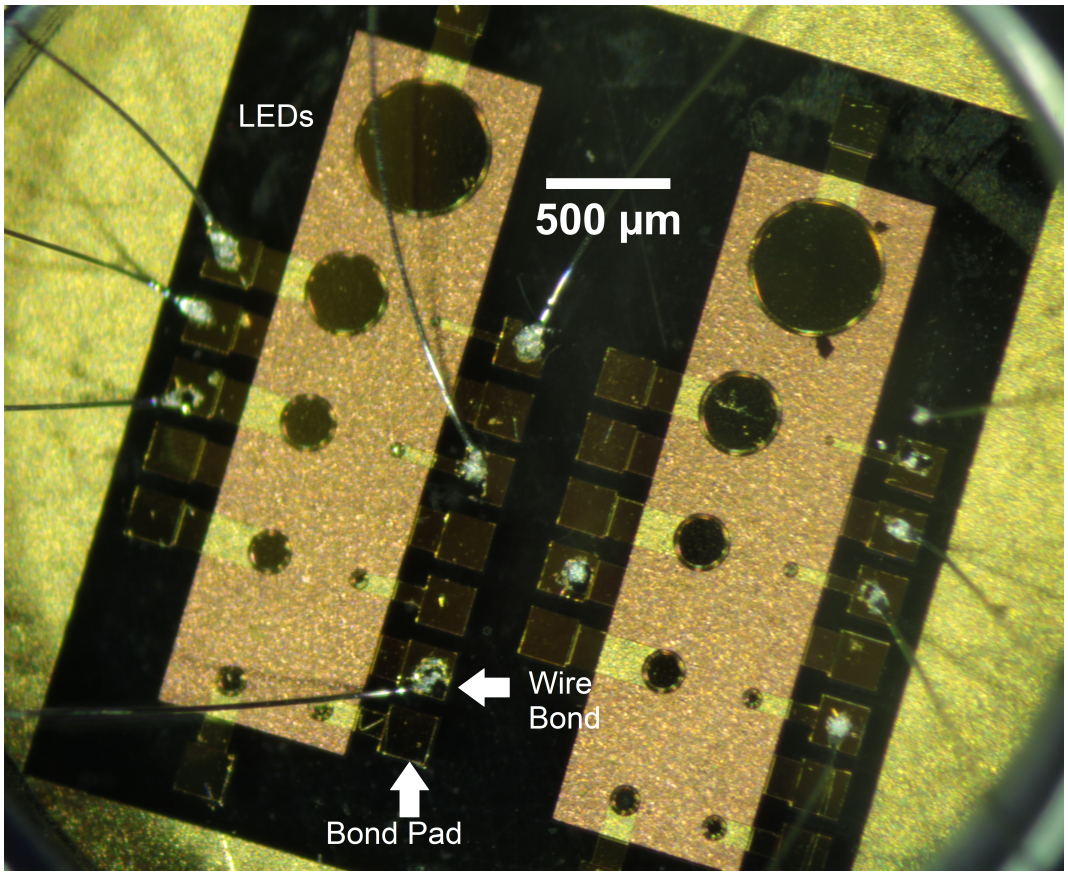

Figure 3.3: Micrograph of DUV μ-LED arrays used in this work.

3.2 Device characterisation

Before the μ-LEDs are used within the system, they need to be characterised. The characterisations required for photolithography purposes were the IV and LI curves of each μ-LED used, along with the emission spectrum of each μ-LED. The LI and IV curves are required to know the correct settings to safely get as much power as possible out of the μ-LEDs. Emission spectra are required to be taken during system design and assembly to ensure that the photo-resist will be absorb the μ-LED light and cure properly. For more information on characterising LEDs, see Section 1.5.

3.2.1 IV curves

The IV curve was taken for each μ-LED by increasing the voltage up in pre-determined steps and recording the current measured by the PSU. The forward voltage at 1 mA was measured by the PSU; this forward measurement result will here on be referred to as the 'turn on' voltage.

Figure 3.4 shows the IV curves for each of the μ-LEDs used in this system, plus others on the chip. In this Chapter, as opposed to Section 1.5.1 where the idea was introduced, the turn on voltage for the DUV μ-LEDs is defined as the voltage at which at least 1 mA of current is recorded on the PSU. Table 3.1 summarises these data by showing the size dependence of the turn on voltage of the devices. As the μ-LED mesa gets bigger, the switch on voltage decreases; this happens because there is less parasitic leakage current as the mesa gets larger [107].

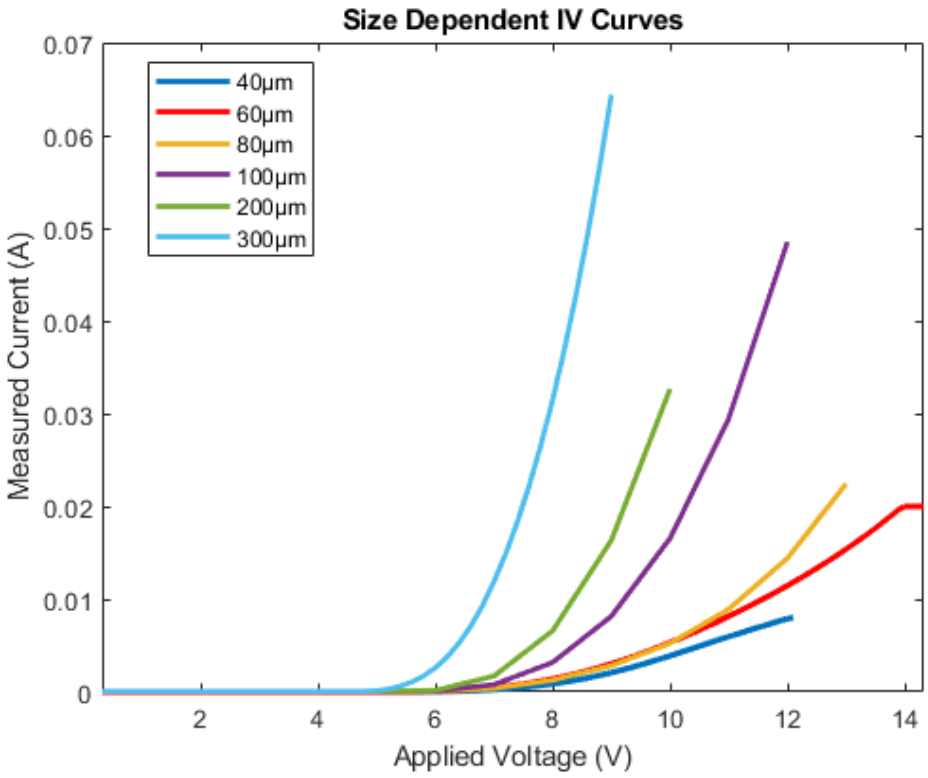

Figure 3.4: Graphs showing the IV curves of the LEDs used in this chapter.

LED Mesa size (μm)	Turn on voltage (V)
40	9.6
60	7.4
80	7.0
80	6.8
100	6.1
200	5.9
300	5.0

Table 3.1: Summarising the turn on voltage of the DUV μ-LEDs used in this work.

3.2.2 LI curves

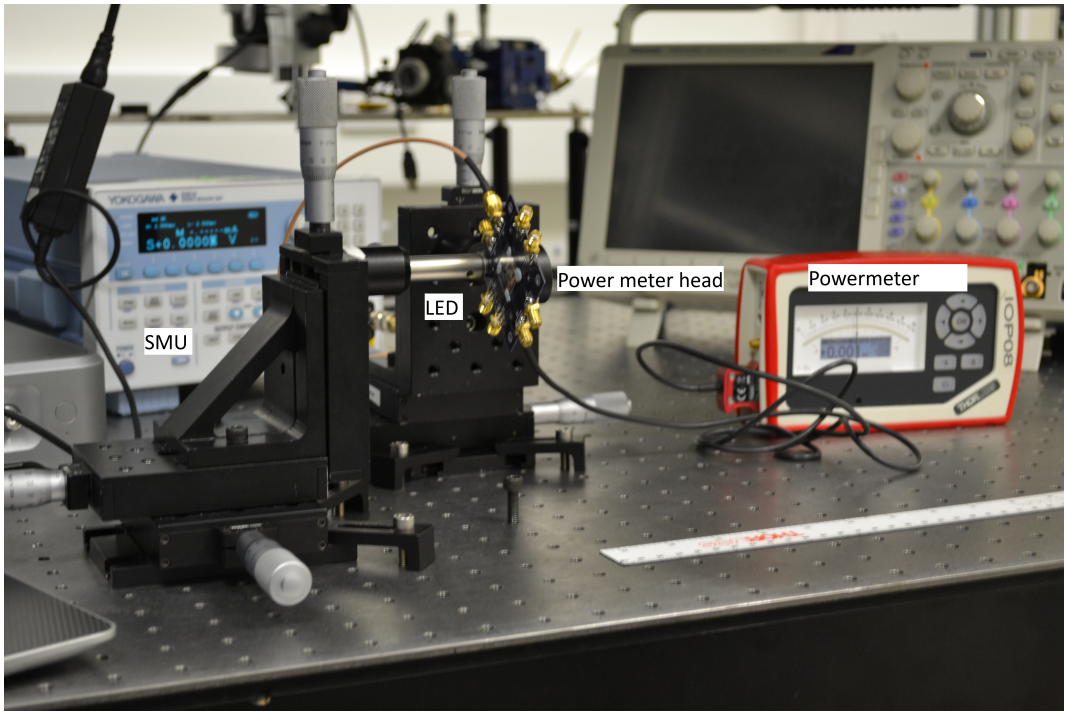

Figure 3.5: Photograph of the setup used for measuring the LI Curves.

The LI curve was taken in a similar manner to the IV curve, by stepping the current and recording the output on an optical power meter; the setup is shown in Figure 3.5. The PSU can be seen on the left of the image, and the μ-LED array and the optical power meter head seen in the middle of the image, with the optical power meter itself shown on the right of the image. The μ-LED board is immediately in front of the optical

power meter head; this was done to get as much power as possible emitting from the front of the μ-LED array, to follow the Lambertian emission profile of μ-LEDs. This also gets a realistic idea of the front emitting power as used during photolithography, compared to an integrating sphere measurement which would measure all of the μ-LED output, as in [108].

Figure 3.6 a) shows the LI curves for each of the μ-LEDs used in the system, with an inset (Figure 3.6 b)) to better show the region below 30 mA. The current that the μ-LED was run at during photolithography is noted in Table 3.2. As the μ-LED mesa size increases, so too does the current applied and output power. As we see in Figure 3.6, each curve has a linear section, which then climbs to a peak light output before decreasing due to thermal effects; see section 1.5.1 for more information.

LED Mesa size (μm)	Current (mA)
40	10
60	17
80	30
80	35
200	75
300	100

Table 3.2: Summarising the size dependence of the operating current used for photolithography.

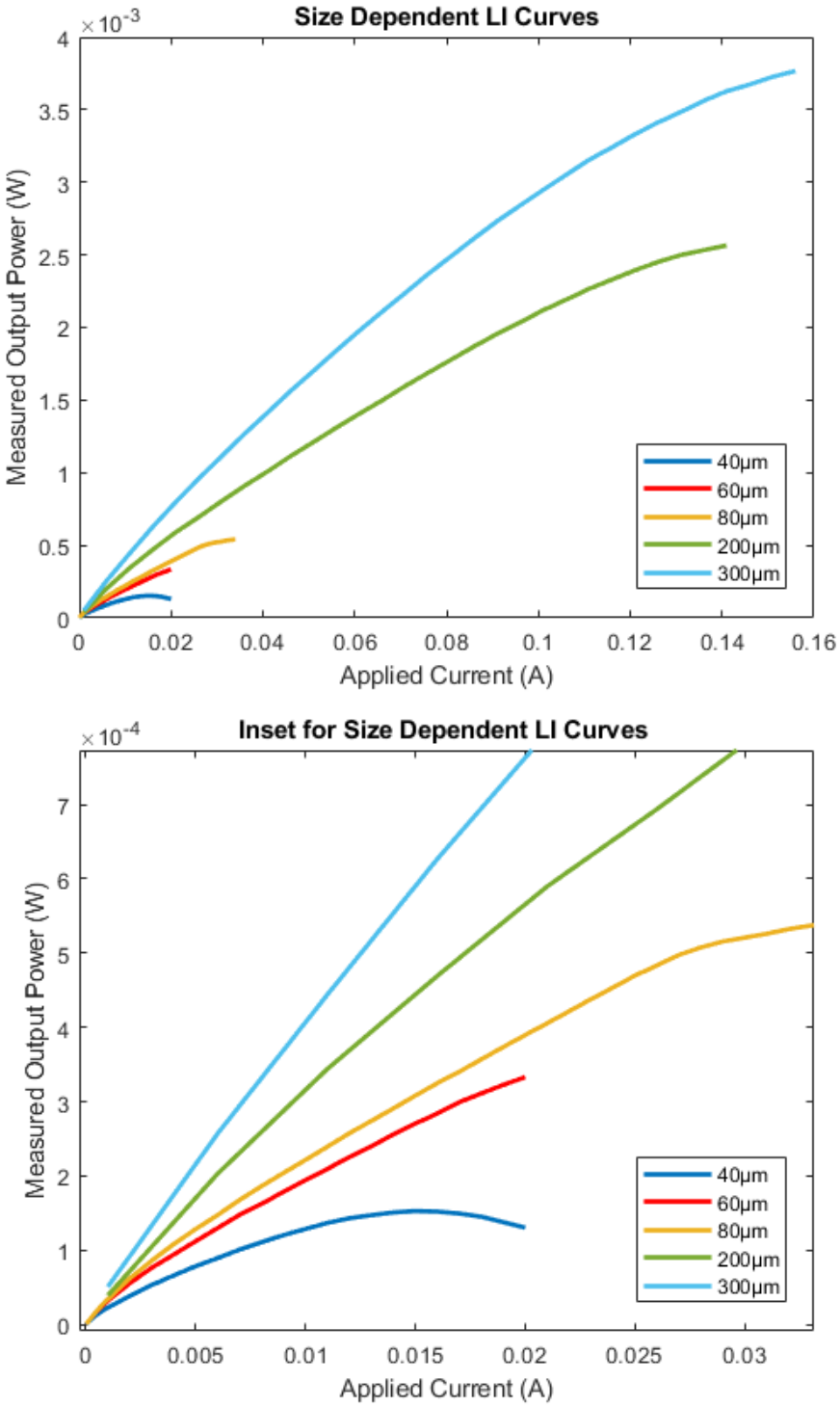

Figure 3.6: Graphs showing the LI curves of the LEDs used in this chapter (a) and showcasing the region below 30 mA (b) of the setup used in DUV direct writing.

3.2.3 Emission spectra

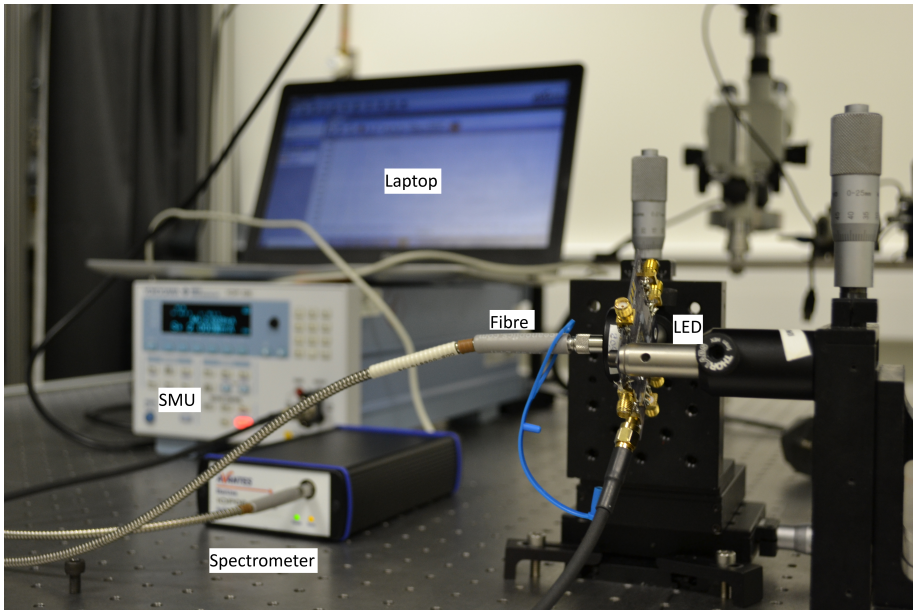

Figure 3.7: Photograph of the setup used in taking the emission spectra of the DUV LEDs.

The emission spectra were taken by operating each μ-LED at a current level near the top of the linear section of the LI curves previously taken. For this, an Ocean Optics QP600-2-SR-BX fibre with diameter 600μm connected to an Avantes spectrometer with spectral resolution of 0.3 nm was placed immediately in front of the μ-LED array, as shown in Figure 3.7. The spectrometer is designed to cover DUV, having a spectral range from 200-1100 nm. On the left of the Figure are the μ-LED array and the fibre for the spectrometer, with the spectrometer itself in the middle of the image. Behind it are the PSU and the laptop used to record the spectra.

Figure 3.8 shows a representative emission spectrum for the DUV μ-LEDs used in this work. Little difference was observed in the emission spectrum as the μ-LED mesa size and drive changes, so the spectrum shown in Figure 3.8 is representative of the μ-LEDs used. The emission spectrum peaks at 275 nm with a full width half maximum of 11.0 nm.

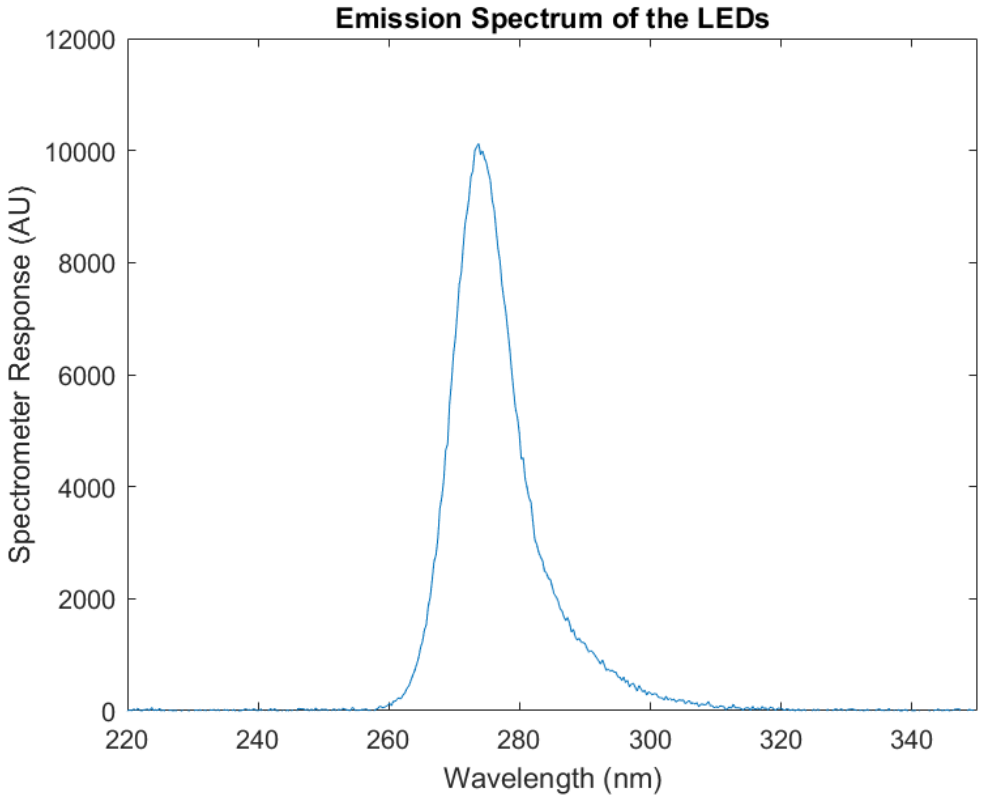

Figure 3.8: Representative emission spectrum of the DUV μ-LEDs used in this work.

3.3 Photocuring at 275 nm

Photo-curing using the DUV μ-LEDs used the same steps as outlined in Chapter 2, namely to prepare the sample and apply the photo-resist with a spin coater before curing with the μ-LEDs. As no positioning is undertaken here, fluorescent markers are not added; the photo-resist is simply spun on to the cleaned borosilicate glass substrate. After curing, the uncured photo resist is washed off with a developer and the sample is cleaned again before viewing.

3.3.1 Photo-resists

Alongside the Anycubic resin that was introduced in Chapter 2, a Norland Optical adhesive (NOA-81) was also used here as a negative photo-resist. This was to show that the system worked with multiple photo-resists, and it allowed exploration of a range of photolithography conditions.

Figure 3.9 shows the transmission spectrum for the Norland optical adhesive. It is described as being sensitive down to 320 nm, but was not originally designed for use at 275 nm. However, it does have some absorption at this wavelength.

3.3.2 Sample preparation

The process for preparing the samples was similar to that described in Chapter 2; however, there were some changes as described below. After cleaning the borosilicate glass slide, two drops of HMDS (HexaMethylDiSilazane) were placed on the glass slide to act as an adhesion promoter which was then spun on a spin-coater at 3200 rpm for 40 seconds. The photo-resist was then drop cast on the sample; for a 15×15 mm^2 slide, 6 drops evenly spaced around the sample were sufficient. The Anycubic resin was spun at 3200 rpm for 20 seconds, and the Norland optical adhesive was spun at 8000 rpm for 40 seconds. Care was required to ensure that the glass slide stays on the chuck of the spin coater; the spin speed was slowly ramped up over 30 seconds to 8000 rpm.

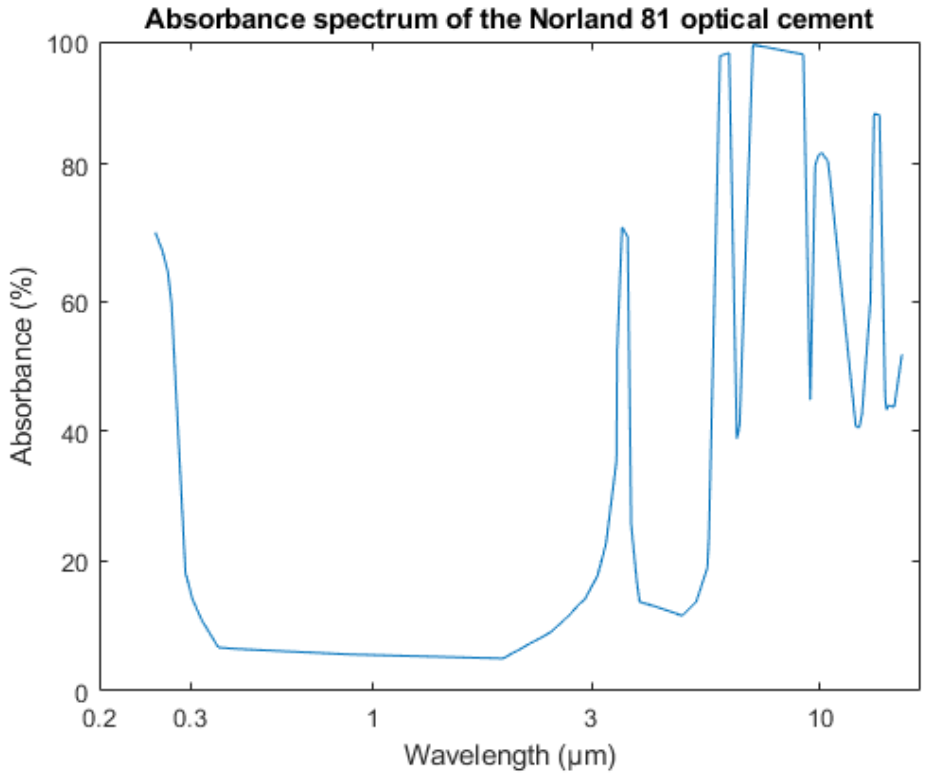

Figure 3.9: Transmission spectrum for the Norland optical adhesive used as a photo-resist [109].

The HMDS was used because smaller μ-LEDs result in smaller projected spots on the sample and therefore smaller structures being made. These smaller structures may not be structurally sound, especially when the photo-resist is under-cured. Therefore, the increased adhesion allowed for the smaller structures to stay on the sample during development after curing. This was used with both the Anycubic resin and the Norland optical adhesive. With conventional photo-resists designed for spin coating, the HMDS may not be required.

With the photo-resist applied, the sample was then cured using the μ-LEDs. During photo-curing, the XYZ translation stage operated at the maximal speed of 1 mms^{-1}. After exposure, the samples were developed using toluene to remove any unexposed photo-resist via gentle agitation for 30 seconds. The sample was left to air dry on tweezers. Further cleaning by use of the triple rinse method detailed in Chapter 2 is possible, but ran the risk of removing the small cured structures.

3.4 Dosage calculations

As in Chapter 2, the curing dosage of the DUV μ-LED based system needs to be calculated. This is to ensure the correct dosage is available during curing (the 2 Jcm^{-2} that the Norland requires) and allows examination of the experimental settings. It is important to note that a surface area, not volume, is mentioned here. The spin coating method results in an optical adhesive film a few microns thick, which would require a smaller dosage than a thicker layer of photo-resist. As per Chapter 1, the dosage at the centre of the structure is given by [15]:

$$E = \frac{2P}{\pi R v} \tag{3.1}$$

where E is the dosage energy, P is the μ-LED power, R is the spot radius, v is the velocity of the sample. In order to take these measurements, three things need to be known: the stage speed, the projected spot size and the power of each μ-LED at the sample level. The stage speed has been previously measured at 1 mms^{-1} [18], and the rest of this section will detail how the other measurements were made and their results, noting how the different μ-LED mesa sizes affect the characteristics measured.

3.4.1 Spot size measurements

The measurement of the projected spot size can be done in a few ways. The focussed spot itself can be imaged with a camera, requiring a calibration at the sample level with an object of a known size. Comparing the size of the focussed spot and that object allows estimation of the spot size. Another method is to move the sample over a sharp change in reflectivity or transmission, known as a knife edge measurement [110], [111]. Moving the sample a known distance over the knife edge and recording the change in detected light intensity allows estimation of the spot size. Both methods will be explored in this subsection.

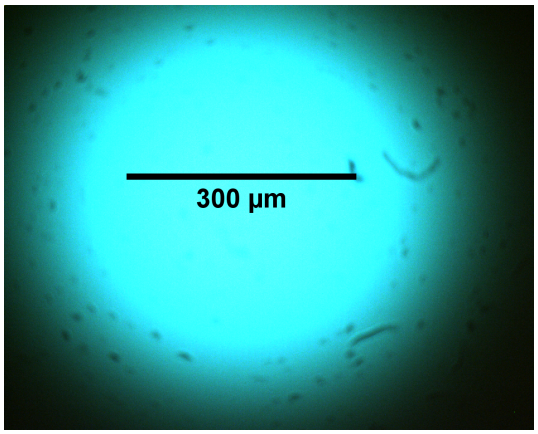

Figure 3.10: Apparent spot size of the 200 μm DUVμ-LED as shown with the BBEHP-PPV polymer. This spot size is approximately 450 μm wide.

Direct spot size imaging

Taking a direct image of DUV μ-LED light is difficult due to its wavelength; detectors that can measure these wavelengths of light are often expensive, with the CCD camera used in Chapter 2 being unresponsive at this wavelength. It was therefore decided to take an image of the DUV light exciting a spot on a glass slide coated with a fluorescent, green-emitting polymer, BBEHP-PPV (poly(2,5-bis(2,5-bis(2-ethylhexyloxy)phenyl)-p-phenylenevinylene)). For more information on how the BBEHP-PPV was synthesised, please see [112]. The BBEHP-PPV was dissolved in chlorobenzene and spun at 4000 rpm for 45 s. The fluorescence showed a broad spectrum between 475-550 nm, thus it should be easily visible with the CCD camera.

The smallest spot imaged by the camera using the 200 μm μ-LED is shown in Figure 3.10. The Full Width Half Maximum of this spot is approximately 450 μm in diameter. Given that the projected μ-LED image is focussed by a 10X microscope objective, the excitation is over a wider area than what would be expected for the μ-LED. This could be due to the fact that the film acts as a waveguide for the fluorescence and scatters the light in the film, making the large spot shown in Figure 3.10. This makes the polymer approach look unsuitable for measuring the projected spot size.

Knife edge tests

To do the Knife Edge Test (KET), a glass slide was spray painted with matte black paint and left to air dry in a well ventilated area. After drying, it was placed at the sample position, with a white piece of paper placed under it, to act as the knife edge in reflectivity; the roughness of the edge made is the roughness of the edge of the piece of paper used.

During the KET, the stage was moved 1 μm at a time via the translation stage, with a spectrometer in place of the CCD camera used to detect the DUV light. The projected μ-LED spot is focussed on the white paper and is then moved over the knife edge into the black matte painted slide. By measuring the response at 415 nm while moving the stage, a plot can be made of the spectrometer response with distance. The distance measured between 90 % and 10 % of the maximal spectrometer response is classified as the measured spot size [111]. This does not measure the DUV spot size directly, but again relies on the fluorescence that occurs when the DUV light excites the paper.

Figure 3.11 shows the plots from the Knife Edge tests, with the response channel of 415 nm on the spectrometer. Both 80 μm μ-LEDs had the same KET data, so one plot covers both μ-LEDs. For each plot, the measured spot size is noted in the caption, with the size dependence of the μ-LED mesa size on the spot size tabulated in Table 3.3. It can be seen that as the mesa size increases, so too does the recorded spot size, with the smallest spot size recorded as 8.5 μm. It can be seen that the demagnification of the system is slightly different for the 200 μm μ-LED when compared to the rest: it had a demagnification factor of 6.4 compared to the rest of the μ-LEDs, which had demagnification factors between 4.5 and 4.7. This discrepancy in the demagnification factors can have numerous causes, but it is believed that it comes from the fact that not all of the 200 μm μ-LED was properly coupled into the system, thus cutting off part of the LED and making the spot seem smaller than it actually is.

Figure 3.11 showcases a variety of Signal to Noise Ratio (SNR) values for each of the μ-LEDs, and potentially would be the result of different spectrometer values used between μ-LEDs. For future work, it would be prudent to use a long enough detection

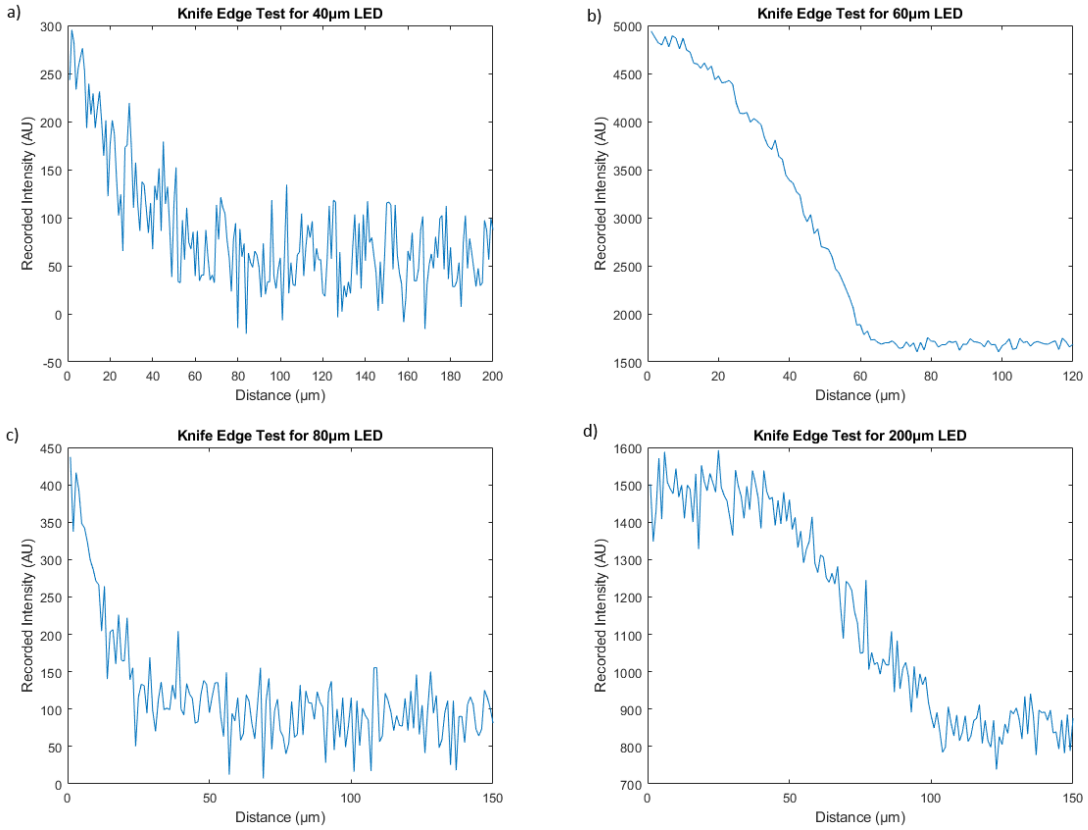

Figure 3.11: Knife edge test data of the μm-LEDs used. The spot sizes are estimated as 8.5, 13.4, 17.7, and 31.1 μm for the 40, 60, 80 and 200 μm μ-LEDs, for a), b), c) and d) respectively.

LED Mesa size (μm)	Measured μ-LED projected spot size (μm)
40	8.5 ± 4
60	13.4 ± 4
80	17.7 ± 4
200	31.1 ± 8

Table 3.3: Summary of the measured spot sizes of the DUV μ-LEDs.

window to allow for a large enough signal with the smallest, 40 μm, μ-LED and used those settings for each LED and take. However, the graphs shown in Figure 3.11 are just one of several takes that were used in the estimation of the spot sizes for each μ-LED. As each sub-figure of Figure 3.11 has the signature drop, the knife edge has moved sufficiently. However, for sub-figures a) and c), it would prove useful to move the knife edge further back after doing this particular test and retake these data so that the drop is more central in the plot, like in sub-figure d).

3.4.2 Power measurement

To measure the projected μ-LED power, as per Chapter 2, an optical power meter head (Thorlabs S120VC) is placed where the sample would be during photo-curing, set to 275 nm wavelength and zeroed. The μ-LED is then turned on, using the operating current mentioned in Section 3.2.2 for each μ-LED, and the maximal power is found by moving the power meter head in the xy plane. The results are tabulated below in Table 3.4 for each μ-LED used; as the μ-LED mesa increases in size, the output power increases, compared to Figure 3.6.

LED Mesa size (μm)	Measured μ-LED power (μW)	Power Density (W/cm^2)
40	0.86	0.38
60	1.59	0.28
80	2.60	0.26
80	7.50	0.76
200	26.7	0.88

Table 3.4: Summary of the measured power of the DUV μ-LEDs.

3.4.3 Dosage calculation

With the μ-LED power and the spot size estimated, the curing dosage for each μ-LED was then calculated using equation 3.1. The results are summarised in Table 3.5. Here, v in Equation 3.1 was 10^{-3} ms^{-1}, the fastest speed afforded by the stage. It was seen that as the μ-LED mesa size increases, so too does the dosage; the increase in power output by the μ-LED far outstrips the size increase. This was partially because the stage speed was kept the same between the different size μ-LEDs. To keep the illumination time the same between μ-LEDs, the stage speed would need to be increased along with the mesa size. However, the stage was already at its maximum speed and cannot be increased further. Therefore, the larger μ-LEDs had a longer illumination time on the photo-resist and therefore a larger dosage. Compared to other μ-LED based photo-lithography systems [113][4][92], this system afforded a higher dosage per μ-LED pixel. The dosages measured here are far higher than the 2 Jcm^{-2} that is recommended for the Norland optical adhesive, and details on the Anycubic resin used are not available.

LED Mesa size (μm)	Measured Spot size (μm)	Measured μ-LED power (μW)	Maximum Dosage (Jm^{-2})
40	8.5	0.86	91
60	13.4	1.59	106
80	17.7	2.60	132
80	17.7	7.50	381
200	31.1	26.70	755

Table 3.5: Summarising the dosage data for the DUV μ-LEDs used.

3.5 Direct writing structures

This section shows the structures that were made from direct writing in both the Anycubic and Norland photo-resist. Figure 3.12 was taken using the Anycubic UV resin introduced in Chapter 2; the rest of the figures in this section were taken with the NOA-81 due to it being more responsive when operated with a lower curing μ-LED duty cycle. Combined with the results from Chapter 2, it is believed that the Anycubic resin can only make structures 20 μm in width or wider. To begin with, the photo-resist

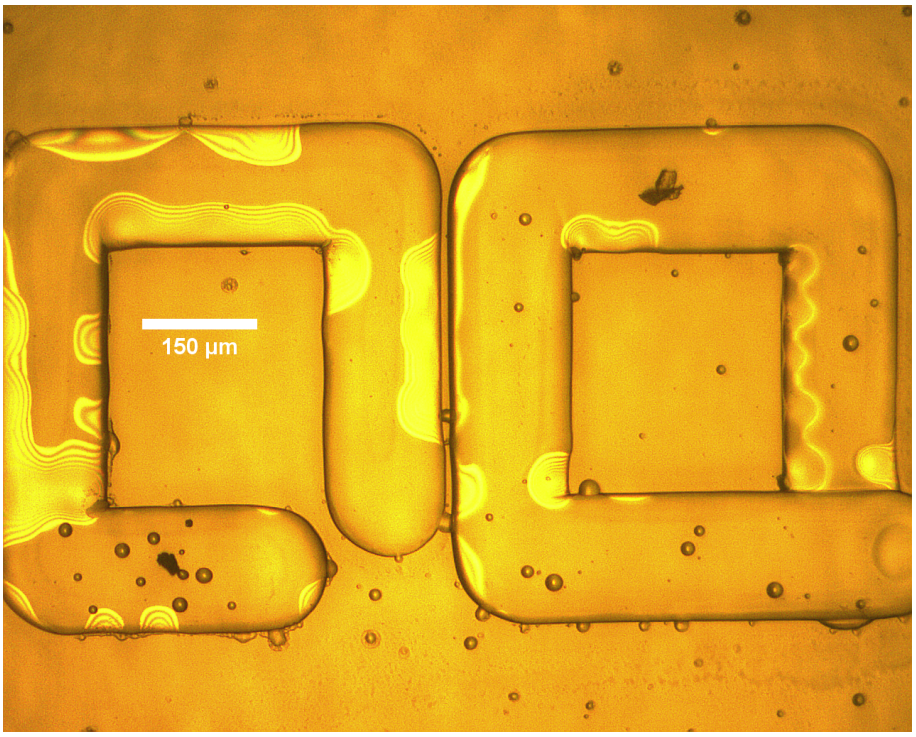

Figure 3.12: Anycubic structures made with the 200 μm-LED with 100 % duty cycle.

was cured with a curing μ-LED duty cycle of 100 %, the percentage of the time that the curing μ-LED is on for during the curing process, the results of which can be seen in Figure 3.12. These images were taken using the 200 μm μ-LED, which is much larger than the projected spot size of 31 μm measured, meaning that a duty cycle of 100 % over-cures the structures, resulting in the large structures shown in Figure 3.12.

3.5.1 Pulse width modulation

Given how much larger the structures made in Figure 3.12 were compared to what was expected, PWM was used with the μ-LEDs to reduce the duty cycle during curing. As explained in the Chapter 2, the duty cycle is directly proportional to the structure width; structure sizes on the order of 5 μm are the goal of the system.

Here, the PSU was set to 50 ms periods to allow duty cycles down to 0.2 % with 100 μs pulses, the shortest pulse time offered by the PSU. A blob of resist cured for a minute was used to orientate the sample when viewing and then duty cycles of 100, 50,

30, 20, 15, 10, 5, and 3 % respectively were used for all the μ-LEDs.

Micrographs showing structures made from NOA81 with duty cycled exposure are shown in Figure 3.13. In each of these images, the largest structure seen is the structure made from using a 100 % duty cycle, and from there, the duty cycle used is 50, 30, 20, 15, 10, 5, and 3 % respectively. For Figure 3.13 a), c), and d), this is from right to left, and for Figure 3.13 b), this sequence is from left to right.

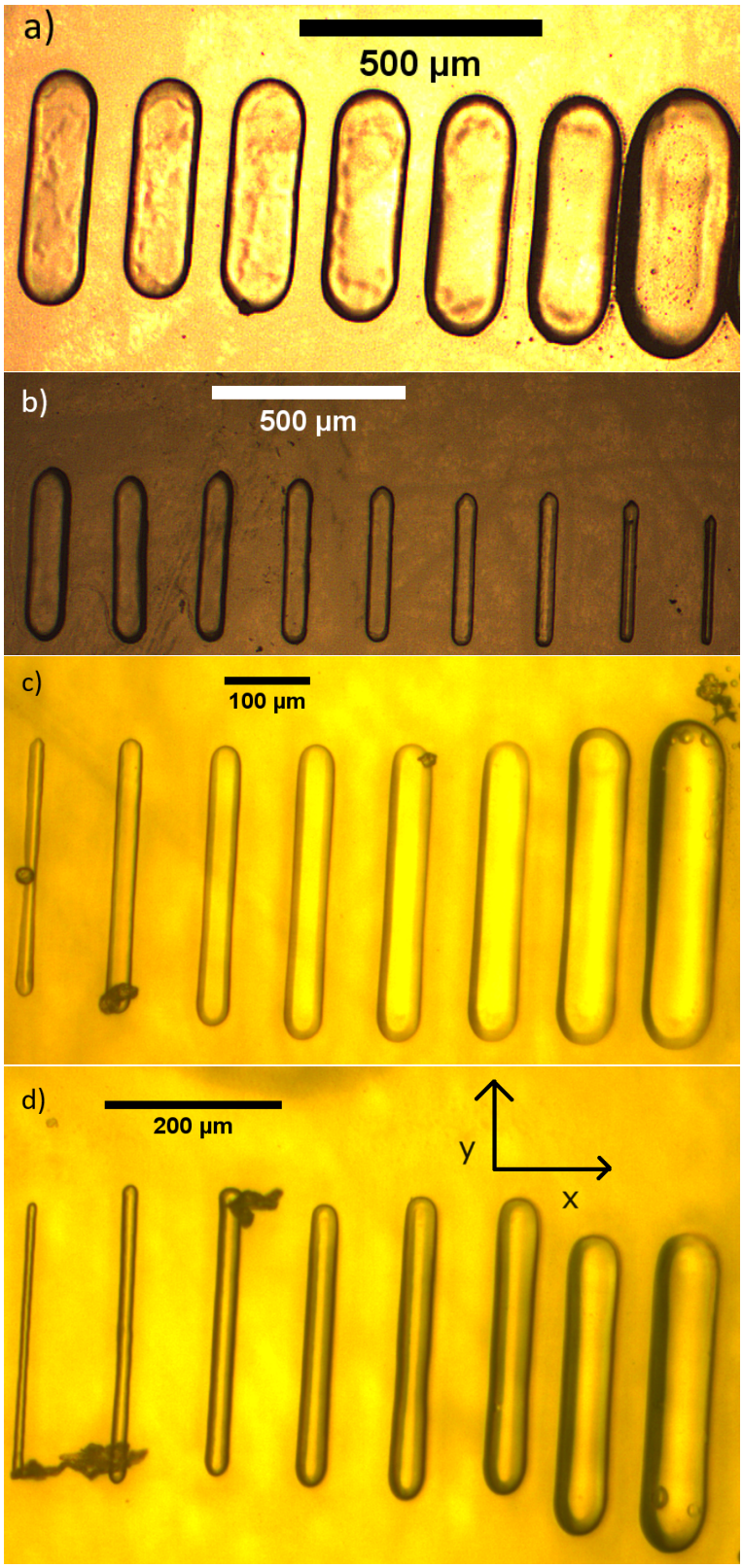

Figure 3.13: Duty cycle runs using the a) 200, b) 80, c) 60, and d) 40 μm DUV μ-LEDs, respectively, with the Norland optical adhesive 81. The x and y axes that are used throughout this section are indicated in the image using the 40 μm LED. The duty cycle used for these Figures are 100, 50, 30, 20, 15, 10, 5, and 3 %. In b), the 30 % duty cycle structure is cured twice.

Table 3.6 shows the width of all the structures made by each duty cycle value of the 40 μm μ-LED. As the duty cycle decreases, so too does the width of the cured structures; this is because areas outwith the smallest projected spot will not be cured with a high enough curing dosage, resulting in thinner structures. As the size of the μ-LED decreases, so too does the size of the projected μ-LED spot on the sample and therefore the resulting structures. The smaller projected spot sizes from Table 3.3 with a smaller μ-LED mesa size will also result in smaller cured structures. For these reasons, only the 40 μm μ-LED, with duty cycles of 2 and 1.6 % were used to achieve the smallest structures, to the point where structures stopped being fully cured, as shown in Figure 3.14. It appears to be the case that the 1.6 % duty cycle structure has peeled away slightly from the glass slide and has little uniformity, due to it being under-cured.

Duty cycle (%)	Measured structure width ($\pm$0.4μm)
100	26.1
50	17.8
30	17.8
20	15.6
15	13.6
10	11.1
6	7.8
3	5.8
2	5.7
1.6	2.8

Table 3.6: Summary of the change in Norland optical adhesive structure size via pulse width modulation of the 40 μm DUV μ-LED.

3.5.2 Resist structure profiles

An important characteristic, along with the width of the cured structures, is their profile, as introduced in Chapter 2. The structure profile displays the height and uniformity of the cured structure, and is here measured perpendicularly and parallel to the movement of the stage. When doing this, lines were cured to see easily how the uniformity is affected by whether or not the curing is perpendicular (from here on

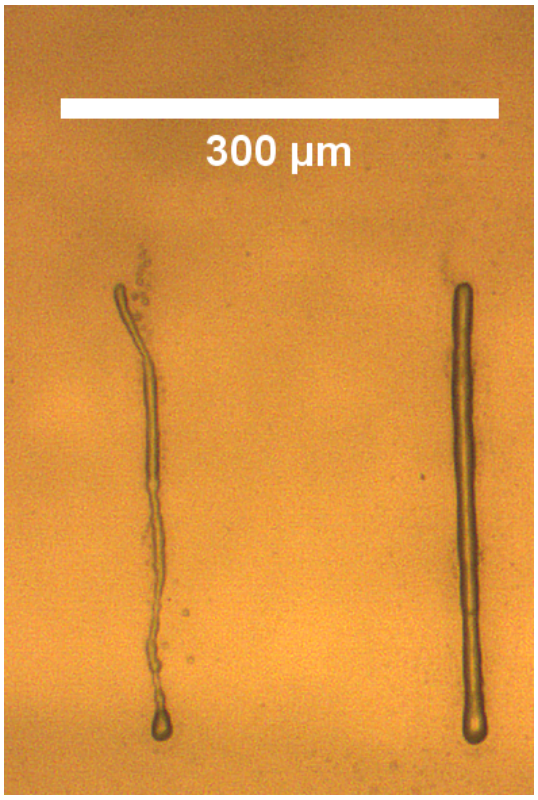

Figure 3.14: Micrograph of the smallest Norland optical adhesive structures made with the 40 μm DUV μ-LED, using duty cycles of 2 and 1.6 %, from right to left.

referred to as the x-axis) or parallel (referred to as the y-axis) to the stage movement. Figure 3.13 d), for example shows the axes as applied to the duty cycle run with the 40 μm μ-LED. Looking at the x-axis shows how uniform the curing μ-LED is, while looking at the y-axis tells us how uniform the stage speed is. If there is little uniformity in the x-axis, that can signify issues within the photolithography system; for example, that the μ-LED is misaligned. NOA-81 was used throughout this section as the photoresist. The profiles were taken using the same tool as in Chapter 2, a Veeco NT1100 optical profiler.

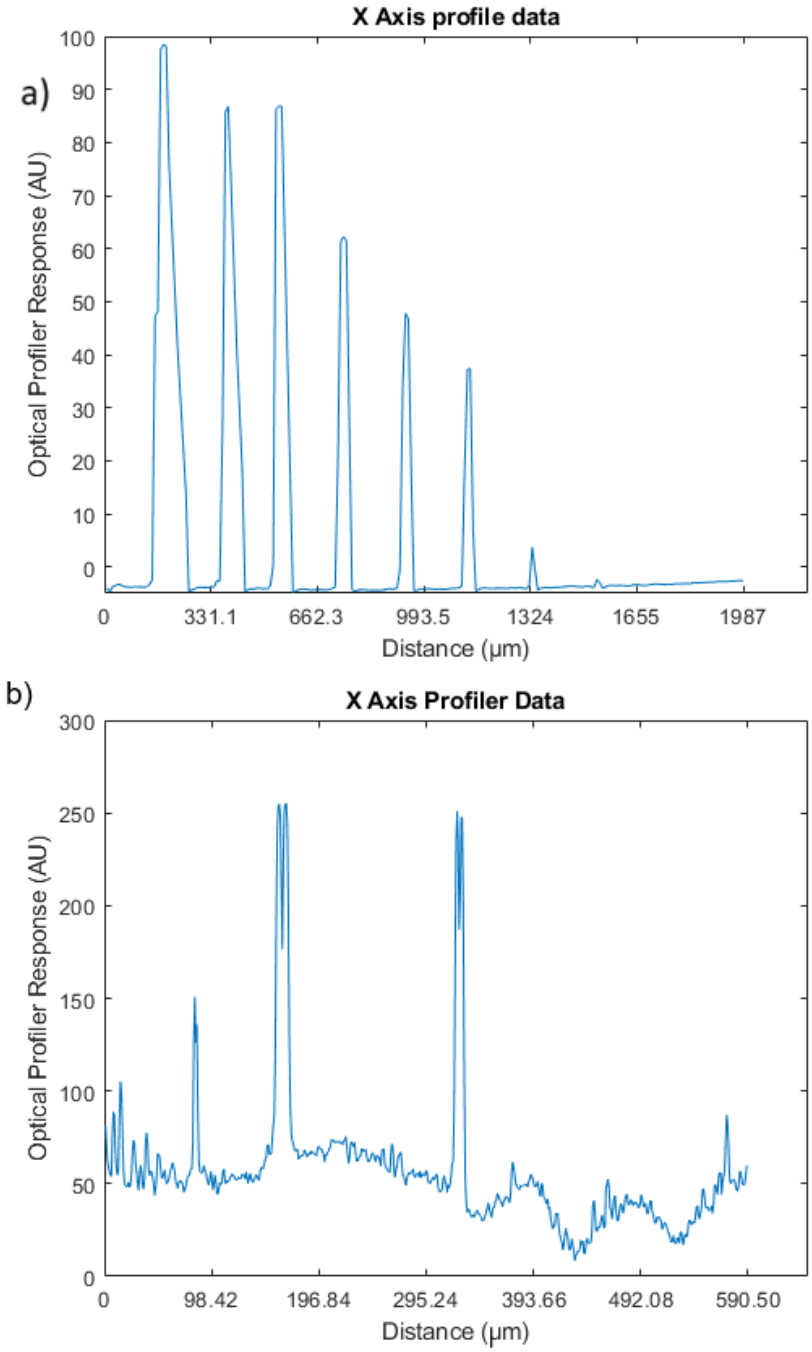

Figure 3.15: Profiles in the x-axis for some of the structures shown in this chapter. a) is for Figure 3.13 d), and b) is for Figure 3.14.

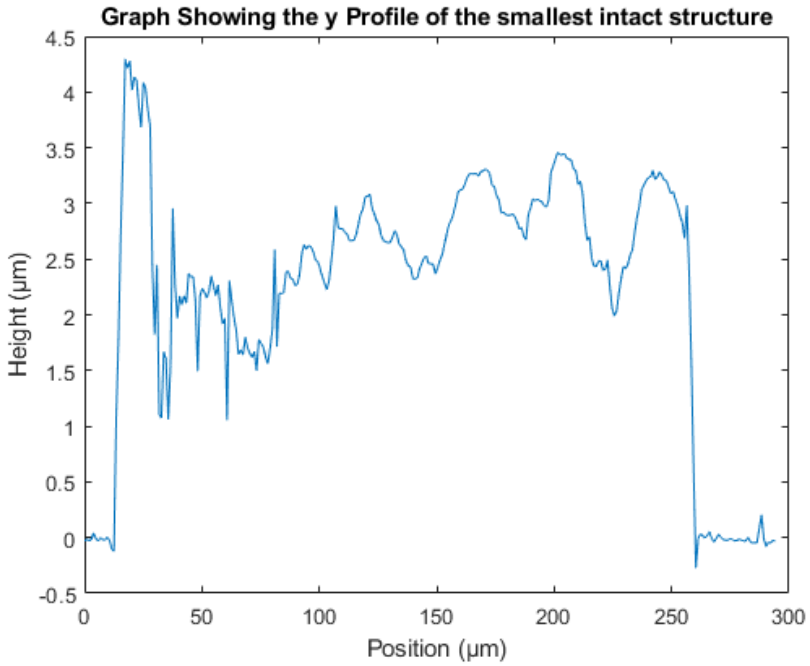

Figure 3.16: Height uniformity profile along the thicker stripe structure, on the right hand side of Figure 3.14.

Figures 3.15 and 3.16 show the profiles of the structures made by the 40 μm μ-LED. In Figure 3.15 a), the sample is upside down compared to Figure 3.13 d), hence the profile and picture being inverted. Figures 3.15 b) and 3.16 correspond to Figure 3.14, the smallest structures that were made.

All the x-axis profiles show a steep side wall edge, but this not related to the relative sharpness of the curing μ-LED projected spots. The side walls scatter light out of the side of the structures, instead of reflecting from the top. The optical profiler measures no light from the side scattered light and thus makes no measurement, giving the illusion of an incredibly sharp side wall.

In Figure 3.15 b), the double spike in profiler response at the centre of the structures has a few potential root causes: the μ-LED focus may not be perfect, or the μ-LED emission may be more powerful at the edges of the μ-LED compared to the centre. The relative non-uniformity in the background level of Figure 3.15 b) is potentially due to the profiler picking up smudges or droplets on the sample, rather than the cured

structures.

In Figure 3.16, the relative non-uniformity in the y-axis is likely to stem from the stage not moving at a steady speed during the curing process. The taller section at approximately 20 μm along is attributed to the μ-LED being on for a longer period at the end of curing, over-curing the optical adhesive. Again, the hard edges seen on this structure are because of the light being scattered away from the profiler, as with the x-axis profiles. Comparing the background level to the x-axis profile in Figure 3.15 b), the background level is relatively stable.

3.6 Conclusions

In this chapter, a deep ultraviolet direct writing photolithography system using μ-LEDs was discussed. The changes to the setup from the previous chapter were shown, including the DUV μ-LEDs used and the changes in optics. The DUV μ-LEDs were characterised, focussing on the LIV curves and emission spectra. The turn on current used during photolithography and measured power increased with μ-LED mesa size, while the turn on voltage decreased with increasing mesa size. The photolithography setup was characterised by undertaking a dosage calculation; this was done by measuring the μ-LED projected spot size and the curing power at the sample position. The changes in sample preparation from the visible violet μ-LEDs were explained, namely the addition of the HMDS to the cleaned borosilicate glass slide to aid in structure adhesion.

The results of the photolithography using the μ-LEDs themselves were then shown, focussing on shapes of squares and lines. The Anycubic photo-resist used in Chapter 2 was found to be unsuitable for use with the DUV light, requiring a different photo-resist to be used, namely NOA81. The initial structures written were much larger than anticipated, requiring Pulse width Modulation (PWM) to reduce the curing dosage applied to the structures to a few %. The effect of the reduced curing dosage via PWM was explored and it was shown that by reducing the duty cycle, the structures became thinner as well, with the thinnest structures being 2.8 μm wide, with a 1.6 % duty cycle. This is smaller than what was possible with the visible μ-LEDs, which is

partially due to the physical size of the μ-LEDs used being smaller than in Chapter 2. Given that the same stage speed was used between curing at both wavelengths, the curing time was the same as well. However, this comes at the expense of having a lower curing dosage: compared to the dosage of 220 mJcm^{-2} achieved with the visible photolithography, the smallest DUV μ-LED was only capable of 9.1 mJcm^{-2}. Finally, the profiles of the structures were explored with an optical profiler, which showed that the structures were adequately uniform perpendicular to the stage movement, but not parallel to the stage movement, resulting in uneven structure height.

Chapter 4

Hyperspectral Single Pixel Imaging

Chapter 2 deployed positioning through structured illumination by a μ-LED array in a direct writing system, using an RGB camera as the detector. However, the system did not demonstrate an actual advantage over traditional RGB camera vision with flood illumination. In this Chapter, hyperspectral alignment capability in a direct writing system is demonstrated with 0.3 nm spectral resolution and a 16×16 spatial grid using 2048 spectral windows with a 20 μm resolution. The 16×16×2048 hyperspectral data cube was generated using structured illumination from a GaN μ-LED array, confocal with the photolithographic curing source, which in this case is a single μ-LED.

Spectral information was obtained through a single-pixel camera technique using a fibre-coupled spectrometer as detector, called Hyperspectral Single Pixel Imaging (HSPI). Compressive sensing is used to determine the position of fluorescent markers within the field of view within only 32 measurements, i.e. reducing the hyperspectral dataset required for positioning by a factor of eight to 32×2048. Different fluorescent markers were identified through hyperspectral analysis methods such as spectral filtering, spectral fitting, and principal component analysis (PCA). The functionality of the system is demonstrated via the example of two different red fluorescent markers which can only be distinguished through detailed spectral information. The contents of this Chapter have been published in [114].

4.1 Illumination pattern sequence used

As discussed in Chapter 1, when undertaking Single Pixel Imaging (SPI), it is important to consider the patterns that are being sent. There are multiple pattern types to choose from for the spatial and temporal resolution required in SPI. The simplest of these is a raster scan, where each element in the illumination array is lit up sequentially. By measuring the response from each element, a frame can be made by multiplying the measured response by the sent pattern. In this raster example, the sent patterns are arrays of zeros other than a single 1 where the μ-LED is on. The frames are then summed to get a final image.

The Hadamard pattern sequence, as originally described in Section 1.11.5, is suitable for HSPI as it has half of the μ-LEDs illuminated in any one Hadamard pattern, compared to the raster scan, which uses a single LED in each pattern, while also being orthogonal to the next pattern. Another pattern set, the Moving Bars pattern sequence, again described in Section 1.11.5, can also fulfil most of these criteria [76] [71], with a similar proportion of the μ-LEDs on at any one time. While not all of the patterns are orthogonal to each other, the other criteria are fulfilled. However, the output of this approach lacks rotational symmetry, making it less suitable for human scale positioning. The Moving Bar patterns are shown in Figure 4.1. Data taken using this pattern sequence is compressively sensed, with 32 patterns used for positioning rather than the 256 required with a raster scan.

4.2 Experimental Setup for hyperspectral alignment and direct writing

Adding the hyperspectral imaging capability to the system from Chapter 2 requires a change to the experimental system. Figure 4.2 shows the experimental setup used, with the same GaN μ-LED arrays, mirrors, and lenses as in Chapter 2.

The detection system is significantly different from Chapter 2, however. An air spaced doublet collimator lens (CL in Figure 4.2: F810SMA-543, f/1.9) focuses the microscope image into an optical fibre, (Ocean Insight QP600-2-SR-BX) linked to a

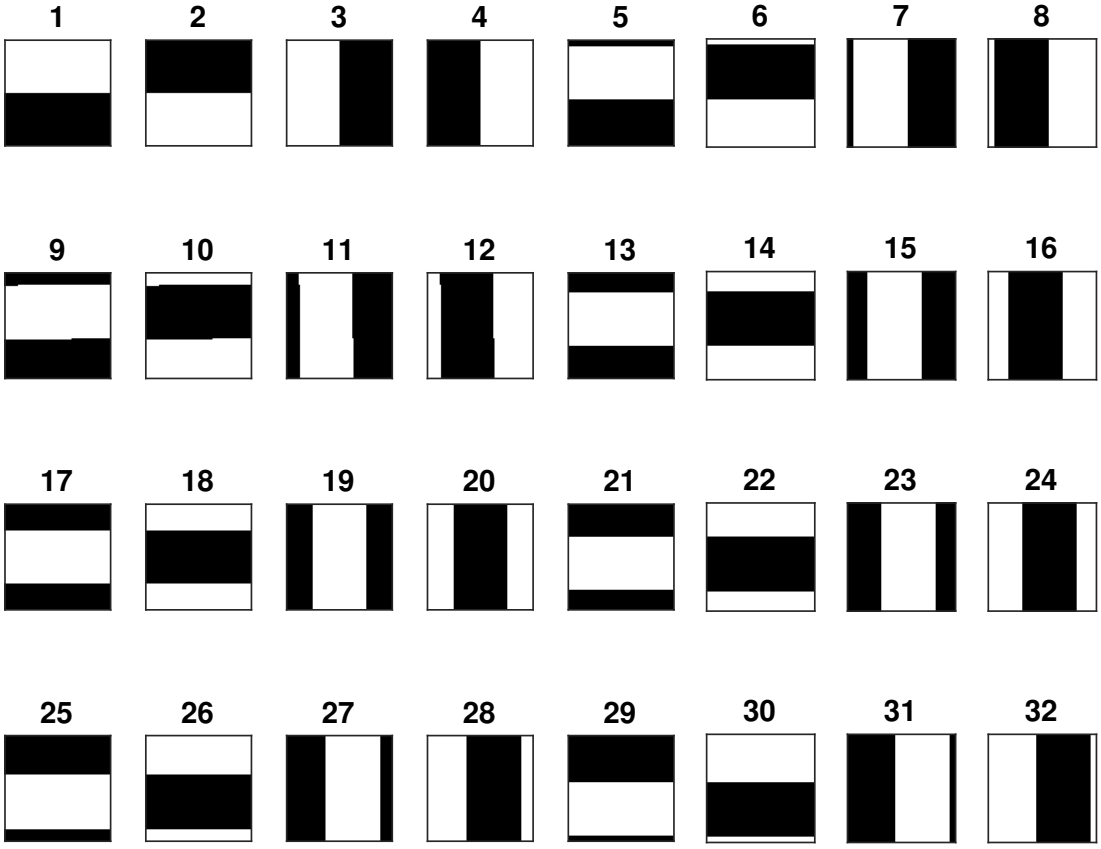

Figure 4.1: The moving bars patterns used in this Chapter.

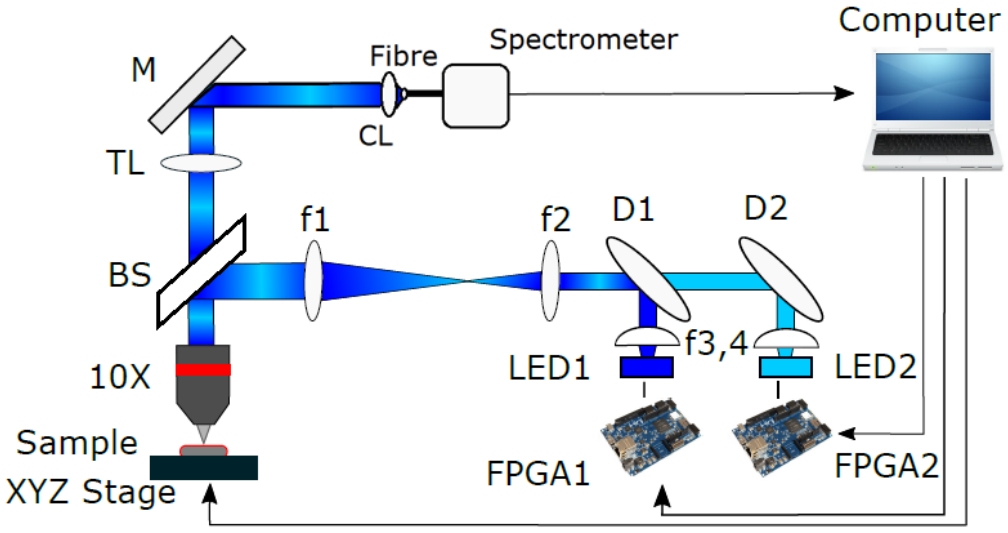

Figure 4.2: Schematic diagram of the experimental setup.

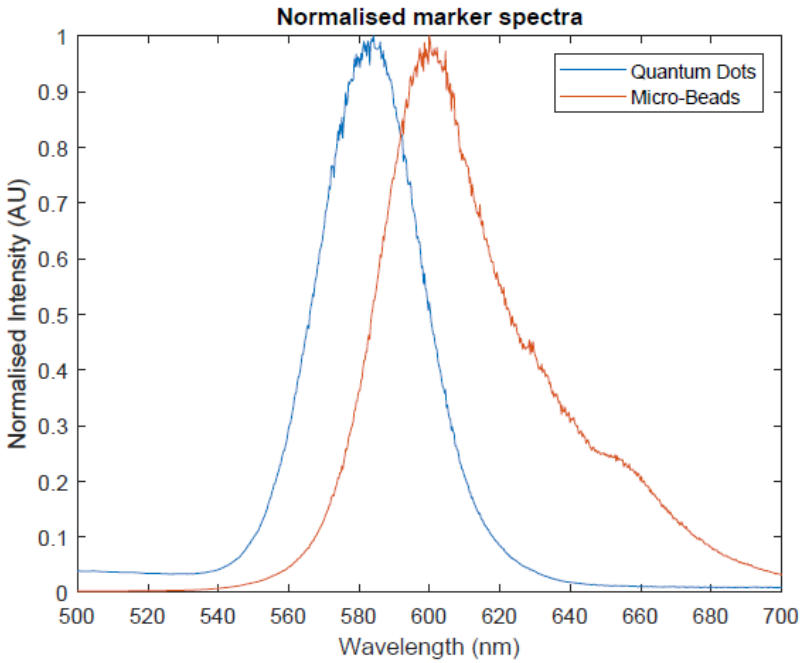

Figure 4.3: Normalised marker spectra for the two types of markers.

spectrometer (Avantes Starline Avaspec 2048-L, spectral resolution 0.3 nm), which is used as the single pixel hyperspectral detector. The collimator lens is vital to increase the Field of View (FoV) of the spectrometer; the full width half maximum of the μ-LED array brightness, used as a measure of the FoV, increases from two projected μ-LED pixels without the collimator lens to ten projected pixels with it, or to about 400 μm in diameter, roughly matching the dimension of the 450 nm array.

4.2.1 Fluorescent Markers

The markers used in this work are dyed polyethylene micro-beads (Cospheric fluorescent red polyethylene microbeads, 10-22 μm in diameter), as used in Chapter 2, and Cd-Se Quantum Dot (QD) clusters, suspended in water. For hyperspectral alignment, the marker types must be spectrally distinct from each other. Figure 4.3 shows the normalised spectra for the respective markers, which shows that they are spectrally distinct.

Borosilicate glass slides are used as a substrate during positioning and photo-curing. To have both marker types within the FoV of the fibre, the QDs are drop cast onto a slide, which is then spin-coated at 3200 rpm for 20 s. If a higher concentration of QD clusters is required, they can be left to dry at room temperature to evaporate the water off after drop casting, instead of spin-coating. The microbeads are then added to a small amount of the photoresist used in Chapter 2 at a ratio of 1.5 mg/μl, which is drop cast again on top of the QDs and spin-coated at 3200 rpm for 20 s. This randomly distributes the markers throughout the sample, so it is not possible to ensure the position of the markers, or to determine if a sample has a suitable area for the alignment procedure before examination of the sample.

4.3 Hyperspectral Alignment Procedure

The procedure of aligning the writing tool to the position of the fluorescent markers is schematically illustrated in Figure 4.4. The positioning μ-LED array displays a time-sequence of spatial illumination patterns, which result in a unique Temporally Modulated Illumination (TMI) at the position of the marker. Here, the same moving bars pattern sequence as in Chapter 2 was used because it provides a good trade-off between the number of patterns required and resilience against noise in the received signal. In the case of the 16×16 μ-LED array used in this work, this results in 32 positioning patterns, augmented by 2 pilot patterns for synchronisation. Spectra were recorded at triple the pattern update rate, thus allowing a comfortable margin to the Nyquist sampling limit, which requires that the spectra are recorded at double the pattern update rate. Subsequent synchronisation to the pilot patterns enabled extraction of a hyperspectral dataset of 1 spectrum per illumination pattern, i.e. 32 spectra in the case of the moving bars sequence.

This hyperspectral dataset may still contain a dynamic background, consisting of the long-wavelength tail of LED emission that was coupled into the spectrometer through diffuse and/or specular reflection on the sample. Therefore, an optional dynamic background subtraction method was implemented. The spectrum of the dynamic background was estimated by measuring the LED spectrum separately, and then using

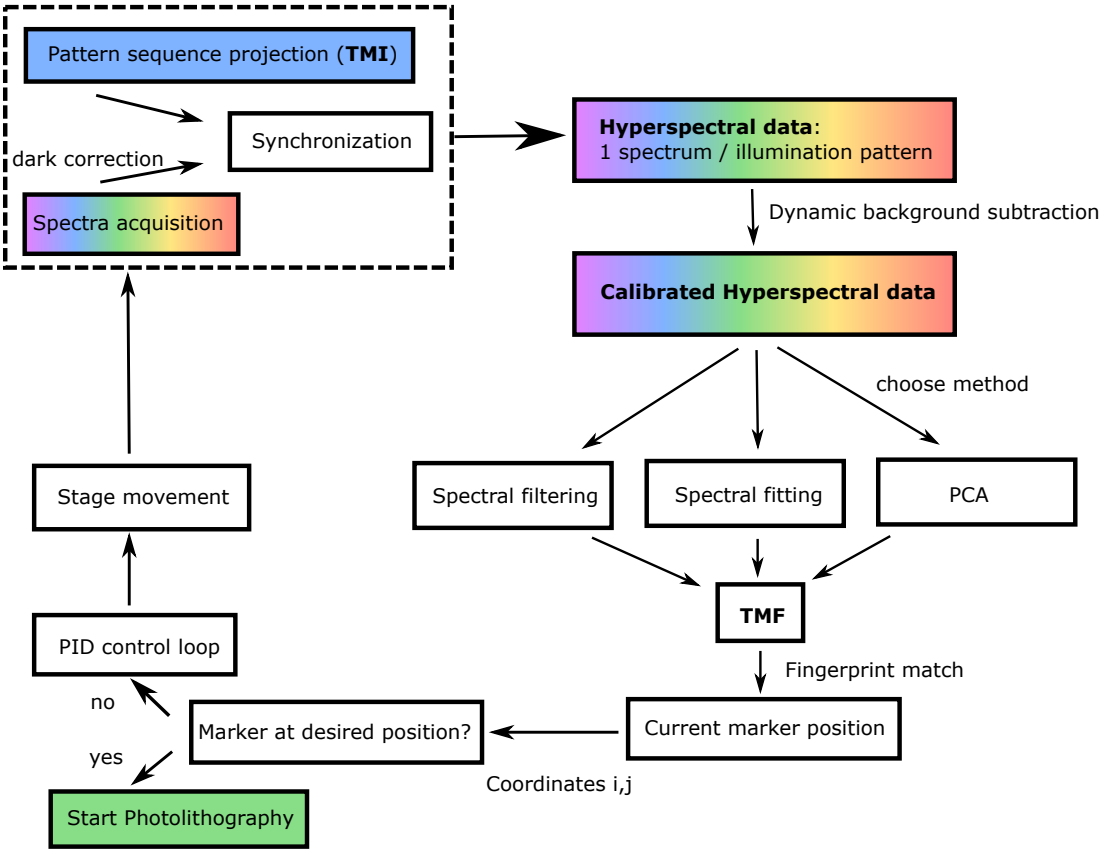

Figure 4.4: Flow diagram of the alignment procedure.

the short-wavelength tail of the LED component in the hyperspectral data to scale the LED spectrum amplitude for each pattern and then subtract it from the spectrum corresponding to that pattern.

After this calibration step, a range of hyperspectral analysis methods is available to extract the Temporally Modulated Fluorescence (TMF) of the marker from the hyperspectral data. In this work spectral filtering, spectral fitting, and PCA were used, each of which is discussed in detail below. The possibility of distinguishing markers will depend on the signal to noise ratio (SNR) of the TMF, and the magnitude of the differences between the emission spectra of the two markers. Therefore, the best possible results are achieved with markers that have similar emission intensity. The TMF should follow the TMI at the marker location, and since each grid site in the 16×16 array grid has a unique fingerprint TMI, the grid site coordinates can directly be found by fingerprint-matching the TMF to the corresponding TMI. The position was then fed into a proportional-integral-derivative (PID) controller of the sample translation stage to move the marker to a desired position. Once that position was reached, there was an additional round of marker positioning to ensure the marker was in the correct place before the direct-writing photolithography process was started.

4.3.1 Spectral Filtering

The simplest method for TMF extraction is to sum the intensities of all wavelength channels within a pre-defined wavelength region matching the peak emission of the markers. For samples containing only micro-beads, a wavelength window of 580 nm to 605 nm was used. For samples containing both types of markers, two spectral windows at 575 nm and 610 nm were used, c.f. Figure 4.3. Further investigation is possible to further refine these windows, and would be dependent on the exact shape of the fluorescence spectra and the SNR of each signal.

Due to its simplicity, this technique was utilised for in-situ automated alignment work done in this chapter. While this method is simple, it is unable to separate the spectral overlap between two spectra; therefore, each marker used must have its own separate spectrum. If the two markers have a significant overlap, then simple spectral

filtering may have significant cross-talk and other methods such as spectral fitting or PCA may be advantageous.

4.3.2 Spectral Fitting

Each spectrum of the hyperspectral dataset can be fitted as a superposition of background components and signal components. Here, a linear background was used, with two different representations of the signal component. The first option was to use the known fluorescence spectra shown in Figure 4.3, and the second option was fitting a Gaussian peak. In both cases, the amplitude obtained through the fit was then the resulting TMF value. Spectral fitting was performed within the the wavelength range between 550 nm and 650 nm. In this Chapter, this technique was done on data after the experiments were undertaken.

4.3.3 Principal Component Analysis (PCA)

If a signal is made up of one or more components, it can be possible to deconstruct the signal into its constituent parts. In anticipation of 2-4 meaningful spectral components, PCA was performed following the method described in [115] with 10 principal components (PCs). This technique splits a received signal into 10 separate, orthogonal channels. It was expected that three meaningful PCs would be received, one from the tail-end of the μ-LED illumination, and one from each marker type. It was found that three components were significant, with the remaining 7 components displaying noise. Two of the significant PCs were associated mainly with LED emission, and one was mainly associated with fluorescence from the target. Figure 4.5 shows the spectra of the three meaningful PCs. PC3 resembles the anticipated fluorescence spectrum best, and the eigenimage of PC3 was used as the TMF for position determination; it seems to be a mixture of both types of markers, as both of their spectral peaks are visible in its spectrum. Due to its computational complexity, this technique was not used in-situ with the automated alignment system.

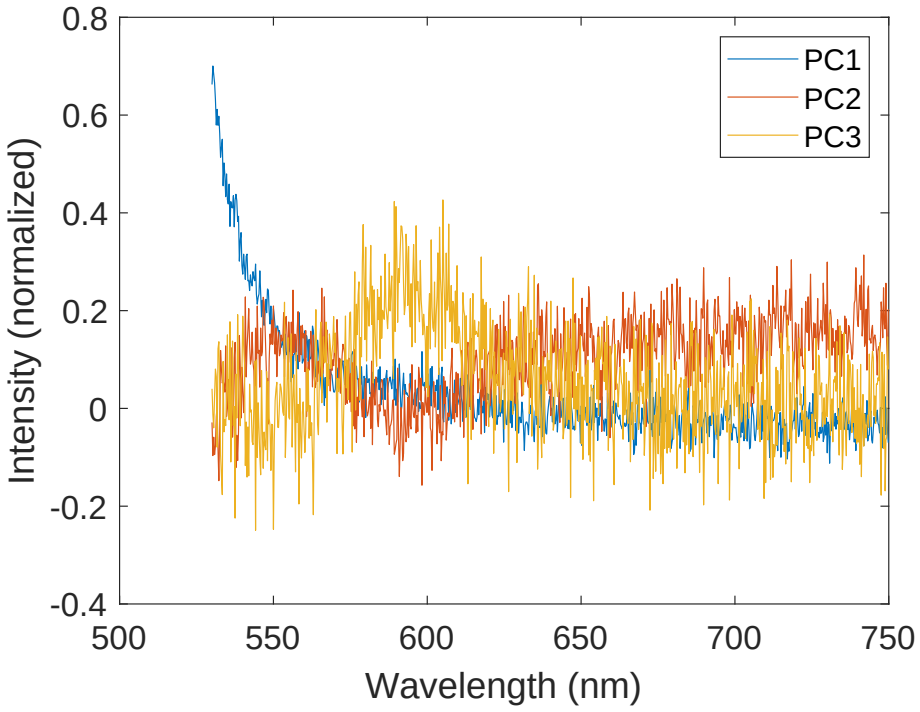

Figure 4.5: Spectra of principal components.

4.4 Positioning Results

A key step that goes beyond Chapter 2 is the extraction of the TMF from hyperspectral data. To evaluate this process, a sample with fluorescent microbeads was prepared and a microbead was put close to the centre of the field of view. For reference, a $16\times16\times2048$ hyperspectral data cube is generated by raster scanning. Figure 4.6(a) shows this raster scan, spectrally filtered for wavelengths 580–605 nm. The position of the microbead at grid site (7,8) can clearly be identified, and the fingerprint TMI at this location is shown in Figure 4.6(b). The performances of the different hyperspectral TMF extraction methods was then demonstrated by using the fingerprint TMI as ground truth for comparison.

In Figure 4.6, the TMI and TMFs are plotted as a temporal sequence, where the x-axis corresponds to the pattern number in the temporal sequence of illumination patterns. All data points are part of a single sequence of TMI/TMF values; however, they have been visually grouped to aid identification of key features within the TMI/TMF.

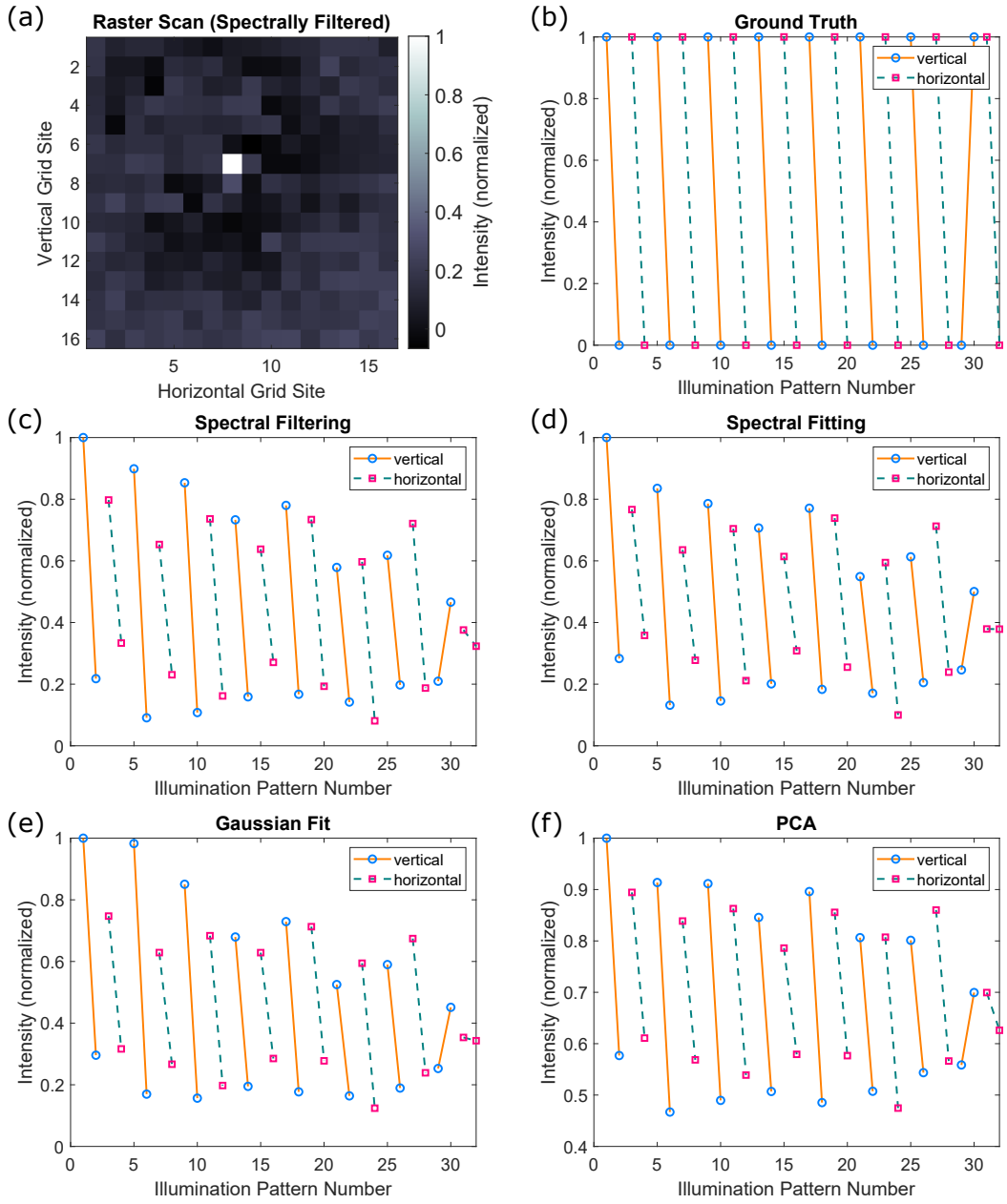

Figure 4.6: TMF of a micro-bead close to the center of the field of view at position (7,8). (a) Raster scan for reference, (b) ground truth for TMI at position (7,8), (c)-(f) experimentally measured TMF. The experimental TMFs were extracted from the hyperspectral data by (c) spectral filtering, (d) fitting with known micro-bead fluorescence spectrum, (e) fitting with a Gaussian peak, and (f) PCA.

The pattern sequence uses differential signalling, and the TMI/TMF values for each inverse pattern pair are connected through a straight line (either solid or dotted). Importantly, the position information is given by the sign of the gradient of these lines.

The pattern sequence contains patterns for vertical alignment (corresponding differential pattern pairs shown by blue circle markers and orange solid lines), and horizontal alignment (corresponding differential pattern pairs shown by magenta square markers and green dashed lines). As each pattern in Figure 4.6 is illuminated upon the sample, there will be a response from the sample at the wavelength channels monitored. Figure 4.6 (b) shows the idealised version of the response expected to be seen for a marker at the grid site (7,8) found by the raster scan in Figure 4.6 (a), from which the performances of the different hyperspectral TMF extraction methods were demonstrated by using the fingerprint TMI as a ground truth for comparison.

The TMFs extracted by each method are shown in Figure 4.6(c)–(f). All methods TMFs identify the marker position correctly, i.e. the differential pattern pairs have the same gradient sign as the ground truth. The different methods are also broadly consistent with each other with respect to the relative magnitude of the individual differential transitions. The last horizontal pattern pair has a poor SNR compared to the other pattern pairs, which is potentially a sign of the marker being close to the boundary of the two grid sites, leading to optical cross-talk. This shows the power of the positioning capability, because as long as the system is within the projected μ-LED array, accurate positioning is possible. Given the overall similar performance of the different methods, spectral filtering was subsequently used in the application of the method to direct writing.

It is important to note that these data were taken with one marker of each type (QD cluster and micro-bead) in the FoV of the positioning μ-LED array. It is possible to detect whether or not there is more than one of each marker type, but this will lead to ambiguities in the reported position. With n identical markers within the FoV of the positioning μ-LED array, there will be n^2 possible marker positions from the initial moving-bars positioning sequence. To reduce these to the n actual positions of the identical markers, additional patterns are needed to be added to the sequence, with at

most $n^2 - n$ additional patterns required.

Data with and without dynamic background subtraction were both tested. Overall, the observed difference was small in most cases except for PCA. Dynamic background subtraction provided a small benefit when spectral fitting with a known spectrum. In this case, fitting without dynamic background subtraction mis-identified the last differential pattern pair and thus resulted in a positioning error of one grid site, which would have been picked up by the extra positioning round if the marker was moved to this position. For PCA, results were consistently better without dynamic background subtraction, and in some cases significant positioning errors were observed when using dynamic background subtraction together with PCA, and was therefore not used with the PCA technique.

It is believed that dynamic background subtraction can help enhance the significance of the fluorescent peak in a narrow spectral window relevant to filtering and fitting, but it may induce additional complexity to the overall spectral composition of the signal across the entire spectral range and thus have a detrimental effect on PCA.

The data shown in Figure 4.6 were obtained with dynamic background subtraction for all methods except for the PCA result, which was obtained without dynamic background subtraction.

4.5 Application to Direct Writing

In order to demonstrate an advantage over conventional camera-based positioning, a sample was prepared that contained both colloidal QD clusters and fluorescent micro-beads. To an RGB camera, both markers are indistinguishable as fluorescence is mostly seen in the red channel. Hyperspectral analysis enables appropriate identification of each marker.

After sample preparation following the procedure described above in section 4.2.1, an area was selected that had one QD cluster and one micro-bead in the FoV of the structured light positioning grid. By spectral filtering for a narrow wavelength range near the fluorescence peaks in Figure 4.3, TMFs were first obtained for the QD cluster

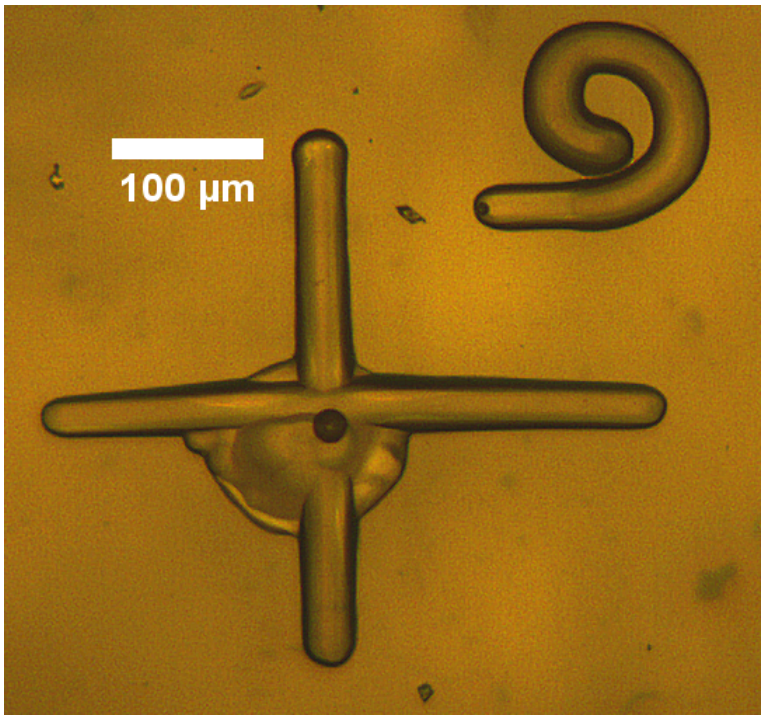

Figure 4.7: Micrograph of photoresist patterns aligned with fluorescent markers. A cross pattern is aligned with a colloidal quantum dot cluster and a spiral pattern is aligned with a fluorescent microbead. The cross is very much overexposed.

and after automatic alignment following the procedure in Figure 4.4, a cross-shaped pattern was exposed centred around the QD cluster. Then TMFs were first obtained for the microbead and after automatic alignment, a spiral-shaped pattern was exposed aligned to the QD cluster. Afterwards, the photoresist was developed.

Initial results are shown in Figure 4.7. While the markers are close enough to have been within the FoV of the blue positioning μ-LED array, this showcases a potential issue if the curing LED is left on for too long during the curing process, overexposing the photoresist.

Representative results without overexposure are shown in Figure 4.8. The structure on the left, with the Quantum Dot cluster used as the marker, required two sets of positioning to cure, therefore making this technique suitable for multi-step processing. This requires the marker to be within the FoV of the positioning LED array after the first round of positioning for multi-step processing, done by returning the marker to the starting position of the first photolithography step. The structure on the right,

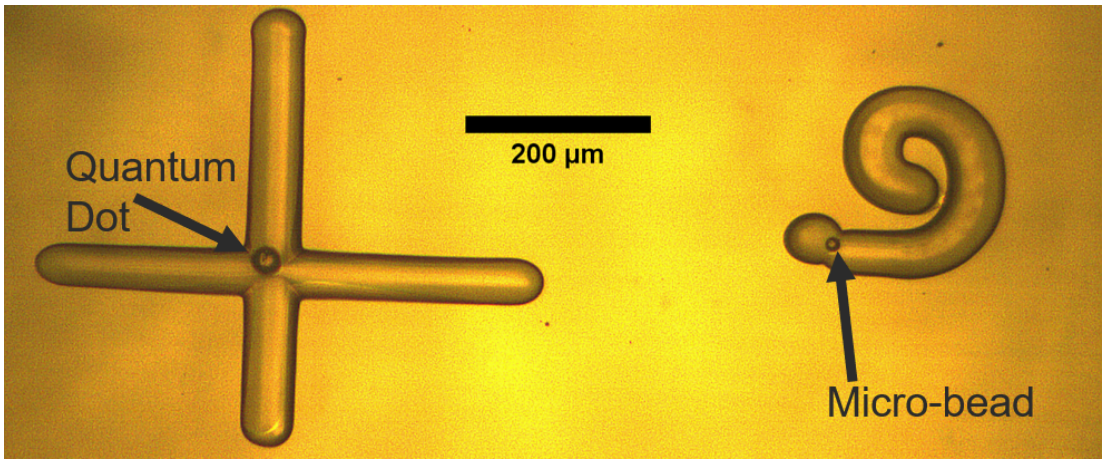

Figure 4.8: Micrograph of photoresist patterns aligned with fluorescent markers. A cross pattern is aligned with a colloidal quantum dot cluster and a spiral pattern is aligned with a fluorescent microbead.

using the micro-bead as the marker, shows that writing curved structures is possible with this setup.

The positioning accuracy of 20 μm achieved here and in Chapter 2 is suitable for general micro-scale photolithography applications, but a higher degree of precision can be required. For example, when trying to photo-cure structures with a fluorescent marker at the centre, the position of the curing μ-LED can be 10 μm away from the centre of the marker. Therefore, to be used for a fully autonomous μ-LED based micro-photolithography system, either smaller projected pixel sizes, which will reduce the FoV of the system, or sub-pixel positioning are required, which would allow positioning within a pixel's projected space, with the aim of having a higher positioning accuracy with the same μ-LED array.

There is scope for improvement in resolution using this technique. The μ-LED array used in this work was designed as a multi-purpose device and not optimised for minimal pixel pitch. There have been significant efforts in commercial research and development of μ-LED arrays for display applications, and pixel pitches of 3–10 μm have been reported [116, 117]. Using the same 4:1 demagnification as in this thesis, such arrays will enable a positioning precision on the order of 1 μm. Similarly small μ-LEDs or lasers can be used for curing to achieve a feature size matched to the precision

of the positioning method.

4.6 Conclusion

This Chapter discussed Hyperspectral Single Pixel Imaging (HSPI). The patterns that were sent for the Single Pixel Imaging (SPI) were shown and how this can be done with a 16×16 blue LED array. The ability of SPI for positioning and imaging was discussed, and ability to do spectral imaging by looking at different wavelengths when imaging to reveal new information. An exploration of the errors involved was made. The HSPI imaging system was then incorporated into the μ-LED based Direct Writing system outlined in Chapter 2. The positions and identity of markers with certain spectral signatures was extracted from the recorded hyperspectral data through spectral filtering, spectral fitting, or principal component analysis. Individual photolithography structures aligned with different types of fluorophores were made on the same substrate. It was demonstrated that two different types of alignment markers could be identified, and bespoke photoresist structures created aligned to each of them. Finally, spectra reconstruction was done; principle component analysis of the spectral data and least squares fitting algorithm based reconstructions yielded satisfactory results.

Chapter 5

Conclusions

The research work presented in this thesis focuses on the design and development of a μ-LED based micro-photolithography system, using both visible and deep ultraviolet emitting μ-LEDs, the former of which is controlled by CMOS technology. To add intelligence to the micro-photolithography system, an automated micro-scale positioning algorithm was developed, capable of positioning down to 20 μm, with Section 4.5 discussing how this resolution can be decreased further.

The system used both a CCD camera and spectrometer for automated positioning, the latter of which enabled hyperspectral single pixel imaging, and therefore could position with more than one marker within the field of view, provided that the markers have spectral differences.

The first chapter of this thesis provides a theoretical background to the work.

In Chapter 2, a direct writing system using μ-LED arrays was built and characterised, with reasoning given behind the main design choices made. Much of the groundwork for the rest of the thesis was reported here, which was particularly relevant to Chapter 4. Experimental techniques were shown and the automated positioning algorithm was explained, from design choices made during the algorithm construction to showing results in the positioning. Photolithography using the setup was then discussed and the curing itself optimised, with the dosage and width of the structures reliant on the duty cycle of the curing μ-LED, and the structure smoothness reliant on the frame rate, resulting in structures 20 μm wide. The dosage of the photolithography

system was estimated at 220 mJcm^{-2}. Shorter focal length lenses and smaller μ-LEDs were used in an attempt at curing smaller structures, where it was found that the shorter focal lenses resulted in dual exposure on the photoresist, one from exposing the top of the material, and another from reflecting off the bottom surface of the sample.

In Chapter 3, a Deep Ultraviolet (DUV) direct writing photolithography system using μ-LEDs was shown. The μ-LEDs used were characterised, with the current draw during photolithography and measured power increasing with μ-LED mesa size, while the turn on voltage decreased with increasing mesa size. The photolithography setup was characterised by undertaking a dosage calculation of the setup; this was done by measuring the μ-LED projected spot size and the curing power at the sample position. Successful structures were made using a different photo-resist to Chapter 2. The curing dosage of the system was estimated at 755 mJcm^{-2} for the largest LED with diameter 200 μm, down to 9.1 mJcm^{-2} for the smallest successful curing using a LED of diameter 40 μm. This lowest dosage utilised pulse modulation to reduce the size of the cured structure, with a 7 μm wide structure possible from a 1.6 % duty cycle.

Chapter 4 discusses the Hyperspectral Single Pixel Imaging (HSPI) that was done in the project. The patterns that were used for the Single Pixel Imaging (SPI) were explained and it was shown how this can be applied with a 16×16 blue μ-LED array. The ability of SPI for positioning and imaging was discussed, and ability of spectral imaging by looking at different wavelengths when imaging to reveal new information, with a focus on spectral imaging and the errors involved. The HSPI system was then added to the direct writing system from Chapter 2, being used for positioning and aligning to two different types of fluorescent markers within the μ-LED array's field of view, from which bespoke photoresist structures were cured.

5.1 Future Work

There are a number of future research topics to continue the work detailed within this thesis, which will be explored in this section. The first of these is to improve the direct writing system itself, and how this work can be developed for industrial scale electronic

manufacturing using μ-LEDs. Then other possible applications of the main system developed in this thesis will be explored. These include Fluorescence Lifetime Imaging Microscopy (FLIM), changing the detector, or reducing the feature size for a better positioning resolution by adding in a Digital Micro-mirror Display (DMD).

5.1.1 Future of Direct Writing Photolithography with μ-LEDs

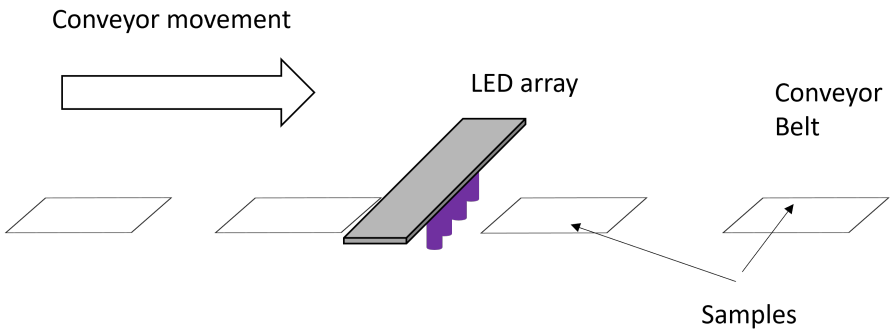

Figure 5.1: Potential idea for a future, completely automated μ-LED based photolithography setup for mass manufacturing.

To accommodate the scale required for industrial scale electronic manufacturing, the time spent photocuring needs to be reduced. In order to reduce this time, either the μ-LED power could be increased, or the speed of the stage while curing could be increased. Another way to improve the performance of the system is by rethinking it entirely. Instead of a 2D square array, a potentially suitable μ-LED geometry is a 1D linear array, a format common in the literature [118], [119], [120]. This would allow large scale automated photolithography with μ-LEDs and a 'conveyor belt' moving a row of samples with the photoresist deposited on them. The linear array can then be programmed with a series of high frame rate signals at the curing wavelength to cure each sample with the desired pattern. An example of how this might look is shown in Figure 5.1. The purple beams represent the μ-LED light being focused onto the samples, curing the structures as the sample moves under it. The idea would be that by the time the sample has moved out of the area illuminated by the linear μ-LED array, one photo-curing step has been completed for the full sample.

This new system would require a high μ-LED power and switching speed to have

the highest available output from this automated system. Markers can be placed at various positions in the samples for positioning purposes throughout processing, and 2D arrays positioned at various points to allow for positioning to occur.

5.1.2 Increased resolution in direct writing

Another way of improving the direct writing system would be to have a higher resolution with the same field of view, or having smaller pixels. Before going further into this topic, it is important to note here that the μ-LED arrays used were not optimised for the smallest pixel pitch, and arrays with micron scale pitches have been demonstrated in the commercial sector [116, 117]. However, increasing the illumination resolution at the sample level results in higher resolution single pixel images, and smaller feature sizes for direct writing. A higher resolution single pixel image would reduce the error in positioning. This can be achieved in one of two ways: reducing the pixel pitch of the illumination, as described above, or adding in a higher resolution reflector into the system.

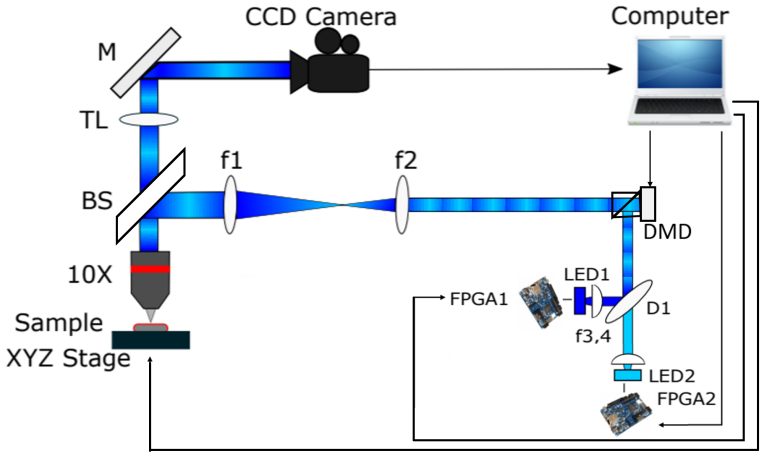

Figure 5.2: Schematic of adding a DMD to the direct writing system used throughout this thesis

A high resolution reflector in the system could be a DMD. An example of such a system, based on the system used throughout this thesis, is shown in Figure 5.2. In this system, the DMD is placed after the collimation lenses from the two μ-LED boards, so that the demagnification can be done on the increased resolution illumination afforded

by the DMD. This should result in much higher resolution images, dependent on the size of the μ-LED array projected onto the DMD.

5.1.3 Fluorescence Lifetime Imaging Microscopy

Another potential application of the direct writing system is possible by changing the detector used in the system. For example, a detector with a fast time detection, such as a single pixel avalanche diode or a photomultiplier tube used instead of the spectrometer in Figure 4.2 would allow the system to take images as a a function of time down to a picosecond timescale, and at very low light levels. As a result, Fluorescent Lifetime Imaging Microscopy (FLIM), a technique often used in bio-imaging [35], is possible using the same direct writing system used throughout this thesis, while pulsing the μ-LEDs.

FLIM is used as an non-invasive imaging method that can be used to determine characteristics of the sample such as temperature, fluorophore concentration and pH from the photon arrival time histogram. Being a non-invasive technique, this allows measurements to be made on otherwise delicate samples, where the samples may break down if invasively measured, or if they are photosensitive. Time of flight measurements are taken multiple times, making a histogram of the arrival times, and it is expected that the fluorescence decays exponentially [121], in a technique called Time Correlated Single Photon Counting (TCSPC). The pulses that are sent for FLIM are in the few-photon regime, requiring statistical analysis as each pulse sent may not result in an output photon.

5.1.4 Multi-coloured μ-LED arrays

While the images taken during Chapter 4 were hyperspectral given the amount of fine channels used, it could be argued that due to the single colour of μ-LED that is used for illumination, this is not a full colour image. As a result, an array containing differently coloured μ-LEDs might be constructed to allow for multicolour single pixel images. This assumes that the μ-LEDs are individually addressable, the same as in the single colour μ-LED arrays used previously, and the ability to make multiple coloured μ-LEDs

and attach them onto the same circuit for individual addressing. While imaging using multiple different coloured μ-LEDs has been done [122], SPI using multiple coloured μ-LEDs has not been reported and thus would be an interesting avenue of research. This could allow applications that have been previously attempted with SPI to use multiple wavelengths of light simultaneously. There is the potential for even more fluorescent markers within the FoV, for example, which are each excited by different wavelengths of light. This work would then tie into the HSI done earlier by then allowing many more wavelengths of fluorescence to be used for giving instructions to a system, as shown in Chapter 4.

This is reliant on the ability of the array to have multiple wavelength emitting μ-LEDs arranged into a square array, to be as similar as possible to the arrays that have been used throughout this thesis, and to get a 2D square image output, to be comparable to other imaging techniques. A schematic example of such an array is shown in Figure 5.3, where different pixels in the array are different wavelength bands, in this case blue, green, yellow, and red, centred around four different wavelength bands; these are centred around 450, 525, 580, and 640 nm. Keeping the pattern of the colours is vital; it allows the same square patterns to be made and illuminated as before, albeit with a theoretical maximum fill factor of 25 % for each wavelength band.

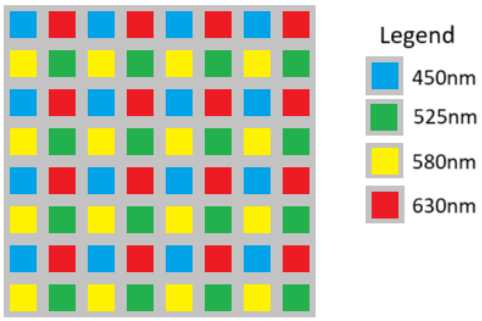

Figure 5.3: Example multicoloured LED array showing the different colour LEDs. Each different colour pixel in the device refers to a different wavelength band - blue is centred around 450 nm, green around 525 nm, yellow around 580 nm, and red around 630 nm.

5.2 Application of this work

This thesis has demonstrated a new capability; that is, the ability of automated positioning on a milli-micro scale using Hyperspectral Single Pixel Imaging and fluorescent markers. This technique, when combined with making unique instructions for different colours of fluorescent markers, can allow for easier rapid prototyping. By starting each prototype with a different coloured marker, by being mindful of the size of the structures made, it would be possible to automate numerous prototypes on the same sample.

In terms of additional capacities enabled by this technology, it would also be able to use the markers themselves as functional elements. For example, by electrically contacting to individual fluorescent quantum dot clusters, it would then be possible to have structures cured relative to the clusters. This would allow atom-like electro-optic stimulation, and could potentially be used as an on-chip light source for photonic integrated circuits, with waveguides being made from the photolithography steps. With an increase in the resolution, it might even be possible to align to individual quantum dots themselves, as opposed to the clusters used throughout this thesis.

5.3 Final Conclusion

In conclusion, electronically interfaced μ-LED arrrays allow many new avenues for smart direct-writing and structured illumination systems. They can be used as a central part of an indoor illumination arrangement affording automated positioning to fluorescent markers, both on the macro- and micro-scale. CMOS control enables a high pulse rate and individual μ-LED pixels to be used for photo-curing, and finely tuned control over the dosage. The combination of these three elements allow for highly customisable patterns that can be made in photoresist.

Appendix A

Publications

Journal publications

Mark Stonehouse, Alex Blanchard, Benoit Guilhabert, Ian Watson, Erdan Gu, Johannes Herrnsdorf, and Martin Dawson. Microscale automated alignment and spatial tracking through structured illumination. doi: 10.15129/7cf60f24-0678. URL: https://doi.org/10.15129/7cf60f24-0678-.

M. Stonehouse, A. Blanchard, B. Guilhabert, Y. Zhang, E. Gu, I. M. Watson, J. Herrnsdorf, and M. D. Dawson. Automated alignment in mask-free photolithography enabled by micro-LED arrays. *Electronics Letters*, 57:721–723, 2021. ISSN 0013-5194. doi: 10.1049/ell2.12244.

A. Blanchard, P. R. Edwards, B. Guilhabert, E. Gu, I. M. Watson, and J. Herrnsdorf. Hyperspectral alignment capability for direct writing systems enabled by structured illumination with a micro-LED array. *J. Opt.* **27** 055402, doi:10.1088/2040-8986/adcfb0.

Oral publications at conferences

M. Stonehouse et al., "Microscale Automated Alignment and Spatial Tracking through Structured Illumination," 2019 IEEE Photonics Conference (IPC), San Antonio, TX, USA, 2019.

A. Blanchard et al., "Hyperspectral single pixel imaging using visible light emitting

diode arrays and spectrometer for microfabrication applications", Photon Conference, Online, 2020.

A. Blanchard et al., "Hyperspectral Single Pixel Imaging with GaN μ-LED arrays for microscale positioning of fluorescent markers", International Workshop on Nitrides, Berlin, Germany, 2022.

Bibliography

[1] Mark Stonehouse, Alex Blanchard, Benoit Guilhabert, Ian M. Watson, Erdan Gu, Johannes Herrnsdorf, and Martin D. Dawson. Microscale automated alignment and spatial tracking through structured illumination. In *2019 IEEE Photonics Conference (IPC)*, pages 1–2, 2019. doi: 10.1109/IPCon.2019.8908309.

[2] M. Stonehouse, A. Blanchard, B. Guilhabert, Y. Zhang, E. Gu, I. M. Watson, J. Herrnsdorf, and M. D. Dawson. Automated alignment in mask-free photolithography enabled by micro-LED arrays. *Electronics Letters*, 57:721–723, 2021. ISSN 0013-5194. doi: 10.1049/ell2.12244.

[3] Chan-Wook Jeon, Enternal Gu, and Martin Dawson. Mask-free photolithographic exposure using a matrix-addressable micropixellated AlInGaN ultraviolet light-emitting diode. *Applied Physics Letters*, 86:221105–221105, 05 2005. doi: 10.1063/1.1942636.

[4] Murat Kaya Yapici and Ilyas Farhat. UV-LED exposure system for low-cost photolithography. *Optical Microlithography XXVII*, 9052:90521T, 2014. ISSN 1996756X. doi: 10.1117/12.2046123.

[5] Jun Ke and Edmund Y. Lam. Fast compressive measurements acquisition using optimized binary sensing matrices for low-light-level imaging. *Optics Express*, 24:9869, 5 2016. ISSN 10944087. doi: 10.1364/oe.24.009869.

[6] S.M. Sze (Editor) and Joseph Round. Semiconductor devices: Pioneering papers. *World Scientific Publishing*, page 879, 1991. URL `http://www.jmargolin.com/history/leds.pdf`.

[7] O.V. Lossev. Cii. luminous carborundum detector and detection effect and oscillations with crystals. *The London, Edinburgh, and Dublin Philosophical Magazine and Journal of Science*, 6: 1024–1044, 11 1928. ISSN 1941-5982. doi: 10.1080/14786441108564683.

[8] W. van Roosbroeck and W. Shockley. Photon-radiative recombination of electrons and holes in germanium. *Phys. Rev.*, 94:1558–1560, Jun 1954. doi: 10.1103/PhysRev.94.1558. URL `https://link.aps.org/doi/10.1103/PhysRev.94.1558`.

[9] Hiroshi Amano, Masahiro Kito, Kazumasa Hiramatsu, and Isamu Akasaki. P-type conduction in Mg-Doped GaN Treated with Low-Energy Electron Beam Irradiation (LEEBI). *Japanese*

Journal of Applied Physics, 28(12A):L2112, dec 1989. doi: 10.1143/JJAP.28.L2112. URL `https://dx.doi.org/10.1143/JJAP.28.L2112`.

[10] Dhanesh Kattipparambil Rajan and Jukka Lekkala. A maskless exposure device for rapid photolithographic prototyping of sensor and microstructure layouts. *Procedia Engineering*, 5:331–334, 2010. ISSN 1877-7058. doi: https://doi.org/10.1016/j.proeng.2010.09.115. URL `https://www.sciencedirect.com/science/article/pii/S1877705810006624`. Eurosensor XXIV Conference.

[11] Ming Fei Chen, Yu Pin Chen, Wen Tse Hsiao, and Zhi Peng Gu. Laser direct write patterning technique of indium tin oxide film. *Thin Solid Films*, 515:8515–8518, 10 2007. ISSN 00406090. doi: 10.1016/j.tsf.2007.03.172.

[12] Alexander J.C. Kuehne, David Elfström, Allan R. Mackintosh, Alexander L. Kanibolotsky, Benoit Guilhabert, Erdan Gu, Igor F. Perepichka, Peter J. Skabara, Martin D. Dawson, and Richard A. Pethrick. Direct laser writing of nanosized oligofluorene truxenes in UV-transparent photoresist microstructures. *Advanced Materials*, 21:781–785, 2 2009. ISSN 09359648. doi: 10.1002/adma.200802656.

[13] Chenying Zhang, Wei Zhou, Da Geng, Cheng Bai, Weida Li, Songyue Chen, Tao Luo, Lifeng Qin, and Yu Xie. Laser direct writing and characterizations of flexible piezoresistive sensors with microstructures. *Opto-Electronic Advances*, 4:1–11, 2021. ISSN 20964579. doi: 10.29026/oea.2021.200061.

[14] Rosanne M. Guijt and Michael C. Breadmore. Maskless photolithography using UV LEDs. *Lab on a Chip*, 8:1402–1404, 2008. ISSN 14730189. doi: 10.1039/b800465j.

[15] D. Elfström, B. Guilhabert, J. McKendry, S. Poland, Z. Gong, D. Massoubre, E. Richardson, B. R. Rae, G. Valentine, G. Blanco-Gomez, E. Gu, J. M. Cooper, R. K. Henderson, and M. D. Dawson. Mask-less ultraviolet photolithography based on CMOS-driven micro-pixel light emitting diodes. *Optics Express*, 17:23522, 12 2009. ISSN 1094-4087. doi: 10.1364/oe.17.023522.

[16] Benoit Guilhabert, David Massoubre, Elliot Richardson, Jonathan J.D. McKendry, Gareth Valentine, Robert K. Henderson, Ian M. Watson, E. Gu, and Martin D. Dawson. Sub-micron lithography using inGaN micro-LEDs: Mask-free fabrication of LED arrays. *IEEE Photonics Technology Letters*, 24:2221–2224, 2012. ISSN 10411135. doi: 10.1109/LPT.2012.2225612.

[17] Duc-Hanh Dinh, Hung-Liang Chien, and Yung-Chun Lee. Maskless lithography based on digital micromirror device (DMD) and double sided microlens and spatial filter array. *Optics and Laser Technology*, 113:407–415, 5 2019. ISSN 00303992. doi: 10.1016/j.optlastec.2019.01.001. URL `https://linkinghub.elsevier.com/retrieve/pii/S0030399218301701`.

[18] Mark Stonehouse, Yanchao Zhang, Benoit Guilhabert, Ian Watson, Erdan Gu, Johannes Herrnsdorf, and Martin Dawson. Digital illumination in microscale direct-writing photolithography: Challenges and trade-offs. 2019. ISBN 9781538673614. doi: 10.1109/BICOP.2018.8658364. URL http://dx.doi.org/10.15129/9b7c92b3-f7ac-4be7-b0b5-ba31ac30c35c.

[19] Tariq Jamil and Muhammad Usman. Optimized carrier confinement in deep-ultraviolet light-emitting diodes with alingan/alinn superlattice electron blocking layer. *Materials Science and Engineering: B*, 278, 4 2022. ISSN 09215107. doi: 10.1016/j.mseb.2022.115638.

[20] Johannes Herrnsdorf, Jonathan J.D. McKendry, Shuailong Zhang, Enyuan Xie, Ricardo Ferreira, David Massoubre, Ahmad Mahmood Zuhdi, Robert K. Henderson, Ian Underwood, Scott Watson, Anthony E. Kelly, Erdan Gu, and Martin D. Dawson. Active-matrix GaN micro light-emitting diode display with unprecedented brightness. *IEEE Transactions on Electron Devices*, 62:1918–1925, 2015. ISSN 00189383. doi: 10.1109/TED.2015.2416915.

[21] E. Fred Schubert. *Light-Emitting Diodes*. Cambridge University Press, 6 2006. ISBN 9780521865388. doi: 10.1017/CBO9780511790546. URL https://www.cambridge.org/core/product/identifier/9780511790546/type/book.

[22] Johannes Herrnsdorf, Yue Wang, Jonathan J.D. Mckendry, Zheng Gong, David Massoubre, Benoit Guilhabert, Georgios Tsiminis, Graham A. Turnbull, Ifor D.W. Samuel, Nicolas Laurand, Erdan Gu, and Martin D. Dawson. Micro-LED pumped polymer laser: A discussion of future pump sources for organic lasers. *Laser and Photonics Reviews*, 7:1065–1078, 11 2013. ISSN 18638880. doi: 10.1002/lpor.201300110.

[23] X. A. Cao, P. M. Sandvik, S. F. LeBoeuf, and S. D. Arthur. Defect generation in inGaN/GaN light-emitting diodes under forward and reverse electrical stresses. *Microelectronics Reliability*, 43:1987–1991, 12 2003. ISSN 00262714. doi: 10.1016/j.microrel.2003.06.001.

[24] C. Grazzi, H. P. Strunk, A. Castaldini, A. Cavallini, H. P.D. Schenk, and P. Gibart. Optoelectronic properties of GaN epilayers in the region of yellow luminescence. *Journal of Applied Physics*, 100, 2006. ISSN 00218979. doi: 10.1063/1.2356780.

[25] K. P. O'Donnell, T. Breitkopf, H. Kalt, W. Van der Stricht, I. Moerman, P. Demeester, and P. G. Middleton. Optical linewidths of InGaN light emitting diodes and epilayers. *Applied Physics Letters*, 70(14):1843–1845, 04 1997. ISSN 0003-6951. doi: 10.1063/1.118728. URL https://doi.org/10.1063/1.118728.

[26] Christian Tantardini and Xavier Gonze. Band gap bowing and spectral width of Ga(1-x)InxN alloys for modelling light emitting diodes. *Physica B: Condensed Matter*, 625:413481, 2022. ISSN 0921-4526. doi: https://doi.org/10.1016/j.physb.2021.413481. URL https://www.sciencedirect.com/science/article/pii/S0921452621006402.

[27] Min Ho Kim, Martin F. Schubert, Qi Dai, Jong Kyu Kim, E. Fred Schubert, Joachim Piprek, and Yongjo Park. Origin of efficiency droop in GaN-based light-emitting diodes. *Applied Physics Letters*, 91, 2007. ISSN 00036951. doi: 10.1063/1.2800290.

[28] N. F. Gardner, G. O. Müller, Y. C. Shen, G. Chen, S. Watanabe, W. Götz, and M. R. Krames. Blue-emitting InGaN-GaN double-heterostructure light-emitting diodes reaching maximum quantum efficiency above 200 Acm^{-}2. *Applied Physics Letters*, 91, 2007. ISSN 00036951. doi: 10.1063/1.2807272.

[29] H. W. Choi, C. Liu, E. Gu, G. McConnell, J. M. Girkin, I. M. Watson, and M. D. Dawson. GaN micro-light-emitting diode arrays with monolithically integrated sapphire microlenses. *Applied Physics Letters*, 84:2253–2255, 2004. ISSN 00036951. doi: 10.1063/1.1690876.

[30] S. X. Jin, J. Shakya, J. Y. Lin, and H. X. Jiang. Size dependence of iii-nitride microdisk light-emitting diode characteristics. *Applied Physics Letters*, 78:3532–3534, 5 2001. ISSN 00036951. doi: 10.1063/1.1376152.

[31] Jianghao Xiong, En Lin Hsiang, Ziqian He, Tao Zhan, and Shin Tson Wu. Augmented reality and virtual reality displays: emerging technologies and future perspectives. *Light: Science and Applications*, 10, 12 2021. ISSN 20477538. doi: 10.1038/s41377-021-00658-8.

[32] Shou-Wei Wang, Sheng-Kai Huang, Yi-Yang Lee, Shao-Yi Weng, Hao-Chung Kuo, and Chien-Chung Lin. A novel geometry for integrated photonic characteristics of colloidal quantum dots and micro-LED. *2021 Conference on Lasers and Electro-Optics (CLEO)*, page SM3D.7, 2021. doi: 10.1364/cleo_si.2021.sm3d.7.

[33] Zaifa Du, Dianlun Li, Weiling Guo, Fangzhu Xiong, Penghao Tang, Xiongtu Zhou, Yongai Zhang, Tailiang Guo, Qun Yan, and Jie Sun. Quantum dot color conversion efficiency enhancement in micro-light-emitting diodes by non-radiative energy transfer. *IEEE Electron Device Letters*, 3106: 1–1, 2021. ISSN 0741-3106. doi: 10.1109/led.2021.3089580.

[34] Frederik Görlitz, David S. Corcoran, Edwin A.Garcia Castano, Birgit Leitinger, Mark A.A. Neil, Christopher Dunsby, and Paul M.W. French. Mapping molecular function to biological nanostructure: Combining structured illumination microscopy with fluorescence lifetime imaging (sim + flim). *Photonics*, 4, 9 2017. ISSN 23046732. doi: 10.3390/photonics4030040.

[35] Taylor Hinsdale, Shuna Cheng, Bilal Malik, Javier A. Jo, Kristen C. Maitland, Maryellen L. Giger, Paras Patel, and John Wright. Optical detection of oral carcinoma via structured illumination fluorescence lifetime imaging. page 32. SPIE-Intl Soc Optical Eng, 3 2018. ISBN 9781510616455. doi: 10.1117/12.2293856.

[36] Mathieu Bozzio, Michal Vyvlecka, Michael Cosacchi, Cornelius Nawrath, Tim Seidelmann, Juan C. Loredo, Simone L. Portalupi, Vollrath M. Axt, Peter Michler, and Philip Walther. Enhancing quantum cryptography with quantum dot single-photon sources. *npj Quantum Information*, 8, 12 2022. ISSN 20566387. doi: 10.1038/s41534-022-00626-z.

[37] Christian Schimpf, Marcus Reindl, Daniel Huber, Barbara Lehner, Saimon F Covre, Da Silva, Santanu Manna, Michal Vyvlecka, Philip Walther, and Armando Rastelli. Quantum cryptography with highly entangled photons from semiconductor quantum dots. *Sci. Adv*, 7:8905–8919, 2021. URL `https://www.science.org`.

[38] Daniel Kage, Linn Fischer, Katrin Hoffmann, Thomas Thiele, Uwe Schedler, and Ute Resch-Genger. Close spectroscopic look at dye-stained polymer microbeads. *The Journal of Physical Chemistry C*, 122(24):12782–12791, 2018. doi: 10.1021/acs.jpcc.8b02546. URL `https://doi.org/10.1021/acs.jpcc.8b02546`.

[39] Mathieu Bottier, Marta Peña Fernández, Gabriel Pelle, Daniel Isabey, Bruno Louis, James B. Grotberg, and Marcel Filoche. A new index for characterizing micro-bead motion in a flow induced by ciliary beating: Part II, modeling. *PLoS Computational Biology*, 13, 7 2017. ISSN 15537358. doi: 10.1371/journal.pcbi.1005552.

[40] Emily C. Anderson, Melissa C. Weston, and Ingrid Fritsch. Investigations of redox magnetohydrodynamic fluid flow at microelectrode arrays using microbeads. *Analytical Chemistry*, 82(7): 2643–2651, 2010. doi: 10.1021/ac9020177. URL `https://doi.org/10.1021/ac9020177`. PMID: 20210341.

[41] Coshperic Spheres. Data sheet for the micro-beads. URL `https://www.cospheric.com/UVPMSBR_fluorescent_red_spheres_density0995.htm`.

[42] R.T. Chen. Polymer-based photonic integrated circuits. *Optics and Laser Technology*, 25(6): 347–365, 1993. ISSN 0030-3992. doi: https://doi.org/10.1016/0030-3992(93)90001-V. URL `https://www.sciencedirect.com/science/article/pii/003039929390001V`.

[43] W. Bogaerts, D. Taillaert, B. Luyssaert, P. Dumon, J. Van Campenhout, P. Bienstman, D. Van Thourhout, R. Baets, V. Wiaux, and S. Beckx. Basic structures for photonic integrated circuits in silicon-on-insulator. *Opt. Express*, 12(8):1583–1591, Apr 2004. doi: 10.1364/OPEX.12.001583. URL `https://opg.optica.org/oe/abstract.cfm?URI=oe-12-8-1583`.

[44] Malte C. Gather, Anne Köhnen, Aurélie Falcou, Heinrich Becker, and Klaus Meerholz. Solution-processed full-color polymer organic light-emitting diode displays fabricated by direct photolithography. *Advanced Functional Materials*, 17:191–200, 1 2007. ISSN 1616301X. doi: 10.1002/adfm.200600651.

[45] Paweł E. Malinowski, Tung Huei Ke, Atsushi Nakamura, Ya Han Liu, Dieter Vander Velpen, Erwin Vandenplas, Nikolas Papadopoulos, Auke Jisk Kronemeijer, Jan Laurens van der Steen, Soeren Steudel, Che Cheng Kuo, Yen Yu Huang, Yu Hsien Chen, Ming Hua Yeh, Gerwin Gelinck, and Paul Heremans. High resolution photolithography for direct view active matrix organic light-emitting diode augmented reality displays. *Journal of the Society for Information Display*, 26: 128–136, 3 2018. ISSN 19383657. doi: 10.1002/jsid.643.

[46] Renzhong Chen, Xuejun Wang, Xin Li, Hongxiang Wang, Mingqian He, Longfei Yang, Qianying Guo, Shen Zhang, Yan Zhao, Yang Li, Yunqi Liu, and Dacheng Wei. A comprehensive nano-interpenetrating semiconducting photoresist toward all-photolithography organic electronics. *Sci. Adv*, 7:659–677, 2021. URL `https://www.science.org`.

[47] John A. Defranco, Bradley S. Schmidt, Michal Lipson, and George G. Malliaras. Photolithographic patterning of organic electronic materials. *Organic Electronics*, 7:22–28, 2006. ISSN 15661199. doi: 10.1016/j.orgel.2005.10.002.

[48] Alphonse Poitevin. *Traité de l'impression photographique sans sels d'argent*, volume 1. Bibliothèque nationale de France, 1 edition, 1862.

[49] Jay W. Lathrop. The diamond ordnance fuze laboratory's photolithographic approach to microcircuits. *IEEE Annals of the History of Computing*, 35:48–55, 2013. ISSN 10586180. doi: 10.1109/MAHC.2011.83.

[50] Gerry O'Sullivan, Bowen Li, Rebekah D'Arcy, Padraig Dunne, Paddy Hayden, Deirdre Kilbane, Tom McCormack, Hayato Ohashi, Fergal O'Reilly, Paul Sheridan, Emma Sokell, Chihiro Suzuki, and Takeshi Higashiguchi. Spectroscopy of highly charged ions and its relevance to EUV and soft X-ray source development. *Journal of Physics B: Atomic, Molecular and Optical Physics*, 48 (14):144025, May 2015. doi: 10.1088/0953-4075/48/14/144025. URL `https://dx.doi.org/10.1088/0953-4075/48/14/144025`.

[51] Harry J. Levinson. High-NA EUV lithography: Current status and outlook for the future. *Japanese Journal of Applied Physics*, 61, 6 2022. ISSN 13474065. doi: 10.35848/1347-4065/ac49fa.

[52] Nina A. Kuznetsova, Georgy V. Malkov, and Boris G. Gribov. Photoacid generators. application and current state of development. *Russian Chemical Reviews*, 89:173–190, 2 2020. ISSN 0036-021X. doi: 10.1070/rcr4899.

[53] Kimberly L. Berkowski, Kyle N. Plunkett, Qing Yu, and Jeffrey S. Moore. Introduction to photolithography: Preparation of microscale polymer silhouettes. *Journal of Chemical Education*, 82(9):1365, 2005. doi: 10.1021/ed082p1365. URL `https://doi.org/10.1021/ed082p1365`.

[54] Kumar Shubham and Ankaj Gupta. *Integrated Circuit Fabrication*. 02 2021. ISBN 9781003178583. doi: 10.1201/9781003178583.

[55] L. Jay Guo. Nanoimprint lithography: Methods and material requirements. *Advanced Materials*, 19:495–513, 2 2007. ISSN 09359648. doi: 10.1002/adma.200600882.

[56] Stephen Y Chou and Peter R Krauss. Engineering imprint lithography with sub-10 nm feature size and high throughput. *Microeleetronic Engineering*, 35:237–240, 1997.

[57] Nan Wang, Yi Li, Feng Sha, and Yu He. Sub-nanometer misalignment sensing for lithography with structured illumination. *Opt. Lett.*, 47(17):4427–4430, Sep 2022. doi: 10.1364/OL.468177. URL `https://opg.optica.org/ol/abstract.cfm?URI=ol-47-17-4427`.

[58] Karl Suess. Ma6 mask aligner technical description. URL `https://coltronics.com.au/DATA/MA6.pdf`.

[59] Yuchen Shao, Yuan'an Zhao, Hao Ma, Meiling Chen, Yafei Lian, and Jianda Shao. An easy method to improve efficiency of multi-photon polymerization: Introducing solvents with nonlinear optical absorption into photoresist. *Optics and Laser Technology*, 151, 7 2022. ISSN 00303992. doi: 10.1016/j.optlastec.2022.108008.

[60] Anthony S. Kewitsch and Amnon Yariv. Nonlinear optical properties of photoresists for projection lithography. *Applied Physics Letters*, page 455, 1995. ISSN 00036951. doi: 10.1063/1.116411.

[61] Jason Geng. Structured-light 3D surface imaging: a tutorial. *Advances in Optics and Photonics*, 3:128, 2011. ISSN 1943-8206. doi: 10.1364/aop.3.000128.

[62] Sujan Rajbhandari, Jonathan J.D. McKendry, Johannes Herrnsdorf, Hyunchae Chun, Grahame Faulkner, Harald Haas, Ian M. Watson, Dominic O'Brien, and Martin D. Dawson. A review of gallium nitride LEDs for multi-gigabit-per-second visible light data communications. *Semiconductor Science and Technology*, 32, 2017. ISSN 13616641. doi: 10.1088/1361-6641/32/2/023001.

[63] Eric H. Virey and Nicolas Baron. 45-1: Status and prospects of microled displays. *SID Symposium Digest of Technical Papers*, 49(1):593–596, 2018. doi: https://doi.org/10.1002/sdtp.12415. URL `https://sid.onlinelibrary.wiley.com/doi/abs/10.1002/sdtp.12415`.

[64] Jigang Huang, Qin Qin, and Jie Wang. A review of stereolithography: Processes and systems. *Processes*, 8:1138, 09 2020. doi: 10.3390/pr8091138.

[65] G. E. Johnstone, J. Gray, S. Bennett, S. D. Johnson, C. F. Higham, F. Dehkhoda, E. Xie, J. Herrnsdorf, P. Murray, M. J. Padgett, R. Murray-Smith, R. K. Henderson, M. D. Dawson, and M. J. Strain. High speed single pixel imaging using a micro-LED-on-CMOS light projector.

Optics Express, 32:24615, 7 2024. ISSN 1094-4087. doi: 10.1364/OE.525753. URL https://opg.optica.org/abstract.cfm?URI=oe-32-14-24615.

[66] Foad Arvani and Tony Chan Carusone. TDC sharing in SPAD-based direct time-of-flight 3D imaging applications. *Proceedings - IEEE International Symposium on Circuits and Systems*, 2019-May:0–4, 2019. ISSN 02714310. doi: 10.1109/ISCAS.2019.8702586.

[67] Pengfei Tian, Daopeng Qu, Daqi Shen, Di Sun, Zhou Wang, Zhuoqun Zhao, Zhilai Fang, and Xugao Cui. Correlation reconstruction based high-accuracy LED and micro-LED positioning. *Journal of Lightwave Technology*, pages 1–7, 2023. ISSN 0733-8724. doi: 10.1109/JLT.2023.3272002. URL https://ieeexplore.ieee.org/document/10113717/.

[68] Matthew P. Edgar, Graham M. Gibson, and Miles J. Padgett. Principles and prospects for single-pixel imaging. *Nature Photonics*, 13:13–20, 1 2019. ISSN 17494893. doi: 10.1038/s41566-018-0300-7.

[69] Yuan Zhuang, Luchi Hua, Longning Qi, Jun Yang, Pan Cao, Yue Cao, Yongpeng Wu, John Thompson, and Harald Haas. A survey of positioning systems using visible LED lights. *IEEE Communications Surveys and Tutorials*, 20:1963–1988, 7 2018. ISSN 1553877X. doi: 10.1109/COMST.2018.2806558.

[70] Jaecham Lim. Ubiquitous 3D positioning systems by led-based visible light communications. *IEEE Wireless Comms*, 22:80–85, 4 2015. doi: 10.1109/MWC.2015.7096289.

[71] Johannes Herrnsdorf, Michael John Strain, Erdan Gu, Robert K. Henderson, and Martin D. Dawson. Positioning and space-division multiple access enabled by structured illumination with light-emitting diodes. *Journal of Lightwave Technology*, 35:2339–2345, 2017. ISSN 07338724. doi: 10.1109/JLT.2017.2672864. This paper is useful for the experimental setup of the LEDs and what happens on the transmitter side of things.

[72] Carlos Zamarreño-Ramos, Teresa Serrano-Gotarredona, and Bernabé Linares-Barranco. An instant-startup jitter-tolerant manchester-encoding serializer/ deserializer scheme for event-driven bit-serial lvds interchip aer links. *IEEE Transactions on Circuits and Systems I: Regular Papers*, 58:2647–2660, 2011. ISSN 15498328. doi: 10.1109/TCSI.2011.2151070.

[73] Lalitha V. A review of Manchester, Miller, and FM0 encoding techniques. *The Smart Computing Review*, 4, 12 2014. doi: 10.6029/smartcr.2014.06.006.

[74] Neal Radwell, Kevin J. Mitchell, Graham M. Gibson, Matthew P. Edgar, Richard Bowman, and Miles J. Padgett. Single-pixel infrared and visible microscope. *Optica*, 1:285, 11 2014. ISSN 2334-2536. doi: 10.1364/optica.1.000285. URL https://www.osapublishing.org/optica/abstract.cfm?uri=optica-1-5-285.

[75] Hong-Yeop Song. Examples and constructions of hadamard matrices. 2002.

[76] Johannes Herrnsdorf, Martin D Dawson, and Michael J Strain. Positioning and data broadcasting using illumination pattern sequences displayed by LED arrays. *IEEE Transactions on Communications*, 66:5582–5592, 2018. ISSN 15580857. doi: 10.1109/TCOMM.2018.2850892. URL `http://ieeexplore.ieee.org`.

[77] Jong Kang Park, Tae Gyoo Woo, Myoungha Kim, and Jong Tae Kim. Hadamard matrix design for a low-cost indoor positioning system in visible light communication. *IEEE Photonics Journal*, 9, 4 2017. ISSN 19430655. doi: 10.1109/JPHOT.2017.2667038.

[78] Gonzalo R. Arce, David J. Brady, Lawrence Carin, Henry Arguello, and David S. Kittle. Compressive coded aperture spectral imaging: An introduction. *IEEE Signal Processing Magazine*, 31:105–115, 2014. ISSN 10535888. doi: 10.1109/MSP.2013.2278763.

[79] Zibang Zhang, Xueying Wang, Guoan Zheng, and Jingang Zhong. Hadamard single-pixel imaging versus Fourier single-pixel imaging. *Optics Express*, 25:19619, 8 2017. ISSN 10944087. doi: 10.1364/oe.25.019619.

[80] Simon Foucart and Holger Rauhut. *A Mathematical Introduction to Compressive Sensing*. 8 2013. ISBN 978-0-8176-4948-7. URL `http://www.springer.com/series/4968`.

[81] Gianmaria Calisesi, Alberto Ghezzi, Daniele Ancora, Cosimo D'Andrea, Gianluca Valentini, Andrea Farina, and Andrea Bassi. Compressed sensing in fluorescence microscopy. *Progress in Biophysics and Molecular Biology*, 168:66–80, 1 2022. ISSN 00796107. doi: 10.1016/j.pbiomolbio.2021.06.004.

[82] Jun Feng, Shuming Jiao, Yang Gao, Ting Lei, and Luping Du. Design of optimal illumination patterns in single-pixel imaging using image dictionaries. *IEEE Photonics Journal*, 12(4):1–9, 2020. doi: 10.1109/JPHOT.2020.3002477.

[83] Marco F. Duarte, Mark A. Davenport, Dharmpal Takhar, Jason N. Laska, Ting Sun, Kevin F. Kelly, and Richard G. Baraniuk. Single-pixel imaging via compressive sampling. *IEEE Signal Processing Magazine*, 25(2):83–91, 2008. doi: 10.1109/MSP.2007.914730.

[84] Zi-Hao Xu, Wen Chen, José Penuelas, Miles Padgett, and Ming-Jie Sun. 1000 fps computational ghost imaging using LED-based structured illumination. *Optics Express*, 26:2427, 2 2018. ISSN 1094-4087. doi: 10.1364/oe.26.002427.

[85] Mathieu Ribes, Gaspard Russias, Denis Tregoat, and Antoine Fournier. Towards low-cost hyperspectral single-pixel imaging for plant phenotyping. *Sensors (Switzerland)*, 20, 2 2020. ISSN 14248220. doi: 10.3390/s20041132.

[86] Claire Guilloteau, Thomas Oberlin, Olivier Berné, and Nicolas Dobigeon. Hyperspectral and multispectral image fusion under spectrally varying spatial blurs – application to high dimensional infrared astronomical imaging. *IEEE Transactions on Computational Imaging*, 6:1362–1374, 2020. doi: 10.1109/TCI.2020.3022825.

[87] E. Keith Hege, Dan O'Connell, William Johnson, Shridhar Basty, and Eustace L. Dereniak. Hyperspectral imaging for astronomy and space surviellance. *Imaging Spectrometry IX*, 5159: 380, 1 2004. ISSN 0277786X. doi: 10.1117/12.506426.

[88] J. Pablo Arroyo-Mora, Margaret Kalacska, Deep Inamdar, Raymond Soffer, Oliver Lucanus, Janine Gorman, Tomas Naprstek, Erica Skye Schaaf, Gabriela Ifimov, Kathryn Elmer, and George Leblanc. Implementation of a UAV–hyperspectral pushbroom imager for ecological monitoring. *Drones*, 3:1–24, 3 2019. ISSN 2504446X. doi: 10.3390/drones3010012.

[89] Mary B. Stuart, Andrew J.S. McGonigle, and Jon R. Willmott. Hyperspectral imaging in environmental monitoring: A review of recent developments and technological advances in compact field deployable systems. *Sensors (Switzerland)*, 19, 7 2019. ISSN 14248220. doi: 10.3390/s19143071.

[90] Dhanesh G. Kasi, Mees N.S. de Graaf, Paul A. Motreuil-Ragot, Jean Phillipe M.S. Frimat, Michel D. Ferrari, Pasqualina M. Sarro, Massimo Mastrangeli, Arn M.J.M. van den Maagdenberg, Christine L. Mummery, and Valeria V. Orlova. Rapid prototyping of organ-on-a-chip devices using maskless photolithography. *Micromachines*, 13, 1 2022. ISSN 2072666X. doi: 10.3390/mi13010049.

[91] R. Barbucha, M. Kocik, J. Mizeraczyk, G. Kozioł, and J. Borecki. Laser direct imaging of tracks on pcb covered with laser photoresist. *Bulletin of the Polish Academy of Sciences: Technical Sciences*, 56:17–20, 2008. ISSN 02397528.

[92] Meng-Chyi Wu and I-Ting Chen. High-resolution 960 × 540 and 1920 × 1080 UV micro light-emitting diode displays with the application of maskless photolithography. *Advanced Photonics Research*, 2:2100064, 2021. ISSN 2699-9293. doi: 10.1002/adpr.202100064.

[93] Dhivakar K M and Anshu Sarje. A versatile, low-cost UV exposure system for photolithography. *2021 Smart Technologies, Communication and Robotics (STCR)*, pages 1–5, 2021. doi: 10.1109/stcr51658.2021.9588848.

[94] Johannes Herrnsdorf, Jonathan J.D. McKendry, Enyuan Xie, Michael J Strain, Ian M Watson, Erdan Gu, and Martin D Dawson. High speed spatial encoding enabled by CMOS-controlled micro-LED arrays. *2016 IEEE Photonics Society Summer Topical Meeting Series, SUM 2016*, pages 173–174, 2016. doi: 10.1109/PHOSST.2016.7548774. URL `http://up-vlc.photonics.ac.uk/`.

[95] Jonathan J.D. McKendry, David Massoubre, Shuailong Zhang, Bruce R. Rae, Richard P. Green, Erdan Gu, Robert K. Henderson, A. E. Kelly, and Martin D. Dawson. Visible-light communications using a CMOS-controlled micro-light emitting diode array. *Journal of Lightwave Technology*, 30:61–67, 2012. ISSN 07338724. doi: 10.1109/JLT.2011.2175090.

[96] Gary Williams, Edward Chalupa, and Steven Rahhal. Automated positioning and alignment systems. *Source: SAE Transactions*, 109:737–745, 2000.

[97] Eleni Margariti, Benoit Guilhabert, Dimitars Jevtics, Martin D. Dawson, and Michael J. Strain. Sub-micron-accuracy automated position and rotation registration method for transferred devices. *2021 IEEE Photonics Conference, IPC 2021 - Proceedings*, 2021. doi: 10.1109/IPC48725.2021.9592935.

[98] Pittaya Deekla, Rungrueang Phatthanakun, Sarawut Sujitjorn, and Nimit Chomnawang. Al microheater and Ni temperature sensor set based-on photolithography with closed-loop control. *International Journal of Electrical and Computer Engineering (IJECE)*, 5:849–858, 2015. ISSN 2088-8708.

[99] Hiroshi Ito. Chemical amplification resists for microlithography. *Advances in Polymer Science*, 172:37–245, 2005. ISSN 00653195. doi: 10.1007/b97574.

[100] Vijay Kumar Sharma and Hilmi Volkan Demir. Bright future of deep-ultraviolet photonics: Emerging UVC chip-scale light-source technology platforms, benchmarking, challenges, and outlook for UV disinfection. *ACS Photonics*, 2022. ISSN 23304022. doi: 10.1021/acsphotonics.2c00041.

[101] Daniel Maclure, Cheng Chen, Jonathan McKendry, Enyuan Xie, Jordan Hill, Johannes Herrnsdorf, Erdan Gu, Harald Haas, and Martin D. Dawson. Hundred-meter Gb/s deep ultraviolet wireless communications using AlGaN micro-LEDs. *Optics Express*, 11 2022. ISSN 1094-4087. doi: 10.1364/OE.475049.

[102] Daniel M. Maclure, Jonathan J. D. McKendry, Mohamed Sufyan Islim, Enyuan Xie, Cheng Chen, Xiaobin Sun, Xudong Liang, Xiaohui Huang, Hanaa Abumarshoud, Johannes Herrnsdorf, Erdan Gu, Harald Haas, and Martin D. Dawson. 10 gbps wavelength division multiplexing using UV-a, UV-b, and UV-c micro-LEDs. *Photonics Research*, 10:516, 2 2022. ISSN 23279125. doi: 10.1364/prj.445984.

[103] Huabin Yu, Jikai Yao, Muhammad Hunain Memon, Yuanmin Luo, Zhixiang Gao, Dongyang Luo, Rui Wang, Zixun Wang, Wei Chen, Linjun Wang, Shuiqing Li, Jinjian Zheng, Jiangyong Zhang, Sheng Liu, and Haiding Sun. Vertically integrated self-monitoring AlGaN-Based deep ultraviolet micro-LED array with photodetector via a transparent sapphire substrate toward

stable and compact maskless photolithography application. *Laser & Photonics Reviews*, 19(2): 2401220, 2025. doi: https://doi.org/10.1002/lpor.202401220. URL `https://onlinelibrary.wiley.com/doi/abs/10.1002/lpor.202401220`.

[104] Sisi Zhou and Liang Jiang. Modern description of Rayleigh's criterion. 2019. doi: 10.1103/PhysRevA.99.013808.

[105] Jordan Hill, Cheng Chen, Enyuan Xie, Jonathan J.D. McKendry, Johannes Herrnsdorf, Erdan Gu, Harald Haas, and Martin D. Dawson. Effects of LED device size on UV-C short-range LoS optical wireless communication. *IEEE Photonics Journal*, 15(6):1–8, 2023. doi: 10.1109/JPHOT.2023.3329980.

[106] Jonathan J D McKendry, Enyuan Xie, Jordan Hill, Hichem Zimi, Johannes Herrnsdorf, Erdan Gu, Robert K Henderson, and Martin D Dawson. Deep ultraviolet cmos-controlled micro light-emitting diode array. *IEEE Photonics Journal*, 11 2023. ISSN 1943-0655. doi: https://doi.org/10.1109/JPHOT.2023.3330571. URL `https://doi.org/10.15129/2238875e-fdb1-4c83-83e8-5b4943c618cb.`

[107] Stefan Wolter, Hendrik Spende, Jan Gülink, Jana Hartmann, Hergo Heinrich Wehmann, Andreas Waag, Andreas Lex, Adrian Avramescu, Hans Jürgen Lugauer, Norwin von Malm, Jean Jacques Drolet, and Martin Strassburg. Size-dependent electroluminescence and current-voltage measurements of blue InGaN/GaN μLEDs down to the submicron scale. *Nanomaterials*, 11, 2021. ISSN 20794991. doi: 10.3390/nano11040836.

[108] Daniel M. Maclure, Jonathan J. D. McKendry, Johannes Herrnsdorf, Xiangyu He, Enyuan Xie, Erdan Gu, and Martin D. Dawson. Size-Dependent Characterization of Deep UV Micro-Light-Emitting Diodes. In *2020 IEEE Photonics Conference (IPC)*, pages 1–2, 2020. doi: 10.1109/IPC47351.2020.9252420.

[109] NOA81 optical adhesive website, First accessed 8/8/2022. URL `https://www.norlandprod.com/adhesives/NOA$%$2081.html`.

[110] A. H. Firester, M. E. Heller, and P. Sheng. Knife-edge scanning measurements of subwavelength focused light beams. *Appl. Opt.*, 16(7):1971–1974, Jul 1977. doi: 10.1364/AO.16.001971. URL `https://opg.optica.org/ao/abstract.cfm?URI=ao-16-7-1971`.

[111] Anthony E. Siegman. Choice of clip levels for beam width measurements using knife-edge techniques. *IEEE Journal of Quantum Electronics*, 27:1098–1104, 1991. ISSN 15581713. doi: 10.1109/3.83346.

[112] Aimee Rose, Zhengguo Zhu, Conor F. Madigan, Timothy M. Swager, and Vladimir Bulovic. Sensitivity gains in chemosensing by lasing action in organic polymers. *Nature*, 434:873–876, 4 2005. ISSN 00280836. doi: 10.1038/nature03427.

[113] Alexander Kaltashov, Prabu Karthick Parameshwar, Nicholas Lin, and Christopher Moraes. Accessible, large-area, uniform dose photolithography using a moving light source. *Journal of Micromechanics and Microengineering*, 32, 2 2022. ISSN 13616439. doi: 10.1088/1361-6439/ac4005.

[114] Alex Blanchard, Paul R Edwards, Benoit Guilhabert, Erdan Gu, Ian M Watson, and Johannes Herrnsdorf. Hyperspectral alignment capability for direct writing systems enabled by structured illumination with a micro-LED array. *Journal of Optics*, 2025. doi: 10.1088/2040-8986/adcfb0. URL `http://iopscience.iop.org/article/10.1088/2040-8986/adcfb0`.

[115] Paul R. Edwards, Robert W. Martin, and Martin R. Lee. Combined cathodoluminescence hyperspectral imaging and wavelength dispersive x-ray analysis of minerals. volume 92, pages 235–242. Mineralogical Society of America, 2007. doi: 10.2138/am.2007.2152.

[116] François Templier, Lamine Benaïssa, Bernard Aventurier, Christine Di Nardo, Matthew Charles, Anis Daami, Franck Henry, and Ludovic Dupré. 19-6: Invited Paper: A Novel Process for Fabricating High-Resolution and Very Small Pixel-pitch GaN LED Microdisplays. *SID Symposium Digest of Technical Papers*, 48(1):268–271, 2017. doi: https://doi.org/10.1002/sdtp.11684. URL `https://sid.onlinelibrary.wiley.com/doi/abs/10.1002/sdtp.11684`.

[117] Ludovic Dupré, Marjorie Marra, Valentin Verney, Bernard Aventurier, Franck Henry, François Olivier, Sauveur Tirano, Anis Daami, and François Templier. Processing and characterization of high resolution GaN/InGaN LED arrays at 10 micron pitch for micro display applications. In *OPTO*, 2017. URL `https://api.semanticscholar.org/CorpusID:125252729`.

[118] Alex Olwal and Bernard Kress. 1d eyewear: Peripheral, hidden LEDs and near-eye holographic displays for unobtrusive augmentation. pages 184–187. Association for Computing Machinery, 10 2018. ISBN 9781450359672. doi: 10.1145/3267242.3267288.

[119] Masaki Kawasaki, Yasuo Watanabe, Takumi Yamaguchi, and Yasutada Sakamoto. Volumetric 3d display with scanned 1d led arrays and its application to animation contents, 2006. URL `https://doi.org/10.1145/1179622.1179634`.

[120] Y.D. Gokdel, B.Sarioglu, and A.D. Yalcinkaya. *2D IMAGING WITH 1D LED ARRAY INTEGRATED FR4 ACTUATOR*. IEEE, 2011. ISBN 9781457701566.

[121] Klaus Suhling, Liisa M. Hirvonen, James A. Levitt, Pei Hua Chung, Carolyn Tregidgo, Alix Le Marois, Dmitri A. Rusakov, Kaiyu Zheng, Simon Ameer-Beg, Simon Poland, Simao Coelho,

Robert Henderson, and Nikola Krstajic. Fluorescence lifetime imaging (FLIM): Basic concepts and some recent developments. *Medical Photonics*, 27:3–40, 5 2015. ISSN 22138846. doi: 10.1016/j.medpho.2014.12.001.

[122] Alexander D. Griffiths, Haochang Chen, Johannes Herrnsdorf, David Li, Robert K. Henderson, Michael J. Strain, and Martin D. Dawson. Hyperspectral imaging under low illumination with a single photon camera. Institute of Electrical and Electronics Engineers Inc., 3 2019. ISBN 9781538673614. doi: 10.1109/BICOP.2018.8658323. URL `http://dx.doi.org/10.15129/3de27021-520e-4e1b-9501-c5d95360af2b`.